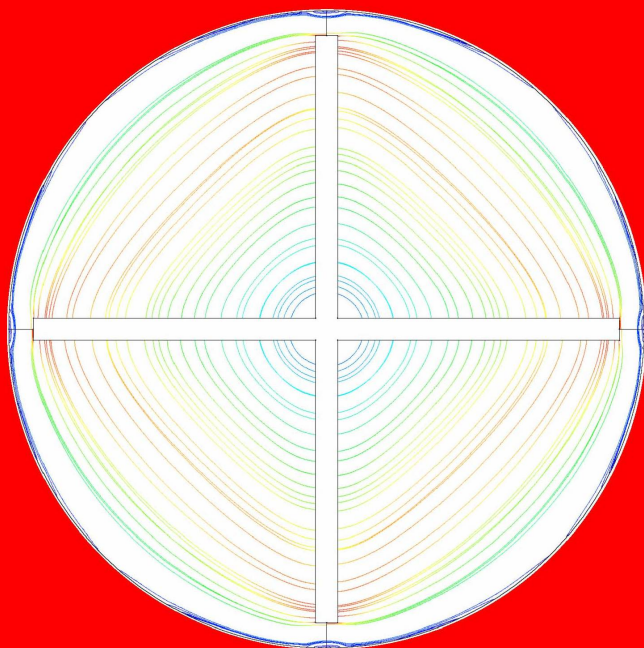


Alejandro Peugnet

Experimental and numerical investigations for vane flow



Cuvillier Verlag Göttingen
Internationaler wissenschaftlicher Fachverlag

Experimental and numerical investigations for vane flow

**Der technischen Fakultät der
Universität Erlangen–Nürnberg
zur Erlangung des Grades**

DOKTOR–INGENIEUR

vorgelegt von

Alejandro Peugnet

Erlangen, 2009

Bibliografische Information der Deutschen Nationalbibliothek

Die Deutsche Nationalbibliothek verzeichnet diese Publikation in der Deutschen Nationalbibliografie; detaillierte bibliografische Daten sind im Internet über <http://dnb.ddb.de> abrufbar.

1. Aufl. - Göttingen : Cuvillier, 2009

Zugl.: Erlangen-Nürnberg, Univ., Diss., 2009

978-3-86955-048-0

Als Dissertation genehmigt von
der technischen Fakultät der
Universität Erlangen–Nürnberg

Tag der Einreichung:	21.12.2005
Tag der Promotion:	25.07.2008
Dekan:	Prof. Dr.–Ing. habil. J. Huber
Berichterstatter:	Prof. Dr.–Ing. P. O. Brunn
	Prof. Dr.–Ing. B. Gampert

© CUVILLIER VERLAG, Göttingen 2009

Nonnenstieg 8, 37075 Göttingen

Telefon: 0551-54724-0

Telefax: 0551-54724-21

www.cuvillier.de

Alle Rechte vorbehalten. Ohne ausdrückliche Genehmigung des Verlages ist es nicht gestattet, das Buch oder Teile daraus auf fotomechanischem Weg (Fotokopie, Mikrokopie) zu vervielfältigen.

1. Auflage, 2009

Gedruckt auf säurefreiem Papier

978-3-86955-048-0

To my parents,
Dinorah y Alejandro

Acknowledgement

What we become in life is the sum of many elements. A chain of facts that has been built along the way until we reach a certain point. At this point I will like to thank people that have supported me through my life in one or the other way and made possible my education and thus this thesis.

Not long time ago my first choice to pursue university studies was pharmacy. To be sure if this was the 'right' path to follow I worked during a summer at the Carvali's laboratories under the guidance of Dr. Raúl Estrada. During that summer I realized that I could go further if I combine or enhance those pharmacy studies with some industrial aspects, typical of chemical engineering. After that summer I decided to study chemical engineering.

At that time there was only one university offering chemical engineering and since the demand was high one had to pass an examination in mathematics. At school I had an excellent mathematics teacher named Oscar Rodríguez who regularly gave me math tasks making it possible for me to take part during those school-years at the 'olimpiadas de matemáticas'. This training allowed me to pass all requirements to enter the university.

After the studies in Managua I went to take some courses in chemical engineering at the Friedrich–Alexander University in Erlangen, Germany. It was Prof. Dr. Dr. h.c. Franz Durst who was head of the institute of fluid mechanics at that time, who accepted my application. To finance my studies I worked in the rheology research-group in the institute of fluid mechanics. I started to work as an assistant with Dr. Ing. Thomas Wunderlich in electro and magnetho–rheology. Later on, when he left the institute I started to work with Dr. Ing. Regina Krüßmann in experimental work of fluid flow through porous media.

My friend Dr.–Ing. Özgür Ertunç arrived nearly at the same time with me to the institute. He was always helpful and collaborative in all aspects. For many situations in which he was involved I highly appreciate his help and support whenever I needed. We had very good times while working at LSTM.

I am specially grateful to my thesis supervisor (Doktorvater) Prof. Dr.–Ing. Peter Otto Brunn for all the discussions we had on the subject, his guidance and friendly support. His vast experience contributed enormously to my work.

In the rheology research–group there was always an agreeable atmosphere making our work more pleasant. I thank to my colleagues Dr.–Ing. Florian Zschunke, Dr.–

Ing. Regina Krüßmann for proof-reading the manuscript and making comments. I thank Dr.-Ing. Hesham Hasoud from whom I took some of the equipment used for the PIV measurements. I also thank to the students who did their master thesis or did some internship under my guidance: MSc. Li Yang who did an internship and later on his master thesis on numerical simulations, MSc. Ayse Betul who did her thesis on experimental flow visualization. Thanks to Battamsetty Ajay Chandra from the University Darmstadt who did his MSc. internship in our group and also worked in rheological characterization of aqueous polymer-solutions. Thanks to MSc. Rosa Rivas for being collaborative and friendly during the time we worked in the rheology research-group.

Many thanks to the LSTM mechanical and electronic workshop who rapidly solved any technical problem: to Jürgen Heubeck for helping to build the experimental facility, to Horst Weber who always was willing to help regarding laser techniques and made a simple, inexpensive and effective trigger for the PIV measurements. For the willingness to help whenever it was necessary thanks to Franz Kaschak and Robert Pavlik. I thank my colleagues Dr.-Ing. Phillip Epple and Naser Sahiti for the valuable discussions we had on numerical simulations.

Special thanks to my girlfriend Dr. Stefania Odoni for her continuous support and patience. For designing the cover of the thesis and making the German translations.

Many thanks to the members of the thesis committee: Prof. Dr.-Ing. A. Delgado, Prof. Dr.-Ing. A. Roosen, Prof. Dr.-Ing. habil. K-E. Wirth, Prof. Dr.-Ing. B. Gampert and Prof. Dr.-Ing. P. O. Brunn. I thank to Prof. De Souza Mendes who kindly provided me one paper of the results of his investigations on rotating bob and vane geometries. For many discussions we had, thanks to my colleagues from LSTM, Dr.-Ing. Çatagay Köksoy, Dr.-Ing. Joao Pêgo and Dr.-Ing. Balkan Genç.

Thanks to Sandrine Benyaich for her support during the years in which this research work was being carried out.

Last but not least I thank to Ina Paulus who always took care that everything worked out at the institute and was always with a happy smile upon her face.

Thanks to Ilse Grimm, Dr. B. Mohr, Iris Knopf and Johanna Grasser for her support regarding the usual contract formalities at the University.

Erlangen, 23rd of July 2009
Alejandro Peugnet

Notation

Latin symbols

Symbol	Description	Units
A_b	Surface area of face b of the control volume	
ALE	Arbitrary–Lagrangian–Eulerian	
b	Face of the control volume (i.e. w, n, e, s)	
B	Nodal point (cell), i.e. W, N, E, S	
BC	Boundary condition	
b_t	Thickness of the blade	mm
c	Dimensionless constant	
C	Carbon	
CC	Concentric–cylinder	
CCD	Coupled charge device	
CC 27	Concentric–cylinder measuring system	
[c]	Concentration	w/w%
c_1	Device constant (for shear stress)	Pa/mN– m
c_2	Device constant (for shear rate)	s/s
CD	Central difference	
CFX	Commercial software used for the simulations	
ChC	Characteristic curve	
C_L	Correction factor	
CMR	Creeping motion regime	
CP	Cone–plate	
CPyCl	Cetylpyridinium	mM
C_v	Device constant (for viscosity)	
c_γ	Device constant for the vane	s/s
c_τ	Device constant for the vane	Pa/N – m
D	Displacement (PIV measurement)	px
D	Rate of deformation tensor	1/s
dA	Surface element of control volume	
DCS	Deferred correction scheme	
D_{ij}	ij component of rate of deformation tensor	1/s
dx	Length of a CV face in x–Cartesian coordinate	mm
D_{xx}	xx component of rate of deformation tensor	1/s
D_{xy}	xy component of rate of deformation tensor	1/s
d_p	Diameter of a tracer particle	μm

Symbol	Description	Units
d_v	Diameter of the vane	mm
dV	Volume element of control volume	
dy	Length of a CV face in y–Cartesian coordinate	mm
e	Unit vector	
$e_r, e_\varphi,$	Unit vector in r and φ direction, respectively	
e_φ	Unit vector, φ –direction	
e_r	Unit vector, r–direction	
F_b^C	Convective flux through face b of the control volume	
FD	Finite difference	
F_b^D	Diffusive flux through face b of the control volume	
FDK	Flügeldrehkörper (Eng. vane)	
FE	Finite element	
f_x	Interpolation factor	
FVM	Finite volume method	
GNF	Generalized Newtonian fluid	
H	Hydrogen	
H^+	Ion of hydrogen	
hpg	Hydroxypropyl guar	
I_2	Second principal invariant	
i	Unit vector i–direction	
j	Unit vector j–direction	
k	Unit vector k–direction	
ICEM CFD	Commercial software used to generate the mesh	
K	Device constant	m^3
KZV	Konzentrisch Zylinder Viskometer (Eng. concentric cylinder)	
LDV	Laser Doppler velocimetry	
l_v	Length of the vane	mm
l_B	Length of the cup	mm
m	Consistency (power–law fluid)	$Pa\ s^n$
m_p	Mass of polymer	g
MC	Master curve	
m_s	Mass of solvent	g
M	Torque	mN m
M_S	Torque at the side (bob or imaginary cylinder circumscribed in the vane geometry)	mN m
M_E	Torque at the end (bob or imaginary cylinder circumscribed in the vane geometry)	mN m
M_{max}	Maximum torque	mN m

Symbol	Description	Units
M_{ref}	Reference torque	mN m
MUSCL	Monotone Upwind Schemes for Scalar Conservation Laws	
M_S	Torque on the side	mN m
M_{NS}	Torque calculated under non-slip conditions	mN m
n	Power-law index	
\mathbf{n}	Unit-vector in the normal direction	
\mathbf{n}_b	Unit-vector normal to the face b	
N	Number of blades	
NF	Newtonian fluid	
NNF	Non-Newtonian fluid	
Na	Sodium	
NaSal	Sodium salicylate	mM
Ne	Newton number	
O	Oxygen	
P	Hydrodynamic pressure	Pa
P_e, P_w	Hydrodynamic pressure on east and west sides of the CV	Pa
pa	Polyacrylamide	
P^*	Dimensionless pressure	Pa
PDE	Partial differential equation	
PIV	Particle image velocimetry	
Q_Φ	Source term of the transported variable Φ	
Q_Φ^D	Diffusive source-term of the transported variable Φ	
Q_Φ^P	Pressure source-term of the transported variable Φ	
r	Radius	mm
r'	Radius (local coordinate)	mm
r^*	Dimensionless radius	
r_c	Radius of the bob	mm
Re	Reynolds number	
Re_{ref}	Reference Reynolds number	
R_{fg}	Cross correlation function	
r_i	Inner radius	mm
r'_{max}	Maximum value of the radius (local coordinate)	mm
r_o	Radius of the cup	mm
ROH	Mannose unit	
r_v	Radius of the vane	mm
Si	Silicon	
sio	Silicon oil	
SS	Schleichende Strömung (Eng. creeping flow)	

Symbol	Description	Units
t	Time	s
t^*	Dimensionless time	
t_e	Final time (PIV measurement)	s
t_i	Initial time (PIV measurement)	s
T_iO_2	Titanium dioxide	
TVD	Total variation diminishing	
u	Total velocity	
\mathbf{u}	Speed	mm/s
\mathbf{u}^*	Dimensionless velocity vector	
\mathbf{u}_b	Velocity vector through face b	mm/s
UD	Upwind difference	
UDS 200	Universal dynamic spectrometer (series model 200)	
u_f	Velocity of the fluid	mm/s
u_x	Component of the velocity in x -direction	mm/s
u_y	Component of the velocity in y -direction	mm/s
u_r	Component of the velocity in r -direction	mm/s
u_φ	Component of the velocity in φ -direction	mm/s
VF	Viscometric flow	
W, N, E, S	West, North, East and South (nodal point)	
w, n, e, s	West, North, East and South (face of control volume)	
x	Cartesian coordinate (global)	mm
x'	Cartesian coordinate (local)	mm
x_i	Position of the tracer particle in Cartesian coordinate (PIV measurement)	mm
x_{00}	Half of the blade thickness in Cartesian coordinates (origin of local coordinate system)	mm
x_b	Nodal location of face b of the CV in Cartesian coordinates	mm
x_B, x_E, x_P	Nodal location of computational points B, E and P in Cartesian coordinates, respectively	mm
xg	Xanthan gum	
y	Cartesian coordinate (global)	mm
y'	Cartesian coordinate (local)	mm
y_{00}	Half of the blade-thickness in Cartesian coordinates (origin of local coordinate system)	mm
2-D	Two-dimensional	
3-D	Three-dimensional	

Greek symbols

Symbol	Description	Units
α	Parameter for power-law region in Cross model	
β	Parameter in Carreau–Yasuda model	
ΔA	Surface area of control volume	
Δt	Elapsed time (PIV measurement)	s
ΔV	Volume of control volume	
ε	Error associated between exact and approximated velocity fluid in a PIV measurement	
η	Viscosity	Pa s
η_0	Zero-shear Viscosity	Pa s
η_{eff}	Effective viscosity	Pa s
η_∞	Infinite shear-viscosity	Pa s
η_{ref}	Reference shear-viscosity	Pa s
η^*	Dimensionless viscosity	
λ	Characteristic time	s
γ	Blend factor	
$\dot{\gamma}$	Shear rate	1/s
$\dot{\gamma}^*$	Dimensionless shear rate	
Γ_Φ	Transport coefficient of the transported variable Φ	Pa s
$\Gamma_{\Phi,b}$	Transport coefficient of the transported variable Φ through face b	Pa s
$\Gamma_{\Phi,B}; \Gamma_{\Phi,E}; \Gamma_{\Phi,f_x}; \Gamma_{\Phi,P}$	Transport coefficient of the transported variable Φ through nodal points B, E, f_x and nodal point P, respectively	Pa s
κ	Aspect ratio	
∇	Nabla operator	
Ω	Angular velocity	1/s
∂_t	Partial time-derivative	
Π	Pressure scaling-parameter	
Φ	Transported variable, i.e. velocity	mm/s
Φ_b, Φ_e	Transported variable through face b and e of the control volume	
$\Phi_B, \Phi_E, \Phi_{f_x}, \Phi_P$	Transported variable through nodal points B, E, f_x and P of the control volume, respectively	
ρ	Density	kg/m ³
τ	Shear stress	Pa
$\boldsymbol{\tau}$	Shear stress tensor	Pa
$\boldsymbol{\tau}^*$	Dimensionless shear-stress tensor	
φ	Angle (global coordinate-system)	°

Symbol	Description	Units
φ'	Angle (local coordinate–system)	°
τ_e	Shear stress at the end	Pa
τ_i	Shear stress at the inner wall	Pa
τ_{max}	Maximum shear stress	Pa
τ_o	Shear stress at the outer wall	Pa
τ_y	Yield stress	Pa
τ_v	Shear stress at the bob	Pa
τ_w	Shear stress at the wall	Pa

Contents

Contents	i
Summary	iv
1 Introduction	1
2 Literature survey	5
2.1 Effect of vane dimensions	14
2.2 End effects	15
2.3 Scope of the thesis	16
3 Numerical method	19
3.1 Finite volume method	19
3.2 General transport equation	20
3.3 Non-dimensional formulation	23
3.4 Discretization of the general transport equation with the FVM	24
3.5 Discretization of the diffusive flux	24
3.6 Discretization of the source term	27
3.7 Software used	27
3.7.1 CFX package	28
4 Vane geometry and statement of the problem	31
4.1 Vane geometry	31
4.2 Idealized assumptions	31
4.3 Torque on a rotating vane	32
4.4 Governing equations	34
4.4.1 Boundary conditions	35
4.5 Mesh for the vane geometry	38
5 Optical method	41
5.1 Particle image velocimetry	41
5.1.1 Image acquisition	42
5.1.2 Interrogation	44
5.1.3 Data validation	45
5.1.4 Data analysis	45
5.1.5 Displacement of the tracer particles	46
6 Materials and equipment	49
6.1 Materials	49
6.1.1 Newtonian fluids	49

CONTENTS

6.1.2	Non-Newtonian fluids	50
6.2	Equipment	52
6.2.1	The rheometer Physica UDS 200	52
6.2.2	Concentric-cylinder measuring system (CC 27)	53
6.2.3	Vane-in-cup measuring system	54
6.2.4	PIV set-up	55
7	Flow curves	59
7.1	Newtonian fluids	59
7.2	Non-Newtonian fluids	60
7.2.1	Preparation of the solutions	61
7.2.2	Hydroxypropyl guar	62
7.2.3	Xanthan gum	62
7.2.4	Polyacrylamide	62
7.3	Characterization with the solvent viscosity	64
8	The vane as viscometer	67
8.1	Non-dimensional formulation	67
8.2	Determining the shear rate in vane flow	73
9	PIV measurements	85
9.1	Flow between the blades	85
9.2	Transformation of coordinates	87
9.3	Velocity profiles	90
10	Numerical simulations for vane flow	95
10.1	Flow field	96
10.2	Profiles of the velocity within the blades	100
10.3	Profiles of the velocities near the vane	104
10.4	Profiles of the velocity along the gap	107
10.5	Vane flow and ideal solid-body rotation	110
10.6	Shear rate along the gap and the edge of the vane	111
10.7	Torque	115
	Bibliography	117
	Table of contents in german	136
A	Cup for PIV measurements	137
A.1	Bob and vane geometries used for the experiments	138
B	Flow curves	139

C	Measurement of the yield stress	142
D	Velocity profiles for the NF and GNF	144
E	Streamlines for a NF and a power-law fluid (Ostwald de Waele)	150
	List of Figures	151
	List of Tables	153
	Index	155

Summary

The aim was to find out if, and if yes subject to what restrictions, the vane could be used as a viscometer, even for viscoelastic fluids. The rationale of such an attempt is based on the fact that in all viscometers, which require fluid inertia to be neglected, a viscometric flow does not exist, no matter how small Re is. Prominent examples are cone–plate flow and torsional (i.e. plate–plate) flow. Secondary motions always affect the ideal local flow kinematics. Yet, only at sufficiently large Re -numbers do these changes in the local velocity field lead to measurable global relationships, which are used in determining η . For purely rotational devices this is the M – Ω relationship.

The fluids used were taken from the class of aqueous polymer–solutions. Three different types of polymers were used, namely an industrial one (polyacrylamide), a biopolymer (hydroxypropyl guar) produced industrially by adding polypropylene to guar gum and the biopolymer xanthan gum with its helical backbone. For either type of polymer solution three or four different concentrations were used.

Using a Couette viscometer (concentric cylinder, CC) the flow curves were obtained. It turned out that, depending upon concentration, the flow curves differed quantitatively but showed qualitatively similar behavior. While a Cross–like model sufficed for the two biopolymers, a Carreau–Yasuda–like model was required for the polyacrylamide solutions. Irrespective of these details a master curve allows the flow curve to be determined for any concentration without actually measuring $\eta(\dot{\gamma})$.

To use the vane as a viscometer requires its characteristic curve (ChC) $Ne = Ne(Re)$ to be established. To this end various Newtonian fluids (NFs) were used, in our case various silicon oils of low molecular weight. The influence of η on the ChC is largest in the creeping motion regime (CMR), when $Ne = c/Re$ is bound to hold. In our case up to $Re \approx 10$ one is in the CMR, where $c = 13.51$ was established experimentally. Since this constant differs rather drastically from the one used in our commercial CC–viscometer (of similar dimensions as the vane device) it is clear that substantially different flow fields have to prevail in these two devices.

For non–Newtonian fluids (purely viscous or viscoelastic ones) η is not a constant but rather depends upon $\dot{\gamma}$. Thus, η_{ref} was utilized (in our case the solvent water was used as the reference fluid) to define a reference Reynolds number Re_{ref} .

If $Ne Re = c$ characterizes the CMR then a change of $Ne Re_{ref}$ vs Re_{ref} to $Ne Re$ vs Re requires, in a log–log plot a shift along a 45° line. The magnitude of this shift furnishes η . For each Ω the function $\eta = \eta(\Omega)$ can thus be determined. Equating then $\eta(\Omega)$ with the viscometrically established flow curve $\eta = \eta(\dot{\gamma})$ furnishes a relation between Ω and $\dot{\gamma}$. For Ω small enough (small Re) the relation is linear, i.e. $\dot{\gamma} = c_\gamma \Omega$ prevails. Although c_γ differs slightly from fluid to fluid, the fluid–independent approximation $c_\gamma \approx 4$ (in our case) produces satisfactory results in all cases. It is this fact which allows the vane to be used as a viscometer.

Having succeeded in showing that the vane can be used as a viscometer there are limitations. For viscoelastic fluids deviations from $Ne Re = c$ show up at higher Re numbers, even when $Ne Re = c$ holds in case of Newtonian fluids. This can be most clearly seen in a direct comparison between $\eta(\dot{\gamma})$ from viscometric measurements with $\eta(\Omega)$ from vane flow. Elastic effects seem to be responsible for such behavior. Being non–linear they start to influence the global M – Ω relation at higher shear–rates, the more so the more elastic the fluid is. As soon as elasticity affects the global M – Ω relation the vane ceases to furnish flow curves. For slightly elastic fluids it is fluid inertia which limits the vane’s use as a viscometer (as it does in cone–plate and, respectively in torsional flow).

This gets strengthened from PIV results. Even for NFs these results show clearly that the streamlines between the blades are not circular. Thus, a rigid body motion between the blades and a viscometric flow outside the blades does not exist. This, however, would be the requirement for the fluid’s elasticity to have no effect on the flow field.

The numerical results were obtained in the true CMR regime, i.e. $Re = 0$. In this limit fluid inertia plays no role and the flow can be approximated by a steady one. This fact can be understood if one uses a rotating coordinate system in which the vane is at rest. In this system the flow is indeed steady. But Coriolis and centrifugal forces have to be reckoned with the fact that either one scales with Re implies that for $Re = 0$ they play no role. The name inertial forces is quite appropriate. While the local streamlines and contour lines (lines of constant speed) quite clearly deviate from the ideal ones (in agreement with the PIV measurements) the M – Ω relation shows good agreement with experimental results for small Ω , with noticeable deviations at larger Ω . This does not come unexpected, given the fact that generalized NFs cannot account for any elasticity of the fluid. All polymer solutions used were viscoelastic. Thus the conclusion is that the vane can be used as a viscometer, subject to the limitations that the fluid’s elasticity and/or fluid inertia will sooner or later limit its use for viscoelastic fluids.

1 Introduction

Since the breakthrough of Bingham in the late 20's of the 20th century when he modeled for the first time a *non-Newtonian fluid*, rheology, a branch of continuum mechanics, has been evolving in the study of the deformation of matter. This study covers not only the measuring of the deformation of matter under a certain applied stress or strain but also its use, modeling and understanding.

In order to characterize a material, data need to be collected from measurements. These data should allow to reproduce the deformation of the material and understand how this deformation occurs. This step encloses the modeling of the material property of interest, e.g. the viscosity. One correlates forces acting on the fluid (e.g. torque) with the deformation rate (shear rate) and the resulting relationship between these two variables provides information concerning the viscosity.

To describe the behavior of a material and collect data experimentally a rheometer is necessary. In this device one tries to create ideal flow conditions of the fluid. An example is provided by a rotational rheometer.

Rotational rheometers are well established devices which have been widely used in research as well as in industry.

As mentioned above, for the case of the viscosity one tries to establish a function of the form

$$\eta = f\left(\frac{M}{\Omega}\right), \quad (1.1)$$

where M stands for the torque applied and Ω for the angular velocity measured during the test.

In rotational rheometers it is sometimes necessary to carry out the tests up to relative high velocities or torques. This implies that secondary motions have to be reckoned with. In rheometers such as the (one-gap) concentric cylinder (bob-in-cup geometry) this type of flow will deliver wrong values for the viscosity of the fluid. Although this is a limiting factor this is not the only problem when measuring the viscosity of a fluid with a bob-in-cup system. The so-called wall slip may also occur at the surface of the cylinders.

One can say that slip occurs when a thin layer or film forms on the shearing surface so that the typical equations used to estimate the viscosity with the bob-in-cup system, based on the assumption of non-slip at the walls will not allow to predict the viscosity. It is possible to overcome these obstacles just by limiting the measuring range or modifying the surface of the cylinders. Of course this is not always the best and simplest way to overcome these issues. Often one encounters suspensions where special care has to be paid to avoid disrupting the sample during the immersion of the bob.

An alternative to the bob-in-cup geometry is the vane-in-cup geometry. In this geometry any slip effect at the vane can be excluded and less breakage of the structures –in the case of suspensions– will occur upon immersion of the rotating body. The sample is kept homogeneous. In the present work we investigate a 4-bladed vane immersed in a cup. Despite its simplicity in construction its use has been restricted until now almost only to measuring the yield stress .

Since the vane-flow is not viscometric there is no simple analytic solution for estimating the shear rate if one wants to calculate the deformation as done with the bob-in-cup geometry. Any application of the equations that are employed for rotational rheometers to estimate the shear rate is bound to lead to wrong values.

One way of calculating the shear rate is via numerical simulations which also serve to validate experimental data and / or rheological models. Computational fluid dynamics (CFD) has been developing continuously during the last twenty years with an increasing tendency toward non-Newtonian rheology. Nowadays powerful numerical techniques and hardware are available to investigate relatively complex flows. This allows us to overcome experimental limitations encountered in rheometry due to restrictions imposed by the equipment or measuring techniques.

In the present work experimental and numerical investigations are carried out for vane flow. In this context special attention is paid to its use for material characterization. The whole work is structured as follows.

Chapter 2 gives an overview of the work performed with the vane geometry in the last twenty years. There, a summary is given of the direction investigations have taken to measure the yield stress and attempts to measure the viscosity of fluids.

Chapter 3 is devoted to the numerical aspects to perform the simulations for vane flow. The finite volume method (FVM) and the discretization approach to solve the governing equations are presented. The non-dimensional scaling of the gen-

eral transport equation, which is the basis for our simulations, is also derived and at the end of the chapter, the software used for the simulations, the pre and post-processing is also briefly described.

Chapter 4 introduces the vane-in-cup geometry. Here are imposed the boundary conditions of the problem, the mesh of the geometry and some theoretical aspects for its general use in rheological material-characterization.

In chapter 5 the methodology of the optical measuring technique used for the visualization of the flow is described. Here we are concerned with the elementary procedure for image acquisition, statistical validation and analysis of data for the estimation of the displacement of the tracer particles present in the fluid.

Chapter 6 is concerned with Newtonian and non-Newtonian fluids considering their chemical and physical properties. The reference viscometer, namely the bob-in-cup system which was used to characterize the different fluids is shown schematically under the usual assumptions to calculate the shear stress and the viscosity of a fluid and compared to the vane-in-cup geometry. In addition, the experimental set-up including the vane viscometer is schematically represented.

Chapter 7 deals with the rheological material-characterization of the Newtonian and non-Newtonian fluids. In chapter 8 our approach in estimating the device constants for the vane-in-cup geometry for its use as viscometer is explained and demonstrated. The flow curves of non-Newtonian fluids modeled in chapter 7 are compared with those computed with our approach and the usage of the vane as viscometer is shown.

Finally in chapters 9 and 10 the results of the experimental visualization and numerical simulations for the vane flow at certain regions of the flow domain are presented and discussed.

2 Literature survey

In the last twenty years many authors attempted to develop methods to use the vane for material characterization in a rheological context. These methods were developed or implemented to measure the yield stress or the viscosity of fluids. A consequence of these methods is a self-imposed dependence upon the rheological model used to calculate the device constants. All these works can be divided into three main categories: experimental, theoretical and numerical.

Experimental investigations have been devoted to characterize materials and to determine the device constants. The efforts of theoretical and numerical studies try to describe the flow behavior in the vane-in-cup system considering material properties and / or the geometry. Theoretical studies show that the mathematical treatment of the vane is complex. Whatever the investigations were dealing with there were always common assumptions about the type of flow.

The following section gives an overview of the most important research work carried out for the vane flow in the last twenty years. Table 2.1 summarizes these works.

Table 2.1: Overview of the research-work carried out with the vane geometry since 1983.

Author	Year	Material	Approach
Nguyen et al. [58]	1983	Bingham, Casson, Herschel-Bulkley, Buckingham-Reiner	Experimental (Yield stress)
Keentok et al. [48]	1985	Bingham	Numerical (Shear surface)
Nguyen et al. [59]	1985	Bingham, Casson, Herschel-Bulkley	Experimental (Yield stress)

Continued on next page

Author	Year	Material	Approach
Yoshimura et al. [83]	1987	Suspensions	Experimental (Yield stress)
Haimoni et al. [39]	1988	Cement slurry	Experimental (Yield stress)
Barnes et al. [11]	1990	Newtonian, Ostwald de Waele	Numerical
Alderman et al. [2]	1991	Clay suspensions	Experimental (Yield stress)
Sherwood et al. [72]	1991	Colloidal suspensions, Newtonian	Theoretical
Castell-Perez et al. [23]	1990	Newtonian, Ostwald de Waele	Experimental (Device constants)
Atkinson et al. [5]	1992	Newtonian, linear elastic	Theoretical (Stress, Flow)
Briggs et al. [18]	1996	Frozen ice	Experimental (Yield stress)
Liddell et al. [62]	1996	Suspensions	Experimental (Yield stress)
Yan et al. [80]	1997	Herschel-Bulkley, Casson, Maxwell	Numerical (Yield surface)
Daubert et al. [28]	1998	Food products	Numerical (Yield stress)
Perez et al. [63]	1999	Red mud, soft clay	Numerical (Stresses)
Glenn III et al. [36]	2000	Newtonian,	Experimental

Continued on next page

Author	Year	Material	Approach
		Ostwald de Waele	(Device constants)
Bravian et al. [15]	2002	Newtonian, Power-law	Experimental (Yield stress, Device constants)
Rolon-Garrido et al. [69]	2002	Micellar solutions	Experimental (Flow stability)
Farias et al. [33]	2004	Polymer solutions	Experimental (Material characterization)
Krulis et al. [49]	2004	Flavored yoghurt, Newtonian	Experimental (Device constants)
Martinez-Padilla et al. [53]	2004	Sauces	Experimental (Material characterization)

Nguyen et al. ([58], [59]) introduced at the beginning of the eighties a relatively new method for measuring the yield stress with the vane-in-cup geometry. This method consisted in treating the rotating vane as an imaginary cylinder¹. This facilitated the calculation of the torque exerted on the vane since the equations used to calculate stress distributions in a cylinder were directly applied. In this experimental work they performed a series of measurements with high liquid-solid suspensions whose flow behavior could be predicted with different constitutive equations namely the Bingham, Herschel-Bulkley, Buckingham-Reiner and Casson models. They also considered a 'correction' since the vane diameter in practice does not approach zero, that is, they took into account a non-uniform stress-distribution effect over the ends of the cylinder.

Following the assumptions introduced by Nguyen et al., Keentok ([48]) carried out

¹This has been an usual assumption in soil mechanics ([59]).

numerical simulations with a finite–element (FE) code on a four–bladed vane as well as some experimental work. He concentrated his work on the fracture zone (or surface of shearing) around the four–bladed rotating vane in a Bingham fluid. According to his numerical simulations the region where shearing occurs has a diameter slightly larger than the vane diameter and was about 2.5% larger than the vane diameter. No information is given about the mesh employed. From the results of his experiments he claims that the diameter of the shearing surface was 1.00–1.05 times larger than the vane diameter. He employed for his experiments automotive greases (represented by a Bingham model). Furthermore, he reports he was able to photograph the flow in the vane rheometer and that the fractural surface was approximately cylindrical, but this is not clear how it was conducted.

Although he affirms that he got good agreement between his experimental and numerical works he did not find any theoretical relationship between theory and experiment. For example, the fact that the shearing–surface diameter increased in experiments linearly with the ratio yield–stress to plastic viscosity but numerical simulations showed the contrary, an exponential decrease with increasing ratio yield–stress to plastic viscosity. Despite these discrepancies he recommended the use of the vane for yield stress measurements if a diameter correction is applied.

Yoshimura et al. ([83]) compared the vane technique with other standard methods to measure the yield stress. According to them, values obtained for different oil-in-water emulsions with the vane geometry were of high precision. They pointed out the difficulty in obtaining viscosity information of the fluid after the material starts to flow since the flow field around the vane is quite complex.

Haimoni et al. ([39]) performed yield–stress measurements with a six–bladed vane on a cement slurry. It is well known that cement slurries change their behavior from liquid to solid in matter of hours. Measurements were performed long before reaching the solid state but the samples were given enough time to rest, so that the structures could strengthen. They discuss the shear stress distribution on the vane edges. Different theoretical models to describe this distribution are described: uniform (square), triangular (zero at the vane center having its maximum at the vane tip), parabolic or exponential.

In order to have an uniform stress distribution a large ratio height–to–diameter seems to be required. On the other hand if this ratio is small (less than 2.0) the stress distribution should deviate strongly from a square–uniform distribution and tends to become triangular, depending on the type of material. In practice these distributions will deviate along the vertical and the horizontal edges of the vane, depending on the type of material. They compared all measurements with a bob–in–cup rheometer and attributed the differences between both to slip at the bob.

Barnes [11] carried out simulations with a FE code for a four-bladed vane and a power-law fluid (shear thinning, index $n \leq 0.5$). He compared his results with those obtained with a bob-in-cup geometry. The shear stress calculated at the cup wall was equal for both geometries for a given rotational speed. He obtained equivalent flow curves at low shear rates with the same fluid but a sudden viscosity drop was found with the bob geometry at low shear rates. This effect was attributed to wall slip. Since this effect was not observed with the vane he noted this geometry as a valuable tool when slip occurs.

Alderman et al. ([2]) performed experimental investigations to measure the yield stress of aqueous bentonite clay suspensions. They found that there is no end contribution from the blades for the lower yield stress muds something that is different with the findings by Nguyen et al. ([59]). A comparison with a Carrimed bob-in-cup rheometer suggests that the vane technique may be suitable only for yield stresses greater than a minimum value, most likely dependent on the number of blades. The accuracy of the measurements was not only attributed to the number of blades (a four bladed-vane was used) but also to the concentration of the suspensions. The failure of the measurement for lower concentrations was attributed to the simplified assumptions in the vane technique. For high concentrations the divergence in the measurements between the vane-in-cup and the bob-in-cup geometries was attributed to slip at the walls of the last system.

The results of Alderman et al. ([2]) provided an important basis for Sherwood et al. ([72]). Sherwood et al. showed that the vane could not only be used to measure the yield stress of concentrated suspensions but also to obtain the shear modulus of the suspension (treated as a linear-elastic solid) in small deformations. Sherwood et al. studied different N-bladed² configurations of the vane imposing slip and non-slip conditions for each different case. With the use of a complex variable analysis they came out with certain simplified results for 2,3,4, and 6-bladed vanes. Their results show that despite the simplicity of the geometry of the vane the mathematical analysis of the vane is not trivial and for practical purposes assumptions and / or simplifications are necessary.

Castell-Perez et al. ([23]) performed a series of measurements with 10 different vane geometries. The height of the vane was kept constant while the ratio vane-diameter to cup-diameter was varied. Their results show that shear rates evaluated with an averaged constant were both, geometry and material dependent. Their results are limited to Newtonian and Oswald-de-Waele fluids.

²N denotes the number of vanes.

Atkinson et al. ([5]) went further with theoretical analysis. Using Mellin transforms and the Wiener–Hopf technique they investigated different N-bladed configurations and different boundary conditions. Their interest was the stress distribution and the flow for a 2–D vane.

Briggs et al. ([18]) give an example of the use of the vane in food technology. They consider the vane technique to be advantageous for testing the characteristics of frozen ice cream, mainly for the reason that the vane does not destroy the product structure when the vane is immersed in the sample. Neglecting any end–effects as proposed by Nguyen et al. ([58], [59]), they assumed a solid–body rotation to measure the yield stress of the frozen ice.

Liddell et al. ([62]) performed yield–stress measurements of T_iO_2 suspensions with the vane geometry under the same solid–body rotation assumption. They pointed out that this assumption is "slightly incorrect". Although Nguyen et al. ([59]) have already addressed a non–uniform stress distribution at the ends of the imaginary circumscribed cylinder and Alderman et al. ([2]) minimize its influence on the measuring of the yield stress. Results of Liddell et al. agree only in part with it. According to them the size of the vane will affect the required torque for a given stress but it does not change the development of stress. Thus, the vane dimensions should be immaterial in determining the yield stress.

Yan et al. ([80]) used a commercial finite–element package (FIDAP) to model the behavior of Herschel–Bulkley, Casson and a Maxwell type fluids within a domain of 1300 elements. They assumed a shearing surface located on a cylinder whose dimensions correspond to those of the vane, an uniform shear–stress distributed on this surface being equal to the yield stress and no secondary flows between the vane blades.

Results from Keentok ([48]) are criticized since the way the yield surface is determined is not shown, furthermore, the number of elements between the blades is too coarse (there were only four elements). For this reason, no attempt to investigate the nature of the yield area through elastic, viscoelastic and plastic behavior is made.

Characteristics of the flow such as velocities, streamlines, pressure and shear rate are presented. No difference was found between the Herschel–Bulkley and the Casson model regarding the fluid trapped between the vanes while for the Maxwell model differences were found in the strain rate near the vane tips (which does not agree with the cylinder assumption). For the viscoelastic material there is a more or

less uniform distribution of the shear rate away from the tips of the blades. This distribution is explained in terms of the elastic and the viscous part of the shear. That means that the elastic shear is mainly located in the area around the blade tips while the viscous shear is more uniformly distributed along the yield area. The asymmetry in the shear rate distribution found in the numerical simulations is attributed to the effect of elasticity. As a consequence the cylinder assumption would be valid only for certain models, geometry and flow conditions.

Daubert et al. ([28]) related the vane technique when measuring the yield stress to spreadability, a subjective term used in food technology. For a good product, or say, for a spreadable product the yield stress is inverse proportional to the yield stress of the product. Measurements with the vane allowed them to produce "texture maps" easily and avoided disruption of the sample upon immersion of the vane. A total of 13 different products were tested with different vane geometries. To be in agreement with the cylinder assumption they selected radii of the height-to-diameter of the vane greater than 2.0.

Their results of the yield stress measurements indicate that any influence of the end-effects were negligible. They did not use any constitutive models. Paradoxically, some materials that had a low yield stress were able to withstand a large degree of deformation after yielding, suggesting that effects that were not considered in their analysis (e.g. viscosity) play an important role for the vane flow.

Perez et al. ([63]) performed an analysis of the vane geometry with an Arbitrary-Lagrangian-Eulerian (ALE) formulation within a finite element domain consisting of 1492 elements. They presented an analysis of the stress distributions on the shearing surface. Their analysis considered time and size effects, that is, the influence of the rate of rotation of the vane on the surface of shearing. These results show a shearing surface of 1.01 times larger than the vane radius (slightly smaller than that obtained by Keentok et al. ([48])).

Numerical simulations for the 2-D vane geometry depended upon two dimensionless parameters that were represented and limited by inertial and viscous regimes (the last one being typical in vane tests). Before formulating the problem they showed that stress distributions along the top of the vane are not uniform. It was conjectured that material anisotropy and progressive failure are the cause of this non-uniform stress distribution. This suggests that the material model will determine how the stresses are distributed.

When the material is anisotropic the interpretation of the test becomes difficult. For example, the maximum shear can be reached in the vertical surface while the behav-

ior at the top maybe elastic. Since the ratio of both stresses (that at the top and that at the vertical surface) may vary depending on the vane dimensions the influence of the vane dimensions can not be excluded (contrary to the affirmation of Castell-Perez et al. ([23]) and Liddell et al. ([62])). If the contribution of the failure at the top of the vane is dismissed from the total torque (as it has been done usually in practice) then the stress would be underestimated.

Glenn et al. ([36]) tried to obtain device constants for a four-bladed vane in order to obtain averaged shear stresses and shear rates. It was expected that this should lead to the characteristic flow curves of a power-law fluid. The way the constants were obtained was dependent not only on the vane dimensions (again the cylinder assumption is adopted as in [48], [11], [63]) but also on the power-law index n of the material. For the geometries used, the expected behavior is close to the bob-in-cup geometry as n decreases (it is not clear what type of behavior is meant there, probably the characteristic flow curves). Thus, the method used to estimate the device constants would not allow to characterize any type of fluid nor use any vane-geometry due to the dependence upon the type of fluid.

Bravian et al ([15]) used a six-bladed vane with certain slight modifications. For instance, the bottom of each blade was sharpened to reduce sample disruption. To correct deviations from a bob-in-cup system he included a correction factor approximated by a power series. He characterized Newtonian fluids and measured the yield stresses of Power-law fluids in the same manner as carried out by Liddell et al. ([62]).

He noticed the difficulty of defining a shear rate factor due to the non-linearities observed in the curves of shear stress vs. time. Only at the beginning of the linear stress region would it be allowed to introduce a shear rate formulation. The effective radius should be equal to the height of the triangle formed by the tips of two adjacent blades and the corner resulting from the union of the blades.

Rolon-Garrido et al ([69]) studied the non-linear elastic behavior of worm-like micelles in aqueous solutions (cetylpyridinium 100mM / sodium salicylate 60 mM chloride (CPyCl/NaSal) dissolved in distilled water) with a six-bladed vane. This non-linear behavior, characteristic in micellar³ systems, is represented by a non-monotonic flow curve divided into three main regions. The vane technique helped them to establish conditions when the flow became unstable, a condition that depends upon shear rate. They were able to reach shear rates higher than with a cone-

³Micellar solutions can be regarded as dispersions of small particles (usually spheres or ellipsoids).

plate or plate–plate system since for these systems the sample is ejected and slip effects occur.

Farias et al. ([33]) characterized viscoplastic materials with different geometries. Different bob–in–cup systems were used (different heights, lengths, modified surfaces: roughed surface, smooth surface) and compared with a vane geometry (No information is given about how many blades were attached to the shaft). The vane performed better than the cylinder with smooth surface at low shear rates and agreed well with the one with roughed surfaces indicating that it is suitable to eliminate slip–effects. At higher shear rates there were discrepancies between the bob–in–cup systems (roughed and smooth surface) and the vane, discrepancies that were attributed to secondary flows.

Krulis et al. ([49]) approached a four–bladed vane geometry similarly as by Glenn et al. ([36]). They proved that the vane is suitable for food products, analogous to the results of Briggs et al. ([18]).

Another application of the vane for food products was carried out by Martinez–Padilla et al. ([53]). They used the system to characterize two different type of sauces, one that contained fine particles and another with coarse particles. They used two different aspect ratios for the vane–in–cup geometry, one with $\kappa = 1.06$ and a large–gap configuration with $\kappa = 2.0$ ⁴. The vane–in–cup with small–gap used four blades while the one with the larger gap had eight blades (in both cases the blades were equally spaced).

Their measurements were in agreement with measurements performed with the bob–in–cup geometry. As previous works, they based their investigations on the solid body rotation thereby employing a Couette analogy for small and large gaps. Curiously they conclude recommending the vane–in–cup with large κ . It is known that there is no viscometric flow in this system and that Couette approximations in the bob–in–cup system get worse as κ grows. They calculated shear rate and shear stress factors based on the material properties of the investigated sauces departing from a Couette flow and used a correction factor for the shear viscosity as proposed by Bravian et al. ([15]).

Fisher et al. ([35]) used a 4–bladed vane to investigate measurement errors that arise in yield–stress rheometry in modern rheometers as a result of an extra induced torque upon immersion of the measuring device into the cup containing the sample. In most cases a residual torque is not negligible and can be still present if consecutive

⁴ κ is given by the ratio of the outer cylinder to the inner cylinder radius.

measurements are performed with the same sample. This would lead eventually to erroneous measurements and the tests will not be reproducible. Modern equipment have built-in software to set this initial torque to zero at the beginning of the test to avoid or at least to reduce the effect of this additional torque.

For the calculation of the yield stress they use the methodology proposed by Nguyen et al. ([58]) with a vane having a ratio length-to-radius equal 2.0 (l_v/r_v). If the vane is immersed carefully and no stress is induced, using this modern software-feature to zero the initial stress will make no difference. However, if an initial stress is present and this stress is zeroed, errors will not be eliminated from the measurement and any reproducibility will be difficult to achieve.

2.1 Effect of vane dimensions

Previous approaches seem to fit the experimental data for Newtonian fluids well. Although this may be true, one has to notice that the dimensions of the vane are an important factor that can not be ignored nor should be taken arbitrarily especially when the shear rate is calculated under the assumption of a solid body rotation.

Castell-Perez et al. ([23]) investigated 10 different geometric combinations. In their experiments they kept the diameter of the vane constant while the height of the vane and the ratio vane-diameter to cup-diameter was varied in a certain range. They concluded their work affirming that a certain averaged-constant used to estimate the shear-rate changes as the geometry of the system is modified and / or the material properties change. They used Newtonian and Ostwald de Waele fluids.

An important aspect in the measurement of the yield stress is the minimal influence of the vane dimensions. Liddel et al. ([62]) have performed measurements of the yield stress for different suspensions. In their work they compare the results of other researchers with their results (see for example [58], [83]) to show that the vane dimensions have little effect on the measured yield stress. The size of the vane affect the required torque for a given stress but do not change the development of the stress. This is in agreement with the definition of the yield stress as a material parameter.

On the other hand, for the viscosity, Castell-Perez et al. ([23]) found differences when estimating the constants to compute the shear-rate, that is, the ratio $\kappa = r_o/r_v$ has an influence on the shear rate. Evidently one expects higher shear-rates for lower values of κ . For accurate measurements the ratio length-to-radius of the vane should be greater than 2 ($l_v/r_v > 2$).

2.2 End effects

In the previous section, works carried out by different researchers have shown how the length of the vane and the outer cup can affect the measurement of the viscosity and that the interpretation of the data may become difficult especially for complex fluids. For a small gap (small κ) these problems can be associated with the ends of the vane (bottom and top). How strong or weak they are will depend on the nature of the fluid, whether it is Newtonian or non-Newtonian, shear-thickening or shear-thinning. It is well known that slip might be a problem when using a Searle or Couette rheometer in a concentrated suspension. In this type of rheometer, the fluid in contact with the bottom contributes a drag which must be matched by the applied torque. The profile of this torque is well described in the annular region (along the whole length l_v of the cylinder) but over the immersed end in an undefined way. If the gap width is kept small enough so that $r_o - r_v \ll r_o$ then the above problem is reduced since the contribution of the bottom becomes negligible ([66]).

Ideally in these conditions the shear stress at the outer wall is:

$$\tau_o = \left(\frac{r_v}{r_o} \right)^2 \tau_i. \quad (2.1)$$

Here τ_i is the shear stress at the inner wall.

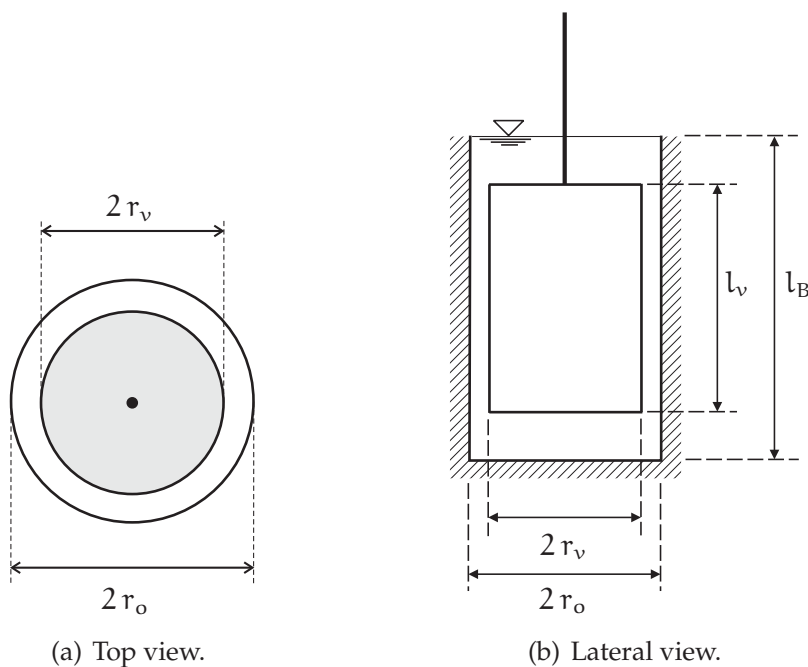


Figure 2.1: Bob-in-cup geometry.

Solutions proposed for the bob-in-cup geometry, used to account for end-effects cannot be applied to the vane-in-cup system. Instead one would have to determine experimentally the end-effect. In this procedure the torque M applied to the rotating-vane at an angular velocity Ω is determined as a function of the height of the vane immersed in the fluid ([11], [20]).

If the height l_v of the vane is long enough compared to the vane diameter $2r_v$ one may assume that the deformation of the fluid around the vane is independent of position along the vertical axis of the vane (two-dimensional). This situation correspond to a problem of plane strain ([72]). The effect above and below the vane is unknown.

Sherwood et al. ([72]) show that for the fluids used by them there is no tendency for tangential slip. However, they say, there may be a tendency for separation to occur at the tips (trailing face of the vane) where the material is in tension.

2.3 Scope of the thesis

The vane flow is mathematically complex. All investigations carried out by other researchers in the past whether experimental, theoretical or numerical in nature, have shown that the vane flow –besides yield stress measurements– is up to now not a tool used for viscometric measurements for any type of material.

No method employed until now is capable of using the vane as a viscometer, independently of the fluid model. This limitation is, in great part, due to the assumption of a solid-body behavior as the vane rotates. A consequence is that the Couette analogy used to estimate the shear-rate or the shear-stress would deliver wrong values if a different material is used at the same flow conditions. Correction factors will not solve the issue. The problem is just of another kind since no viscometric flow governs the vane flow.

The main goal in this thesis is to find out if the vane can be used as a viscometer and if so under what conditions and limitations. Investigations are performed experimentally and numerically .

Experiments are carried out with a four-bladed vane adapted to a commercial rheometer (UDS 200, Physica-Paar). These experiments are divided into two parts: rheological measurements and flow visualization.

The rheological characterization consists of determining the flow curves and their corresponding rheological models for different aqueous polymeric-solutions. Flow

visualizations are accomplished with the particle–image velocimetry technique (PIV). The visualizations should serve to compare the flow conditions in the vane with the simulated models.

Numerical simulations are implemented with a commercial package (CFX) based on the finite volume method (FVM). Since no viscometric flow occurs we do not assume a solid–body rotation in any part of the work. This should lead to a fluid–independent way of using the vane as viscometer. In general terms, both, experiments and numerical simulations should give an insight about the flow.

3 Numerical method

Approximation and integration methods are often used for the solution of the conservative partial–differential equations (PDEs) in fluid mechanics.

A numerical simulation in fluid mechanics can be divided into three main parts. First, the physical problem is modeled with (a set of) PDEs. Next, the numerical–method to be used has to be specified in order to give the solution of the PDEs according to their boundary and initial conditions. This is based on a linearization process and a finite approximation (discretization) of the PDEs as well as the solution of the resulting algebraic system of equations. The third step covers the evaluation and visualization of the numerical results.

In this thesis a commercial software based on the finite volume method (FVM) has been used to solve the system of governing equations. In this method, the conservation and transport equations have to be written in integral form. Flux balances for the mass, momentum and /or energy have to be approximated on the finite–volume elements (control volumes) defined by the geometry in which the problem has to be solved . One advantage of this method is that the conservative properties of the integral form of the equations are preserved. In other methods, such as finite–difference (FD) or finite–element (FE) methods this is possible only under certain circumstances ([17], [61]).

Within the next sections, the FVM will be described. Detailed information about finite approximations and the FVM can be found in [16], [17], [34] and [61].

3.1 Finite volume method

In principle the vane geometry could be represented by a cartesian mesh. This is of course not suitable since its boundaries –due to the curvature– cannot be accurately matched. Near the cup, the mesh of the vane could be orthogonal in cylindrical coordinates but toward the vane blades this would, due the finite thickness of the blades, lead to non–orthogonal intersection–lines (lines that connect the center of the cell and any bounding face).

Thus, the most practical approach is to use a non–orthogonal mesh for the whole domain with no restriction on the angles of the intersection of the mesh lines. This

ensures a more accurate modeling since the geometry is better matched. The principles of the FVM are independent of the type of mesh. Therefore, the FVM used for rectangular geometries can be used on a non-orthogonal mesh. Non-orthogonal meshes have certain characteristics so that certain extensions need to be considered.

The FVM will be briefly described with a two-dimensional cell-centered mesh. In fig. 3.1 the computational point P is located at the center of the control volume (CV) so that

$$\int_{\Delta V} (\mathbf{x} - \mathbf{x}_P) dV = 0. \quad (3.1)$$

There the control volume is bounded by a set of flat faces and each face is shared by only one neighboring CV.

Other approaches are possible and their implementation depend upon the accuracy sought (first order, second order, etc.) and the way the approximations are carried out (discretization scheme). But independently of the cell-orientation the discretization principle is the same for all variants.

Here cartesian coordinates are used but the numerical grid is non-orthogonal. The difference to orthogonal meshes is that in an orthogonal grid the mass flow in one direction –say the the x -direction– flows in only through one side (the west side) and out only through another one (the east side) –see fig. 3.1, while for non-orthogonal grids all lines have to be taken into account –see fig. 3.1.

By decomposing the unit outer normal \mathbf{n} into its x and y components the contribution of the various sides of the rectangle to the mass flow in the x -direction can be accomplished. The software used automatically accounts for this.

3.2 General transport equation

The general transport equation for any unsteady flow of an incompressible fluid, written in terms of the primitive variable Φ is

$$\partial_t (\rho \Phi) + \nabla \cdot (\rho \mathbf{u} \Phi - \Gamma_\Phi \nabla \Phi) = Q_\Phi. \quad (3.2)$$

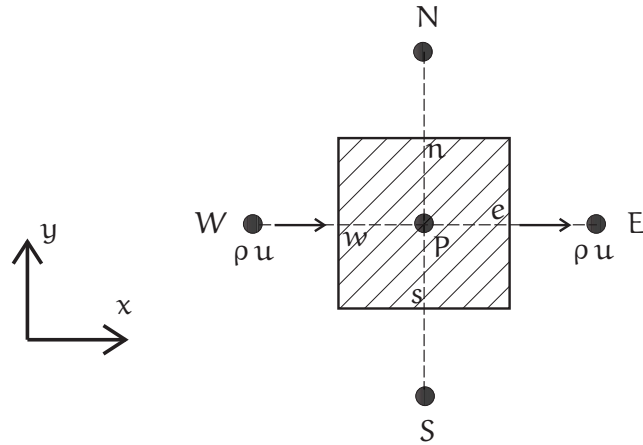


Figure 3.1: Two-dimensional orthogonal control volume and notation used.

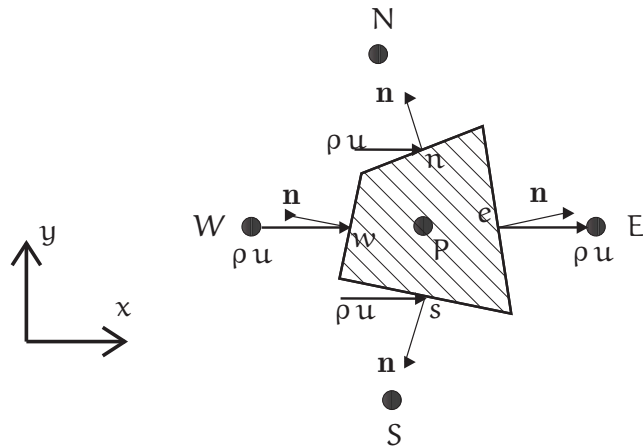


Figure 3.2: Two-dimensional non-orthogonal control volume and notation used.

In this equation, the variable Φ can be a scalar or a vectorial value (e.g. velocity), Γ_Φ stands for the transport coefficient of the transported variable Φ , \mathbf{u} for the velocity vector and ρ for the density. The source term Q_Φ can be divided into its components

$$Q_\Phi^P + Q_\Phi^D = Q_\Phi, \tag{3.3}$$

where Q_{Φ}^P represents the pressure source-term and Q_{Φ}^D the diffusive source-term. The values that each variable can take in previous equations leading to the impulse and continuity equations are summarized in table 3.1.

Table 3.1: Values of the transported variables in the general transport equation (eq. 3.2).

Model		Continuity	x-momentum	y-momentum
All	Φ	1	u	v
	Q_{Φ}^P	0	$-\frac{\partial P}{\partial x}$	$-\frac{\partial P}{\partial y}$
NF	Γ_{Φ}	0	η	η
	Q_{Φ}^D	0	$\eta \begin{pmatrix} \frac{\partial u}{\partial x} \\ \frac{\partial u}{\partial y} \end{pmatrix}$	$\eta \begin{pmatrix} \frac{\partial v}{\partial y} \\ \frac{\partial v}{\partial x} \end{pmatrix}$
GNF	Γ_{Φ}	0	$\eta(\dot{\gamma})$	$\eta(\dot{\gamma})$
	Q_{Φ}^D	0	$\eta(\dot{\gamma}) \begin{pmatrix} \frac{\partial u}{\partial x} \\ \frac{\partial u}{\partial y} \end{pmatrix}$	$\eta(\dot{\gamma}) \begin{pmatrix} \frac{\partial v}{\partial y} \\ \frac{\partial v}{\partial x} \end{pmatrix}$

The corresponding values of the transported variable Φ and the transport coefficient Γ_{Φ} replaced into eq. 3.2 furnishes the momentum equation

$$\rho(\partial_t \mathbf{u} + (\mathbf{u} \cdot \nabla) \mathbf{u}) = -\nabla P + \Delta \cdot \boldsymbol{\tau}. \quad (3.4)$$

3.3 Non-dimensional formulation

For the solution of eq. 3.4 it is necessary to input the different variables such as the density, the viscosity and the velocity in consistent units. We rewrite the governing equation 3.4 in a non-dimensional form to simplify the analysis of the different variables on the flow.

To formulate this equation dimensionless, for each variable will be sought a scaling parameter. For the velocity \mathbf{u} and the length (radius r) it is reasonable to scale with the angular velocity Ω and the diameter of the vane d_v , respectively, as

$$\mathbf{u} = \Omega d_v \mathbf{u}^*, \quad r = d_v r^*. \quad (3.5)$$

The remaining variables time t , shear stress $\boldsymbol{\tau}$ and hydrodynamic pressure P are scaled similarly. For that we choose the angular velocity and the effective viscosity of the fluid η_{eff} . For the pressure P we use a parameter Π .

$$t = \frac{t^*}{\Omega}, \quad \boldsymbol{\tau} = \eta_{eff} \Omega \boldsymbol{\tau}^*, \quad P = \Pi P^*. \quad (3.6)$$

After replacing these non-dimensional variables eq. 3.4 becomes:

$$\underbrace{\frac{\rho d_v^2 \Omega}{\eta_{eff}}}_{Re} (\partial_t \mathbf{u}^* + (\mathbf{u}^* \cdot \nabla) \mathbf{u}^*) = - \underbrace{\frac{\Pi}{\eta_{eff} \Omega}}_{=1} \nabla P^* + \Delta \cdot \boldsymbol{\tau}^*. \quad (3.7)$$

The term $\frac{\rho d_v^2 \Omega}{\eta_{eff}}$ in eq. 3.7 represents the Reynolds number. All variables in previous equations with a superscript (*) represent dimensionless quantities.

As $Re \rightarrow 0$ the left hand-side of eq. 3.7 vanishes. Viscous transport dominates over inertia (density plays no role at all). Then we can write

$$0 = -\nabla P + \Delta \cdot \boldsymbol{\tau}. \quad (3.8)$$

This allows us to formulate a quasi-steady numerical simulation for the vane flow in the creeping motion regime.

3.4 Discretization of the general transport equation with the FVM

Previous non-dimensional analysis shows that the density plays no role in the creeping motion regime. Integration of eq. 3.2 over each CV, neglecting inertial terms and replacing Q_Φ with its components given by eq. 3.3 leads, via the Gauss theorem, to the following form:

$$-\iint_{\Delta A} \mathbf{n} \cdot \Gamma_\Phi \nabla \Phi \, dA = \iiint_{\Delta V} Q_\Phi^P + \iint_{\Delta A} Q_\Phi^D \, dA. \quad (3.9)$$

The area of the surface and the volume of the CV is denoted by ΔA and ΔV , respectively. If we assume that the value of the variables at the center of the face and at the center of the CV can be represented by mean values then we can rewrite eq. 3.9 as

$$\sum_b -\mathbf{n}_b \cdot (\Gamma_\Phi \nabla \Phi)_b A_b = Q_\Phi^P \, dV + \sum_b \mathbf{n}_b \cdot Q_\Phi^D A_b. \quad (3.10)$$

Here, b denotes any surface of the control volume, for instance e, w, n or s and \mathbf{n}_b the unit-vector normal to the face b . One has to introduce approximations for the variable Φ on each side of the CV which later have to be interpolated. The interpolation scheme, as we will see in the next sections, establishes a relationship between the value of the variables at the center P of the CV and the neighboring cells $B = E, W, N, S$.

3.5 Discretization of the diffusive flux

Any formulation of the FVM express infinitesimally the conservation principle. These mathematical expressions contain terms that represent, in the case of the general transport equation 3.2, convective and diffusive fluxes through the finite volume.

The total diffusive flux (left hand-side of eq. 3.9) through the faces of the control volume can be obtained by estimating the term $\Gamma_\Phi \nabla \Phi$ over the surface ΔA . This approximation is carried out here by means of the midpoint-rule. In this method, the integral is approximated as a product of the integrand at the center of the face b of the control volume and the face area ΔA

$$- \epsilon_{\Delta A} \int \mathbf{n} \cdot (\Gamma_\Phi \nabla \Phi) dA = \sum_b F_b^D = \sum_b -\mathbf{n}_b \cdot (\Gamma_\Phi \nabla \Phi)_b A_b. \quad (3.11)$$

Equation 3.11 represents the sum of the diffusive fluxes through all the faces of the CV. Integration over the CV leads to the necessity to estimate the derivative of Γ_Φ with respect to the face normal. Here it is necessary to interpolate the diffusion coefficient $\Gamma_{\Phi,b}$ as well as the gradient $(\nabla \Phi)_b$. Normally they can be treated independently from each other. In non-orthogonal meshes the surface vector has components in more than one Cartesian direction and all of its components contribute to the total flux.

The variable $\Gamma_{\Phi,b}$ corresponds to the value of the diffusion coefficient Γ_Φ at the center of the face cell b . On non-orthogonal grids the linear interpolation offers the best compromise among accuracy, generality and simplicity. This linear interpolation is carried out in terms of the neighboring cells (see fig. 3.3).

$$\Gamma_{\Phi,b} = f_x \Gamma_{\Phi,B} + (1 - f_x) \Gamma_{\Phi,P} \quad \text{with} \quad B = E, W, N, S. \quad (3.12)$$

B corresponds to the center of the neighboring cell.

The interpolation factor f_x accounts for the internodal distances. It can be written as

$$f_x = \frac{x_b - x_P}{x_B - x_P}. \quad (3.13)$$

Other higher-order integration and interpolation techniques can also be used resulting in a high usage of computer resources ([17], [34]).

The differencing scheme used in eq. 3.12 to estimate the face value of the diffusion

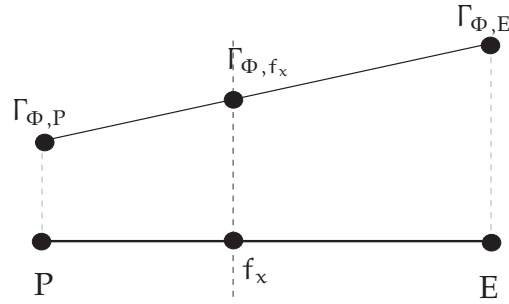


Figure 3.3: Stencil used for the linear interpolation.

coefficient Γ_Φ is called central difference (CD). The CD scheme is one of the simplest methods and frequently used schemes. The linear interpolation approximates the variable Γ_Φ at the CV face b and has second order accuracy. However, this scheme can lead to oscillations (instability).

An alternative to this scheme is the upwind differencing (UD) scheme which is unconditionally stable. The interpolation is performed according to the direction of the flow, thus resulting in a backward or forward-difference approximation. This scheme is first order accurate and tends to be numerically diffusive.

Expressions exist that combine properties of the CD and the UD schemes. In these hybrid approximations a compromise is made between stability and accuracy. The following hybrid equation, often called deferred correction scheme (DCS) is an example.

$$\Gamma_{\Phi,b} = \underbrace{(1 - \gamma)\Gamma_{\Phi,b}}_{\text{UD}} + \underbrace{\gamma\Gamma_{\Phi,b}}_{\text{CD}}. \quad (3.14)$$

The parameter γ , called blend factor, can take values in the range $[0,1]$ (in the present work $\gamma = 1$). For $\gamma = 0$ eq. 3.14 becomes a UD scheme. Thus, the factor γ controls how much diffusion will be introduced.

There are many ways to calculate the derivative normal to the cell face or the gradient vector at the cell center. If the diffusive coefficient is assumed to be constant along the face of the CV then a cell-centered gradient can be calculated and interpolated for the two cells sharing the face (with a linear interpolation, similarly as done with eq. 3.12).

The x -component of the gradient of Φ , say for the east side, can be estimated with a CD scheme:

$$\left(\frac{\partial\Phi}{\partial x}\right)_e = \frac{\Phi_E - \Phi_P}{x_E - x_P}. \quad (3.15)$$

It is assumed that Φ changes linearly between P and E.

3.6 Discretization of the source term

The source term for the equation of motion is of the form

$$Q_\Phi = Q_\Phi^P + \nabla \cdot Q_\Phi^D, \quad (3.16)$$

with Q_Φ^P the pressure source-term and Q_Φ^D the diffusive source-term. One can approximate the pressure source-term (see the first term of the right hand-side of eq. 3.10) by multiplying the source term with the volume of the CV. In this way the gradient of the pressure at the center P of the CV can be obtained with a CD scheme.

For the x -momentum component

$$-\left(\frac{\partial P}{\partial x}\right)_P \cdot dV \approx -\frac{P_e - P_w}{dx} dV = -(P_e - P_w) dy. \quad (3.17)$$

Here dx and dy denotes the length of a face of a CV in their respective Cartesian coordinates. P_e and P_w are the hydrodynamic pressures at the face e and w , respectively. The discretization of the diffusive source-term Q_Φ^D requires, via Gauss' theorem, only areal integration. Treatment of such terms had been shown in previous sections.

3.7 Software used

To solve the set of discretized PDEs obtained (see governing equations in Chapter 4) a commercial package based on the FVM and marketed as CFX version 5.6

was used. This package is modular, i.e., it consists of different elements to perform different tasks such as pre-processing, solving and post-processing. This package offers an all-in-one solution. For the mesh generation and the post-processing additional modules have been used.

For the visualization of the vane-flow Tecplot version 10.0 was used along with Matlab R14 version 7.0. Both applications automated efficiently these laborious tasks. The mesh generation was carried out with another commercial package, ICEM CFD version 5.4. This program allows the mesh to be exported with the specific CFX-format.

3.7.1 CFX package

- **Pre-processing module**

The pre-processing module allows the problem to be set-up. Although the package has only got Newtonian fluids built-in, the user can implement generalized Newtonian fluids. In addition, the discretization scheme, time-steps, boundary and flow conditions are also imposed. The mesh, generated with another commercial package (ICEM CFD version 5.4), can be imported into this module.

- **Solver module**

The discretization process provided by CFX is fully conservative and the solver provides different advection schemes. Available schemes are of first and second order accuracy ('high-resolution'). It is also possible to use a hybrid expression with specific blend. A blend factor $\gamma = 1$ turns the discretization scheme into a second order differencing scheme (see eq. 3.14).

The high-resolution scheme stands for the MUSCL (Monotone Upwind Schemes for Scalar Conservation Laws) approach. This advection scheme is based on a bounded discretization technique to consider strong (sharp) gradients without numerical oscillations¹. This is a TVD-like² discretization with a global second-order accuracy which, according with the convergence criteria, switches to first order upwind scheme locally, in order to prevent oscillations.

The overall solution procedure results in both a high level of robustness and often in a faster convergence than those achieved with segregated solvers (see [65], [51]).

¹This condition depends upon the finiteness of the mesh.

²Total Variation Diminishing.

- **Post-processing**

The huge amount of data resulting from the simulations can directly be exported from this module. With user-scripts and / or user-subroutines in Fortran or Perl, the user is able to extract data from selected regions in the domain. All these allow to automate the whole post-process. Visualization of the flow can also be performed. In CFX the discretization process is fully conservative and the solver provides one with different advection schemes.

An overview of the whole numerics, starting from the mesh generation and going through the set-up of the problem and the iterative process up to the visualization of the results is shown schematically in fig. 3.7.1.

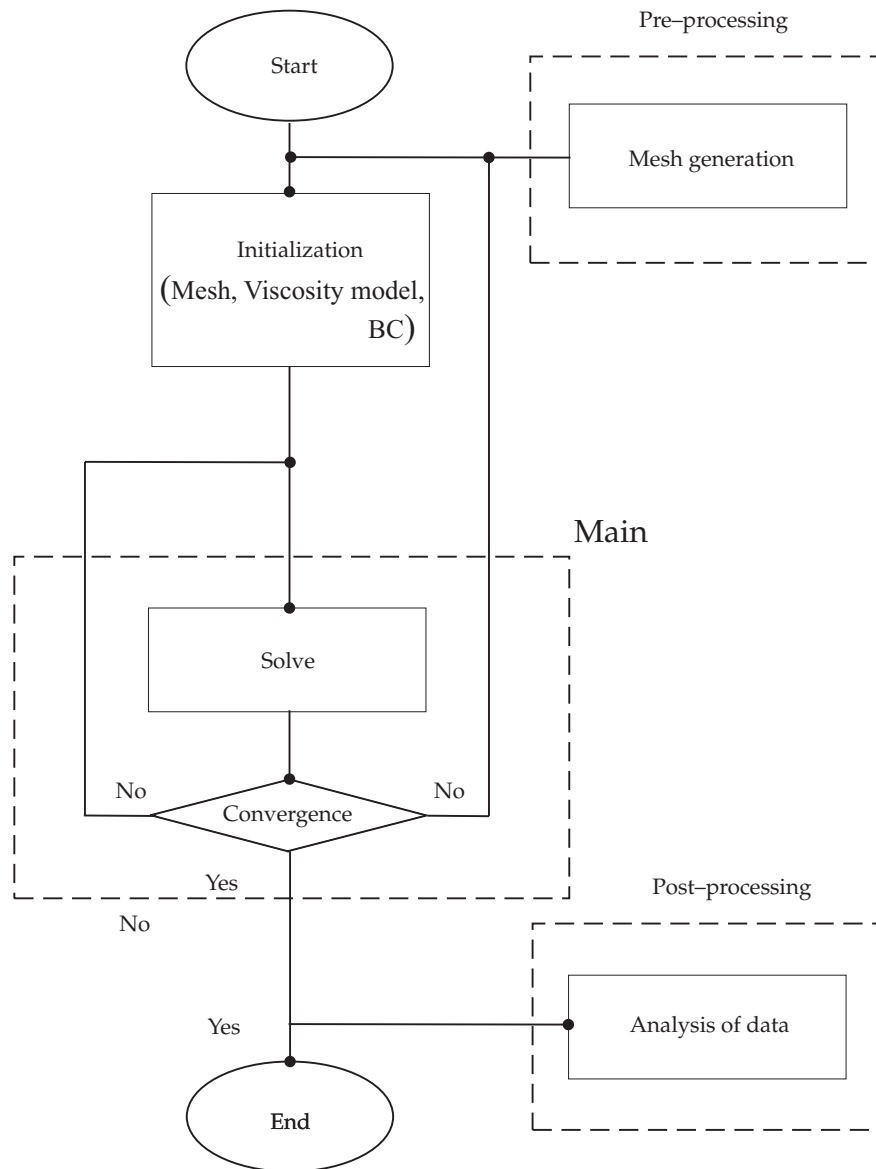


Figure 3.4: Flow chart of the numerical procedure.

4 Vane geometry and statement of the problem for the numerical simulations

If one desires to characterize suspensions, then a vane-in-cup geometry seems to be a better choice over other type of geometries such as the bob-in-cup system . It offers, for example, the possibility of much less disruption to the sample, any effect due to slip can be avoided, and homogeneity of the sample is possible (note that its shape resembles some mixers).

It is almost unavoidable to introduce the vane if one does not mention the principles of rotational rheometers, especially the bob-in-cup geometry, since this system also features a rotating body in a cup. Many of the studies devoted to characterize materials with the vane-in-cup system assume a solid-body rotation within the vane region (see chapter 2).

Thus, before setting up the numerical case for the vane-in-cup geometry it is necessary to introduce its geometrical features and the way it is used and operated in rheological measurements. The governing equations derived from the general transport equation (eq. 3.2) and the boundary conditions that need to be prescribed will be formulated in the next chapters.

4.1 Vane geometry

Simply stated, the vane-in-cup geometry consists of a shaft and a number of N blades attached to it, immersed in a cup (fig 4.2). Typically, it operates in a Searle mode, that is, the inner body (vane) rotates with constant angular velocity Ω relative to the cup. M is the torque required to maintain that situation while the outer cup remains at rest.

4.2 Idealized assumptions

With few exceptions, most of the published work on the rheological characterization of fluids with the vane geometry (radius r_v and height l_v) is based on the assumption of an imaginary rotating cylinder of radius r_v and height ($= l_v$). As a consequence the same equations used to estimate the viscosity with a bob-in-cup system are employed. Anticipating viscometric flow to prevail between r_v and the cup of radius



Figure 4.1: Four-bladed vane used in the present work.

r_o the equation for the shear-stress in such a system (neglecting end effects) is

$$\tau = \frac{M}{2\pi r_v^2 l_v} = c_1 M. \quad (4.1)$$

For the (apparent) shear-rate at r_v one has

$$\dot{\gamma} = \frac{2\kappa^2}{\kappa^2 - 1} \Omega = c_2 \Omega. \quad (4.2)$$

The parameter κ is given by the ratio of the outer radius r_o to the inner radius r_v . The angular velocity Ω is related to the number of revolutions n per second by $\Omega = 2\pi n$.

Equations 4.1 and 4.2 imply for the (apparent) viscosity η

$$\eta = \frac{\tau}{\dot{\gamma}} = \frac{c_1 M}{c_2 \Omega} = \frac{\kappa^2 - 1}{4\pi l_v r_o^2} \frac{M}{\Omega}. \quad (4.3)$$

4.3 Torque on a rotating vane

For a given N bladed vane (fig. 4.3) which rotates with an angular velocity Ω in an unbounded fluid ($\kappa \rightarrow 0$), Akitson et al. ([5]) proposed an equation to evaluate the torque as a function of the number of blades N and angular velocity when the vane is immersed in an incompressible Newtonian fluid of viscosity η .

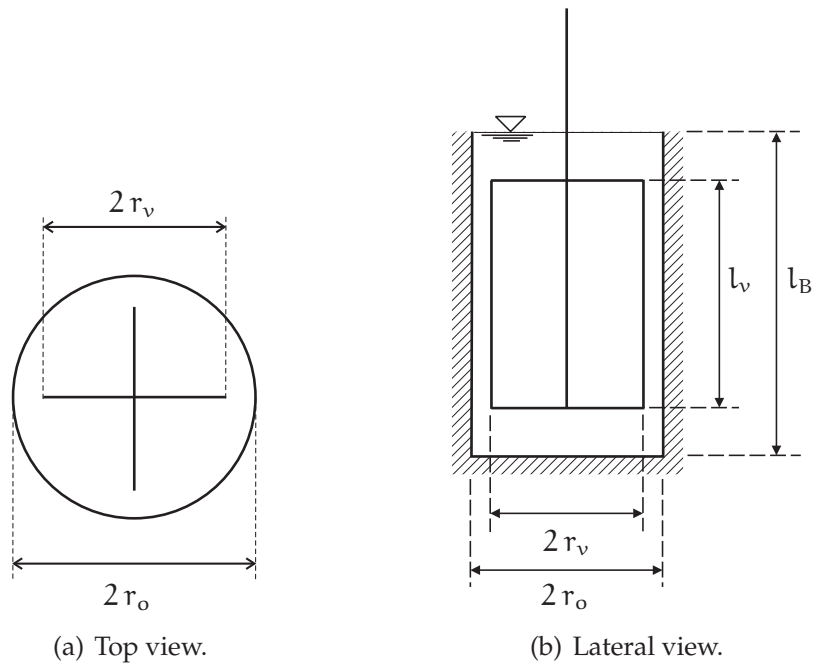


Figure 4.2: Schematic representation of a four-bladed vane-in-cup geometry.

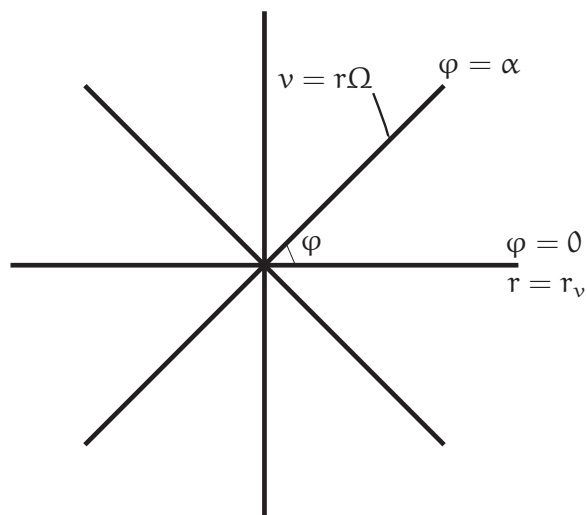


Figure 4.3: N-bladed vane geometry.

This vane has blades of zero thickness, equally spaced around the axis of rotation. The angle that separates the blades is α . Equation 4.4 has been derived with the assumption of a non-slip boundary condition and two-dimensional flow situation in the creeping motion limit.

The equation for the torque per unit length on the vane as a function of the number of blades N has been approximated by ([72]):

$$M \approx 4\pi\eta r_v^2(1 - N^{-1}) \Omega. \quad (4.4)$$

As $N \rightarrow \infty$ Eq. 4.4 turns into

$$M \approx 4\pi\eta r_v^2 \Omega, \quad (4.5)$$

which is exactly the torque on a solid cylinder (see eq. 4.3 in the $\kappa \rightarrow 0$ limit).

4.4 Governing equations

The vane flow is investigated in a laboratory frame. If in the general transport equation given by eq. 3.2 the primitive variable Φ is set equal to 1 (continuity equation) or replaced by the velocity \mathbf{u} and the transport coefficient Γ_Φ by the viscosity function $\eta(\dot{\gamma})$, where $\dot{\gamma}$ denotes the shear rate, one gets the incompressible (mass conservation) equations of motion. In the creeping motion regime we have

$$0 = \nabla \cdot \mathbf{u}, \quad (4.6)$$

$$0 = -\nabla P + \Delta \cdot \boldsymbol{\tau}. \quad (4.7)$$

In this equation P is the hydrodynamic pressure and $\boldsymbol{\tau}$ is the extra stress-tensor which has to be written according to the constitutive equation used. In this work only generalized Newtonian fluids (GNF) are considered, i.e.

$$\boldsymbol{\tau} = 2\eta \mathbf{D}. \quad (4.8)$$

Here \mathbf{D} is the rate of deformation tensor

$$\mathbf{D} = \frac{1}{2} (\nabla \mathbf{u} + (\nabla \mathbf{u})^T). \quad (4.9)$$

The shear rate $\dot{\gamma}$ is written in terms of the second principal invariant I_2 of \mathbf{D} :

$$\dot{\gamma} = \sqrt{-4I_2}, \quad (4.10)$$

with I_2 related to the trace of \mathbf{D}^2

$$I_2 = \frac{1}{2} \text{tr}(\mathbf{D})^2 \quad (4.11)$$

The viscosity function η used fits the Newtonian and or shear–thinning behavior of the fluids employed (details of the viscosity functions are given in chapter 7).

4.4.1 Boundary conditions

In order to save memory and increase the computational speed only a quarter of the whole domain is simulated. Therefore adequate boundary conditions have to be prescribed at the corresponding locations of the domain. To illustrate this, a spatially fixed coordinate system with the origin located at the center of the axis of rotation is used in fig. 4.4.

If the blades have thickness $b_t = 1$ mm, then fig. 4.4 is a sketch of a quarter of the vane–in–cup geometry for this situation.

Wall conditions

At the walls are imposed non–slip conditions. The fluid velocity at the vane surface is:

$$\mathbf{u} = \boldsymbol{\Omega} \times \mathbf{r}, \quad \boldsymbol{\Omega} = \Omega \mathbf{k}. \quad (4.12)$$

Here, \mathbf{u} is the velocity vector and \mathbf{r} the variable radius $\mathbf{r} = (x, y)$. The velocity \mathbf{u} written in terms of its components is:

$$\mathbf{u} = (u_x, u_y) = \Omega (x\mathbf{j} - y\mathbf{i}). \quad (4.13)$$

For the transformations the following relationships are used (see fig. 4.5):

$$\mathbf{e}_r = \mathbf{i} \cos \varphi + \mathbf{j} \sin \varphi , \quad (4.14)$$

$$\mathbf{e}_\varphi = -\mathbf{i} \sin \varphi + \mathbf{j} \cos \varphi , \quad (4.15)$$

which implies

$$\mathbf{i} = \mathbf{e}_r \cos \varphi - \mathbf{e}_\varphi \sin \varphi \quad (4.16)$$

$$\mathbf{j} = \mathbf{e}_r \sin \varphi + \mathbf{e}_\varphi \cos \varphi . \quad (4.17)$$

u_r and u_φ stand for the components of the velocity in cylindrical coordinates, u_x and u_y for the components in Cartesian coordinates. These non-slip conditions are

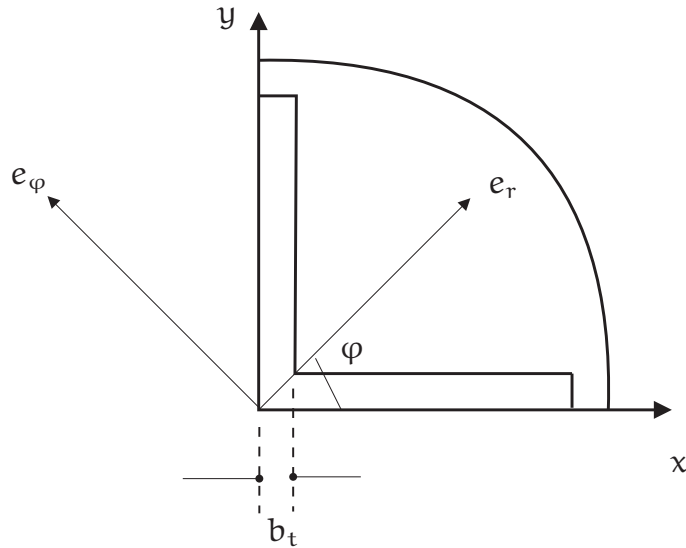


Figure 4.4: Cylindrical coordinate system.

summarized in table 4.1, for the 4-bladed vane flow with blades of thickness $b_t = 1$ mm.

Periodicity conditions

This type of boundary condition reduces significantly the size of the domain. For the vane a pure-periodic BC is used. This means that all dependent variables are

$\mathbf{u} = \boldsymbol{\Omega} \times \mathbf{r}$			
in x-direction			
$\Omega(-y_{00}; x)$	at	$y = y_{00}$	$x_{00} \leq x \leq r_v$
$\Omega(y; r_v)$	at	$x = r_v$	$0 \leq y \leq y_{00}$
0	at	r_0	
in y-direction			
$\Omega(-y; x_{00})$	at	$x = x_{00}$	$y_{00} \leq y \leq r_v$
$\Omega(-r_v; x)$	at	$y = r_v$	$0 \leq x \leq x_{00}$

Table 4.1: Non-slip boundary conditions

identical and repeat periodically at the specified locations. These conditions are imposed at locations ① and ② (fig. 4.5).

For the velocity at locations ① and ② this means:

$$(\mathbf{u}_r; \mathbf{u}_\varphi) \Big|_{\textcircled{1}} = (\mathbf{u}_r; \mathbf{u}_\varphi) \Big|_{\textcircled{2}} . \quad (4.18)$$

\mathbf{u}_r and \mathbf{u}_φ are:

$$\mathbf{u}_r = \mathbf{u} \cdot \mathbf{e}_r = (u_x \mathbf{i} + u_y \mathbf{j}) \cdot \mathbf{e}_r = u_x \cos \varphi + u_y \sin \varphi , \quad (4.19)$$

$$\mathbf{u}_\varphi = \mathbf{u} \cdot \mathbf{e}_\varphi = (u_x \mathbf{i} + u_y \mathbf{j}) \cdot \mathbf{e}_\varphi = -u_x \sin \varphi + u_y \cos \varphi . \quad (4.20)$$

At ①: $\varphi = \frac{\pi}{2}$

$$\mathbf{u}_r = u_y; \quad \mathbf{u}_\varphi = -u_x \quad (4.21)$$

and at ②: $\varphi = 0$.

Then it follows that

$$u_r = u_x; \quad u_\varphi = -u_y. \quad (4.22)$$

Finally:

$$u_r \Big|_{\textcircled{1}} = u_r \Big|_{\textcircled{2}} \quad \therefore \quad u_y \Big|_{\textcircled{1}} = u_x \Big|_{\textcircled{2}}, \quad (4.23)$$

$$u_\varphi \Big|_{\textcircled{1}} = u_\varphi \Big|_{\textcircled{2}} \quad \therefore \quad -u_x \Big|_{\textcircled{1}} = u_y \Big|_{\textcircled{2}}. \quad (4.24)$$

4.5 Mesh for the vane geometry

The mesh used for the simulations has 10744 nodal points and 13940 elements. It was refined so that any coarseness does not affect the solution or the convergence of the simulations. It can be observed, that there is a higher resolution near the solid boundaries (fig. 4.5).

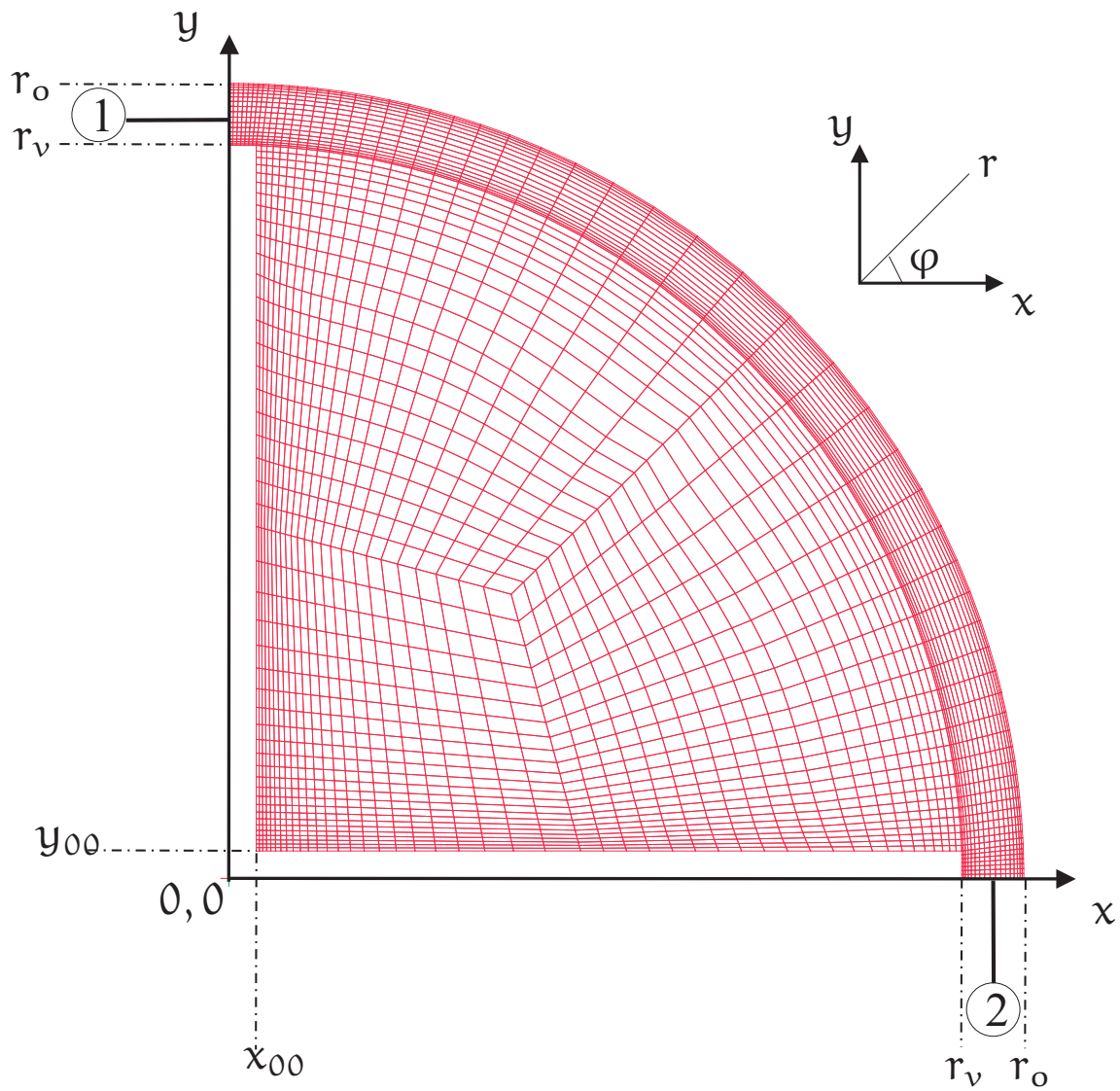


Figure 4.5: Coordinate system and location of boundary conditions imposed on the vane geometry (mesh).

5 Optical method

Experimental flow visualization is often used in fluid mechanics to gain insight of the structure of the flow. In optical tracer-based methods, light-reflecting particles have to be added to the fluid. These particles should be small enough to follow the flow but large enough to scatter the light. The light scattered by these particles is recorded, for instance by means of a computer equipped with a digital camera. Depending on the purpose of the visualization further post-processing may be necessary.

Certain methods such as the Laser Doppler Velocimetry (LDV) allow the local velocity of the fluid to be measured. The flow velocity can be measured by using particles as tracers. Tracers (also known as seeding), should not interact with the fluid and should be able to follow the flow. In the LDV technique one measures the velocity only at one specific location.

Other alternatives exist which allow the velocity to be measured at more than one location at the same time. The particle image velocimetry (PIV) has been chosen and used in the present work to perform the visualization of the flow. A commercial equipment fully controlled by a personal computer has been used for the optical measurements. The software provided with the equipment offers different options to perform the set-up and the post-processing (data validation and analysis).

In the next sections the most relevant aspects concerning the PIV technique, the processing of the information obtained from the measurements and its evaluation will be briefly described. References [1], [38], [6], [77] and [79] are recommended sources for information about this technique and its digital manipulation.

5.1 Particle image velocimetry

Particle image velocimetry is an optical measurement technique that allows the experimenter to acquire the instantaneous velocity field in a planar cross-section of the flow. In this technique the velocity of the flow is indirectly measured from the motion of the tracer particles where any velocity lag between the particles and the fluid is neglected (ideal flow). The local velocity of the fluid is given by the displacement of the particles over a certain period of time. Tracer particles are randomly distributed in the flow. In order to perform an estimation of the displacement of the particles within a small period of time statistical analysis is necessary.

To give an overview of the PIV technique, its fundamental steps can be summarized as follows. First, the flow has to be populated with particles that possess light-scattering properties. Particles have to be illuminated so that their movement can be detected by variations of the light intensity. The particles that are observed in the image-plane of the camera lens are stored at different preset times.

The next step is to 'divide' the images taken into subregions (interrogation) in order to increase the accuracy and speed-up the validation of the collected data (data validation). Results obtained with a statistical method are then further analyzed and processed. Schematic representations of a PIV set-up and the technique are shown in figs. 5.1 and 5.2.

5.1.1 Image acquisition

In modern PIV equipments the raw image can be stored on a coupled charged device (CCD¹) for further processing. The light-intensity that has been scattered by the tracer is kept over a small area in the device called pixel². A high number of pixels means high resolution. It is desired to obtain pictures of high resolution so that the small structures of the flow can be captured but this is only possible under certain conditions or is restricted to the characteristics of the flow. But a good CCD sensor is one item responsible for the quality of the shots. The quality of the information that is stored also depends on the objective of the camera, the wavelength of the laser and/or the diameter of the tracer, just to mention a few.

For a good image acquisition, the following parts need to be selected carefully.

- **Seeding**

Images obtained from a PIV measurement are directly proportional to the scattered light. In general, the light scattered by small particles is a function of the ratio of the refractive index of the particles to that of the surrounding medium, the particle size, shape and orientation. For spherical particles with a diameter bigger than the wavelength of the laser, Mie's scattering theory can be applied. For example, silicon-coated particles with a diameter $d_p \approx 10 \mu\text{m}$ can be used for a pulsed laser with a wavelength of 532 nm.

¹The CCD-chip stores and converts light (photons) into electric charge (photoelectric effect).

²Picture element.

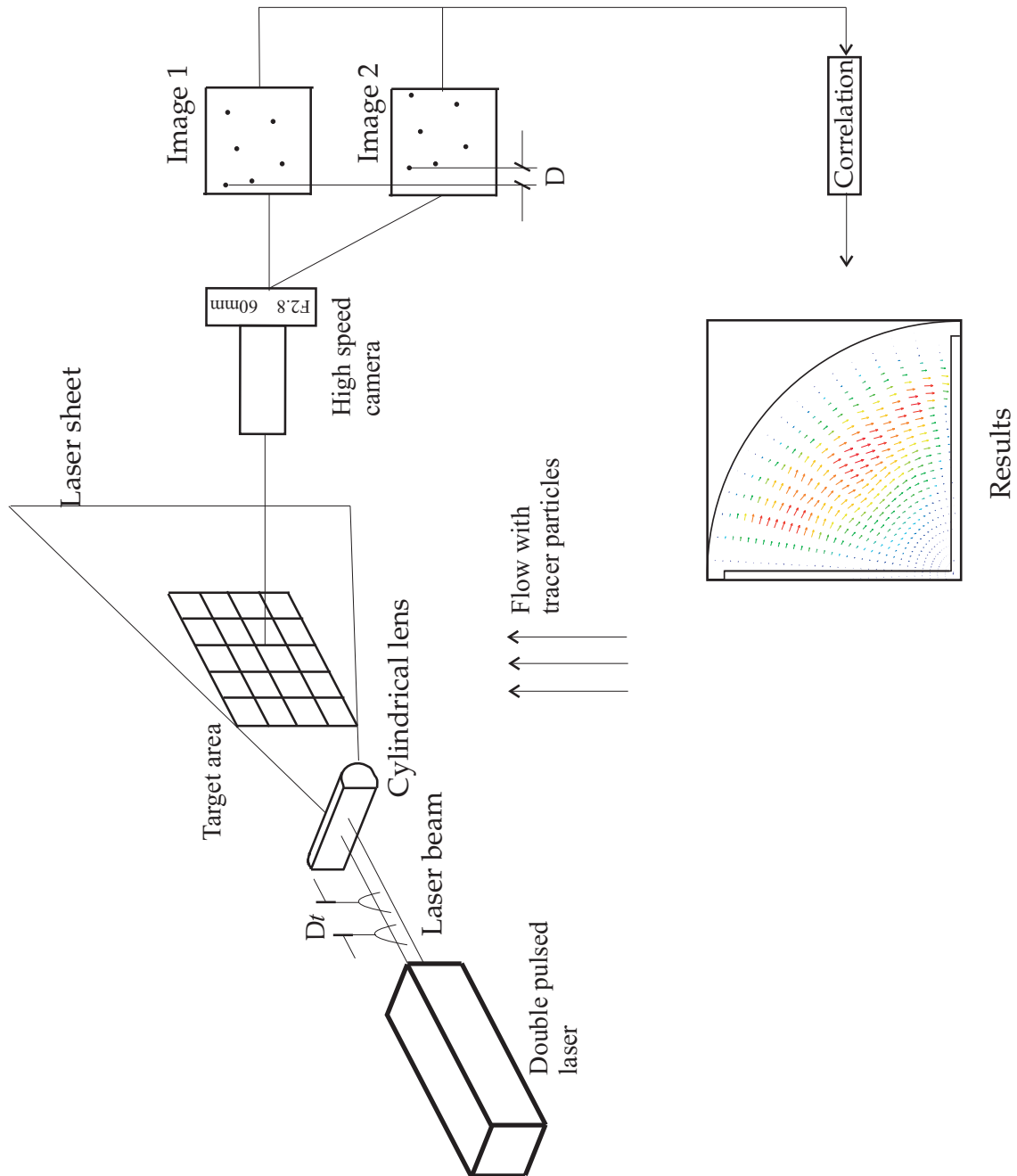


Figure 5.1: Schematic representation of a PIV set-up.

- **Illumination**

Obviously, the light source has to be selected depending on the properties and the geometry of the tracer. The quantity of light that is reflected is important for a successful measurement. Therefore, special attention has to be paid to its selection. The source has to be able to illuminate the particles at a high intensity during a short period of time. Furthermore, the light source must possess certain flexibility to form a thin light-sheet with adequate lenses. Modern PIV measuring devices are equipped with (pulsating) lasers. Thus, a high intensity and a coherent light-beam is guaranteed with these type of light-sources.

- **Imaging**

In PIV, the light-sheet generates a planar cross-section where the tracer particles are projected on a storage medium through (free-aberration) lens. The optical device has a certain numerical aperture and all tracer particles that are in the imaging plane are focused. The imaging obtained is basically a projection of the tracer population onto the planar cross-section. Thus, high quality lenses are mandatory.

- **Registration**

Digital cameras are equipped with CCD-chips whose storing capacity is typically 1000×1000 elements. Therefore, any resulting picture has a matrix of $M \times N$ pixels. One important parameter in the selection of a CCD sensor is its dynamic³ (the capacity of the chip to get the information before reaching the saturation). This fact has a direct relationship with the velocity at which the information can be registered in a short interval of time. In [77] it is shown that the recording of two or more images should require a frame rate equal to Δt^{-1} . There are other factors that the user should also consider such as the sensitivity, noise, image area and pixel size.

5.1.2 Interrogation

To evaluate the information stored in two pictures taken at two different times, t_i and t_e , the picture has to be divided in small regions called interrogation areas. Since each picture has a size $M \times N$, the picture taken at time t_i can be divided in many small parts $f(i, j)$ of equal size (in pixels). The same is done with the second picture

³Manufacturers of CCD use the term 'full well capacity'.

to obtain $g(k, l)$ with a size equal to $f(i, j)$. From both functions a displacement vector $(k - i, l - j)$ necessary to evaluate the velocity can be found.

An evaluation picture to picture would require an enormous amount of time. Thus, one has to compare (correlate) statistically⁴ two pictures that are located in the same global region of size $M \times N$ by using the corresponding interrogations areas.

In standard PIV applications cross-correlation methods are used to estimate the highest matching probability between two functions. Digital pictures are not continuous. Raffel ([67]) defines the cross-correlation for a discrete signal with a finite number of elements as

$$R_{fg}(x, y) = \sum_i \sum_j f(i, j) g(i + x, j + y), \quad (5.1)$$

with x and y the displacement in pixels.

5.1.3 Data validation

One always finds that measurements contain a number of 'spurious' vectors. These vectors deviate from the 'valid' vectors in direction and magnitude. They are originated from regions that do not contain enough particle-image pairs. Despite its occurrence, in practice the quantity of spurious vectors in a PIV measurement is usually less than 5 % ([77]). The occurrence of spurious vectors is almost inevitable even for carefully prepared experiments.

In a post-interrogation process spurious vectors are identified and eliminated from the final data. Experimentally, an increase of the seeding density leads to an improvement of the quality of the resulting data. One should be carefully since an increase of the seeding density (with a fixed size particle) could influence the flow and the optical opacity of the fluid ([77]).

5.1.4 Data analysis

All information gathered from measurements and processed numerically is always treated statistically. The interrogation with high pixel-resolution is relatively slow, therefore a compromise has to be made, for instance, a relatively low-pixel resolution has to be used. Spurious vectors that were found and eliminated have to be

⁴One is looking for two matching regions between both pictures.

replaced. Its replacement is carried out with an interpolation between neighboring vectors.

Fortunately, this number is low and modern equipment can manage this tasks in short time. Many tools are available commercially in order to analyze and report PIV data. The information obtained from PIV measurements, e.g the velocity field, is presented as a picture containing the vectors that represents the velocity. Figure 5.2 summarizes the procedure of the PIV technique.

5.1.5 Displacement of the tracer particles

The velocity is measured indirectly as a displacement of the tracer particle in an infinitesimal time-interval $\Delta t = t_e - t_i$. In the ideal case the tracer velocity is equal to the local velocity of the fluid, however, in practice this can only be approximated.

The displacement of the tracer is given by

$$D(x_i, t_i, t_e) = \int_{t_i}^{t_e} v(x_i(t), t) dt, \quad (5.2)$$

where $v(x_i(t))$ is the velocity of the tracer. In the ideal case the velocity of the tracer is equal to the local velocity of the fluid $u_f = u(x_i, t)$, however, in practice this can only be approximated. Equation 5.2 implies that the displacement field only provides information about the average velocity. Therefore, $D(x_i, t_i, t_e)$ does not lead to the exact value of the fluid velocity but to an approximation.

For an accurate measurement this approximation should lie below an error ε given by the following relationship

$$|D(x_i, t_i, t_e) - u_f \cdot \Delta t| < \varepsilon \quad \text{for} \quad t_i \leq t \leq t_e. \quad (5.3)$$

This error is usually negligible whenever the spatial and time scales of the flow are much larger than the spatial resolution and the exposure time delay of the storing media, and the dynamics of the particles ([1]).

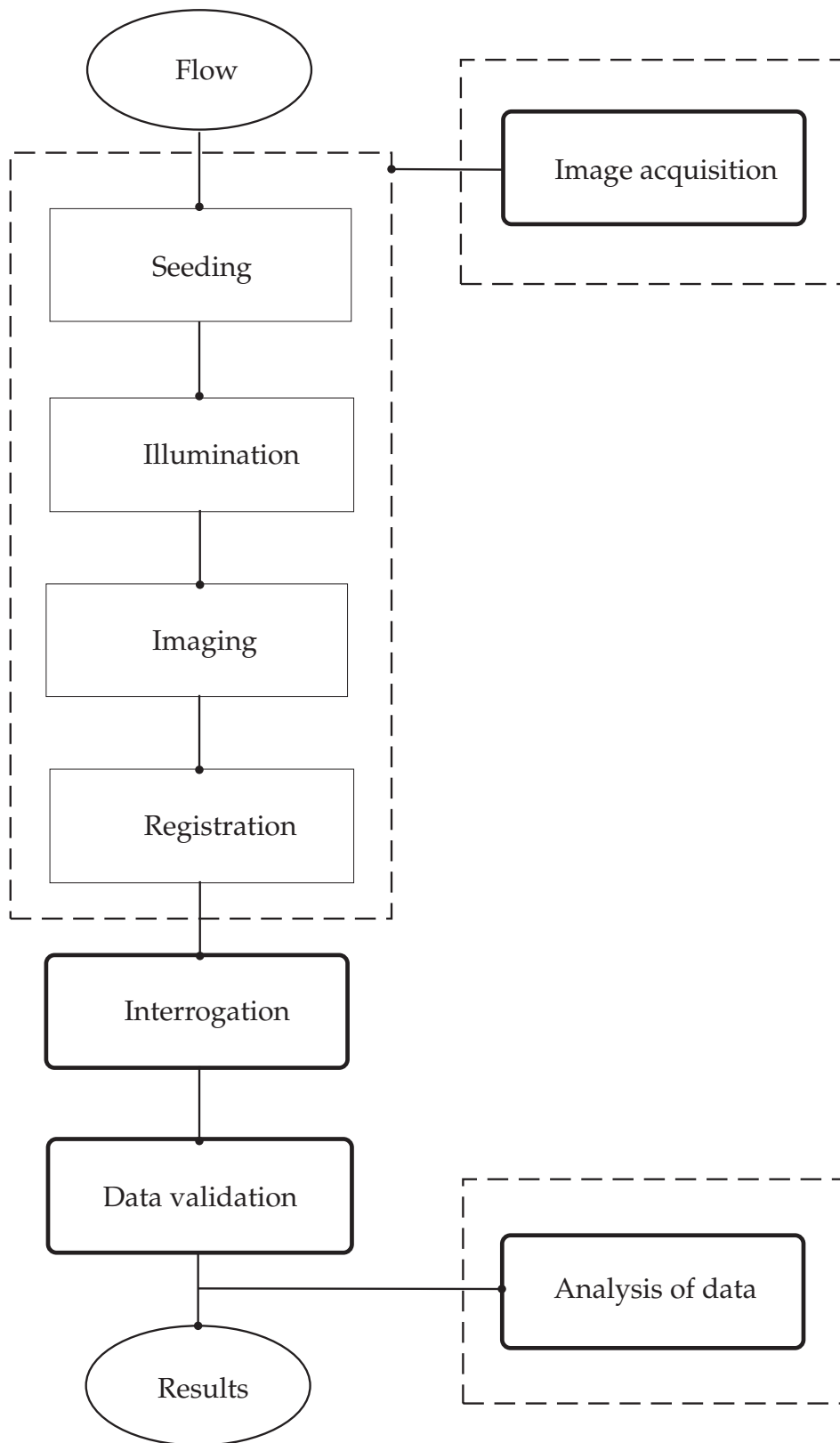


Figure 5.2: Flow chart for the particle image velocimetry procedure.

6 Materials and equipment

6.1 Materials

6.1.1 Newtonian fluids

Silicon oil Silicon oils are long-chain polymers. Their molecular weight (given by the length of the chain or degree of polymerization) governs their behavior. Typically, oils with low-molecular weights show a Newtonian behavior. Another important aspect is that their structure is linear. This implies chemical and thermal stability in a moderate range (i.e. weak dependence of the viscosity upon temperature). Another reason for selecting these fluids is their transparency.

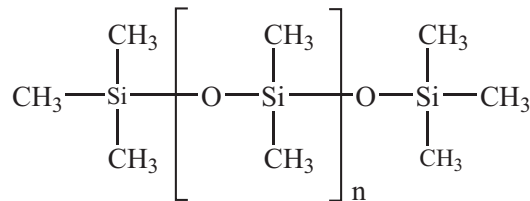


Figure 6.1: Molecule of silicon-oil.

Notation	η (mPa s)
sio20	32.20
sio80	80.00
sio100	122.00
sio350	355.56
sio500	544.20
sio125e3	544.20
sio60e3	57412

Table 6.1: Viscosities of Newtonian silicon oils

6.1.2 Non-Newtonian fluids

Hydroxypropyl guar

Hydroxypropyl guar (hpg) belongs to the family of Galactomannans¹. It is a complex linear-long-chain polymer with a molecular weight of approximately one million kg/kmol. One important property of this material is its high water-binding capacity. Relatively small concentrations of (hydroxypropyl) guar change fluid properties (i.e. increase of the viscosity). It is widely used in the food industry to modify certain characteristics such as texture and/or mouthfeel or in the tertiary oil extraction.

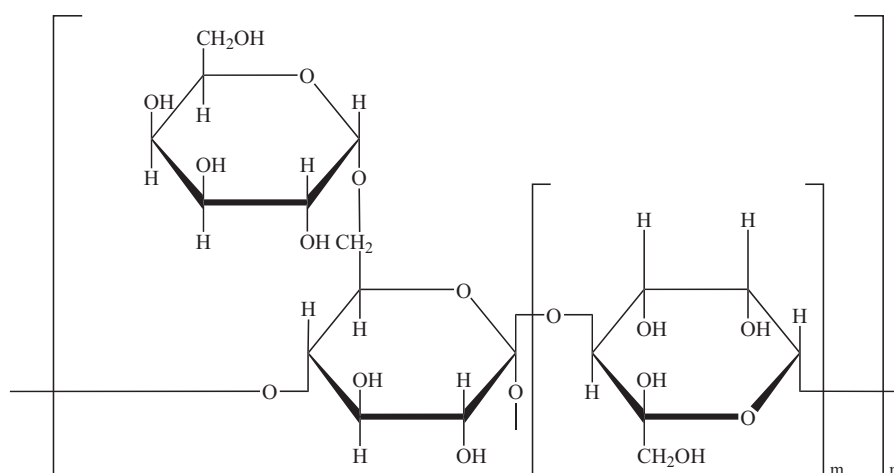


Figure 6.2: General molecule of the Galactomannans. For hydroxypropyl guar $m = 1$.

Hydroxypropyl guar can be obtained by oxydixing the molecule of guar (fig. 6.2), for example, with propylenoxid. In this specific reaction the hydroxyl groups of the galactose and mannose units (ROH) are etherified through an acid catalysis. The steps for this reaction are shown in Figure 6.3.

Xanthan gum

Xanthan gum (xg) is a high molecular polysaccharide produced by the xanthomonas campestris bacteria. Its rheology is of great interest because of its wide use in the

¹Galactomannans are plant reserve carbohydrates. During sprouting (germination), the galactomannans are enzymatically degraded and used as nutrition.

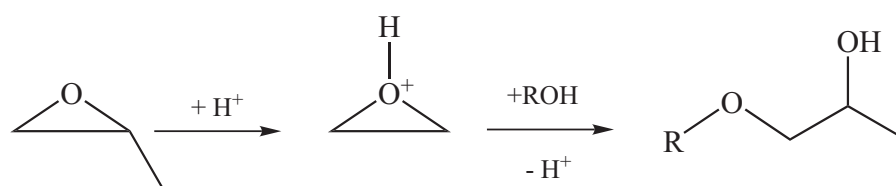


Figure 6.3: Representation of the reaction to obtain hydroxypropyl guar.

food industry. It develops a weak structure in water which creates high-viscosity solutions at relatively low concentrations. It has excellent solubility and stability in acid and alkaline conditions. Xanthan gum is based on a linear 1,4 β -D-glucose backbone (main chain) similar as in cellulose (see fig. 6.4).

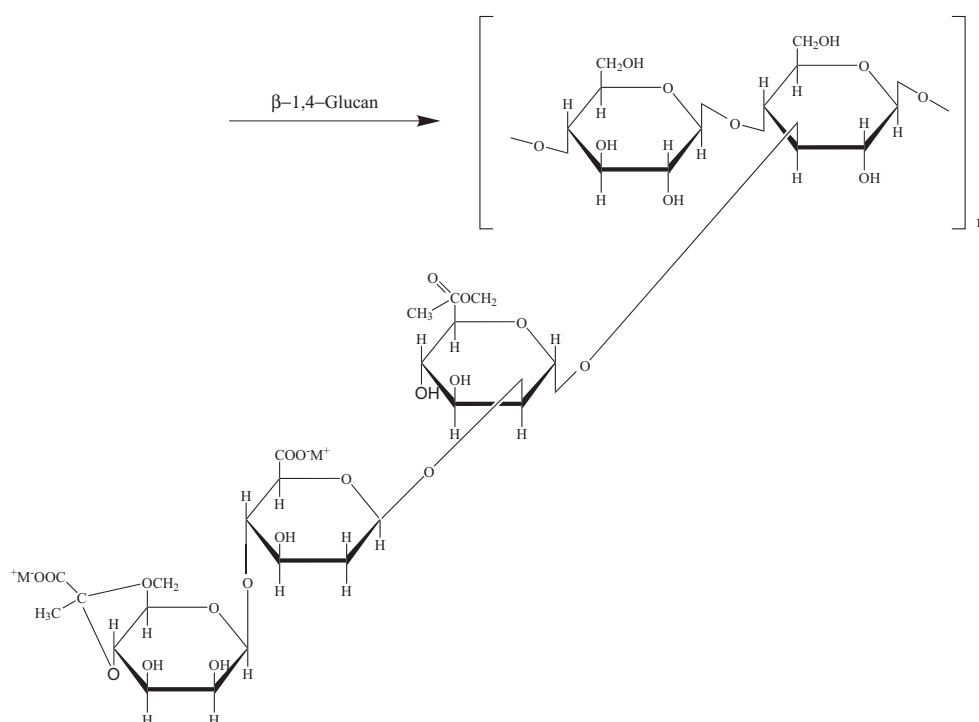


Figure 6.4: Molecule of xanthan gum.

Polyacrylamide

Polyacrylamide is a high-weight acrylate-polymer formed by units of acrylamide. It is highly soluble in water forming a soft gel. It finds application in the treatment

of disturbed soils to avoid or to recover from erosion. In the food industry as a thickener, and in fundamental research in optical measuring techniques such as the Laser Doppler Velocimetry (LDV) or the Particle Image Velocimetry (PIV) due to its transparency.

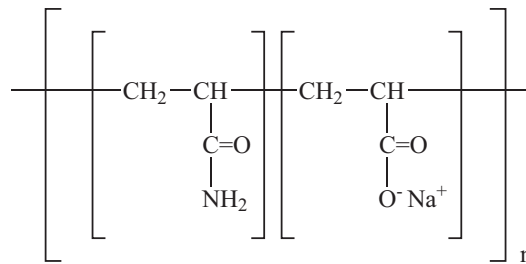


Figure 6.5: Molecule of polyacrylamide.

6.2 Equipment

6.2.1 The rheometer Physica UDS 200

A rheometer manufactured by the company Anton–Paar Messtechnik GmbH, model Physica UDS 200, was used for rheological measurements. It is a Searle–type rheometer and allows modifications of the standard concentric–cylinder measuring system (by exchanging the outer metallic cup by a transparent–glass cup).

This device is able to measure from rather low up to relative high angular velocities (or high shear rates depending on the geometry of the system used). A schematic representation of this rheometer is given in figure 6.6.

Two different measuring–systems have been used in the experimental work. To measure reference values the standard bob–in–cup geometry (CC 27) was utilized. The second geometry, the 4–bladed vane–in–cup, had the same aspect ratio as the bob–in–cup system (i.e. cup–radius to vane–radius) and same length l_v (see figs. 4.2 and 6.7). The same outer cup was used for both, the vane–in–cup and the bob–in–cup system, respectively ². In the following sections these systems are described.

²For rheological measurements the standard metallic cup was kept. During the PIV measurements this cup was exchanged by a transparent–glass cup.

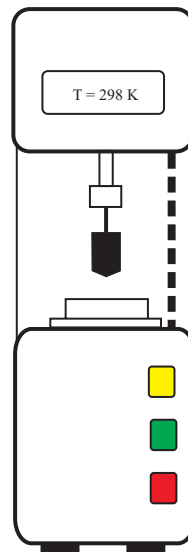


Figure 6.6: Illustration of the rheometer used for the measurements (Physica UDS 200, Searle-type).

6.2.2 Concentric-cylinder measuring system (CC 27)

This system, which is particularly useful when measuring the properties of suspensions has been a standard measuring device for a long time. In the early 20's of the 20th century Mooney ([55], [56]) proposed end-effect corrections which consist in changing the flat-bottom shape of the bob with a conical one (the CC 27 uses this type of modified geometry, [3]). With the corresponding corrections, the shear-stress and the shear-rate can be calculated with eqs. 4.2 and 4.1, respectively.

The influence of the ratio torque-to-angular velocity in a laminar flow, because of end-effects (bottom) and the finite length of the cylinder, basically consist of two parts:

- a) The flow between the ends of the cylinder contributes to an extra torque. Thus, the actual measured torque is higher.
- b) Torques acting within the gap (see fig. 6.7) and the ends of the cylinder are in principle not additive. This is only possible when the profiles of the shear rates at both regions are identical (laminar regime, small κ , large l_v/r_v).

The corrected (representative) shear stress τ is:

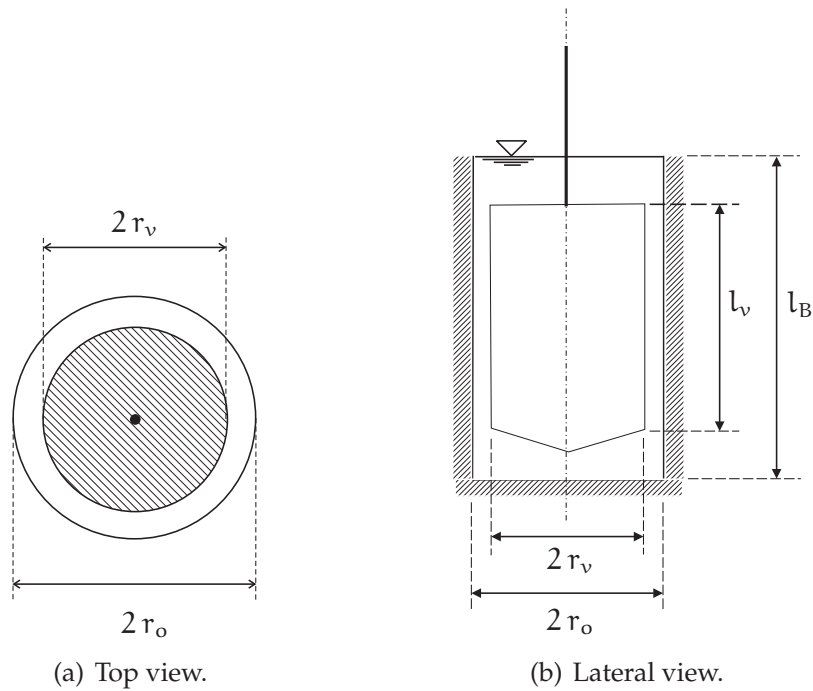


Figure 6.7: Schematic representation of the bob-in-cup geometry (CC 27).

$$\tau = \frac{\tau_v + \tau_o}{2}, \quad (6.1)$$

where τ_v stands for the shear stress at the bob surface and τ_o for the shear stress at the outer wall.

6.2.3 Vane-in-cup measuring system

Equations used for the bob-in-cup rheometer can not be applied to the vane geometry. The vane flow is more complex. Thus, the assumption of an uniform force distribution as for a solid cylinder cannot lead to accurate results. In order to estimate geometric or fluid dynamic constants for this system it is necessary to measure (for example) the viscosity of different fluids with a reference (concentric) rotational-rheometer. In chapter 8 we show our approach to estimate the device constants for the vane-in-cup necessary to calculate a representative shear-rate and the viscosity of the fluid.

A representative shear rate $\dot{\gamma}$ sought for the vane geometry can be written as

$$\dot{\gamma} = c_{\gamma} \Omega . \quad (6.2)$$

And similarly for the shear stress:

$$\tau = c_{\tau} M . \quad (6.3)$$

c_{γ} and c_{τ} are constants of the system, Ω and M the angular velocity and the torque exerted on the vane, respectively. The dimensions of the vane geometry utilized in the present work are summarized in table 6.2.

Radius r_v (mm)	Height l_v (mm)	Thickness b_t (mm)	Radius of the cup r_o (mm)
13.33	40.00	1.00	14.46

Table 6.2: Dimensions of the vane geometry used for the experimental and numerical work.

6.2.4 PIV set-up

As mentioned before in section 6.2.1, the rheometer UDS 200 allowed for some modification in the standard system. The cup used for the PIV measurements was made of plexiglas. In figure 6.8 the PIV set-up is depicted. The whole arrangement consisted of the rheometer UDS 200, a PIV-system produced by the company DANTEC GmbH (for more information on the components see Appendix D) whose parts are a pulsed laser with a wavelength of 532 nm and a HighSense 80C60 CCD camera with a 60 mm Nikon macro-objective. The plane where the laser is located is shown in figure 6.9. Here it can be seen that the plane is located at the middle of the edge of the vane (P). The vane is immersed in the cup up to a distance from the bottom of the cup equal to the radius of the vane r_v . The height of liquid above the upper tips of the vane is also equal to r_v .

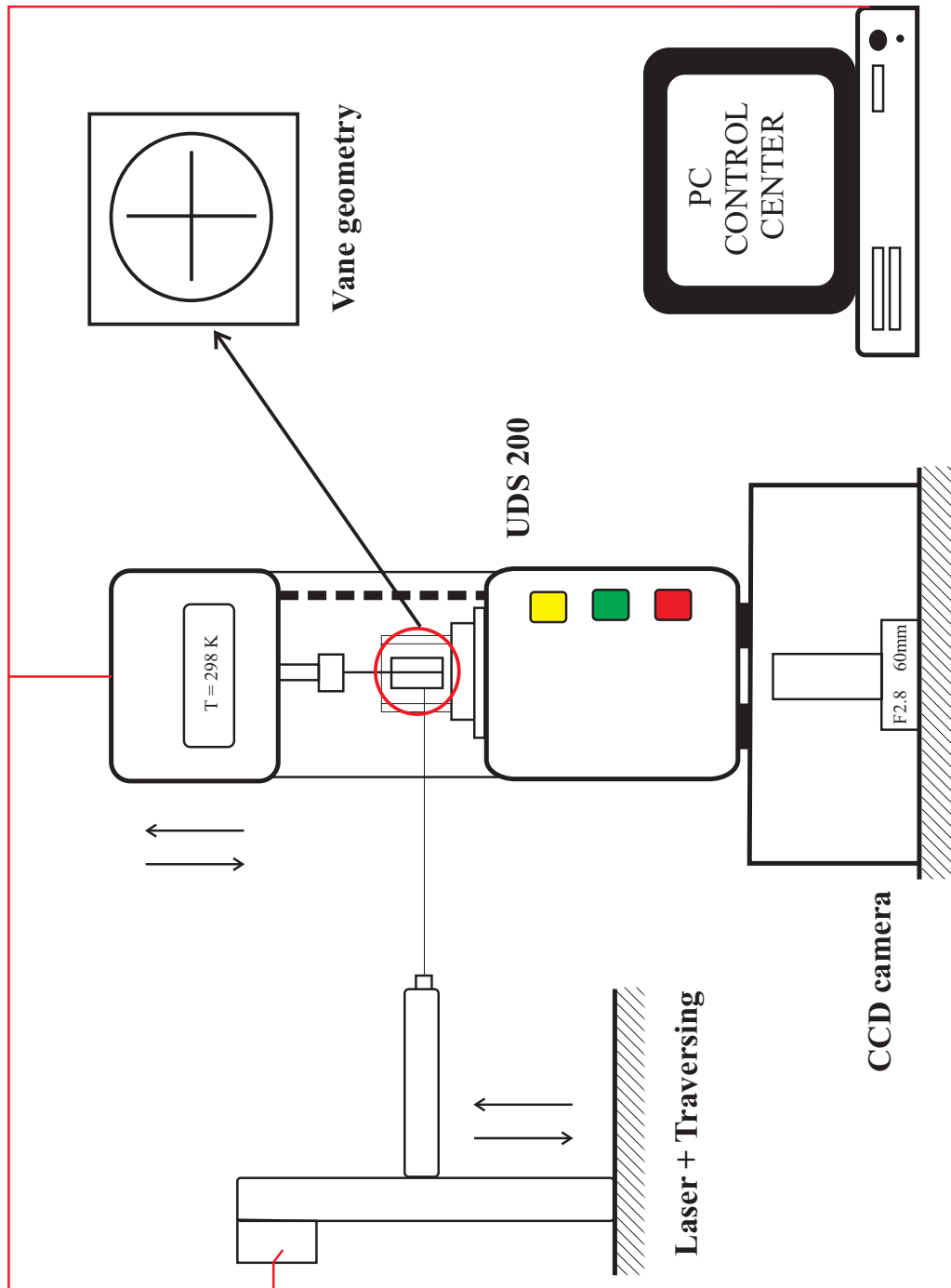


Figure 6.8: Set-up used for the PIV measurements.

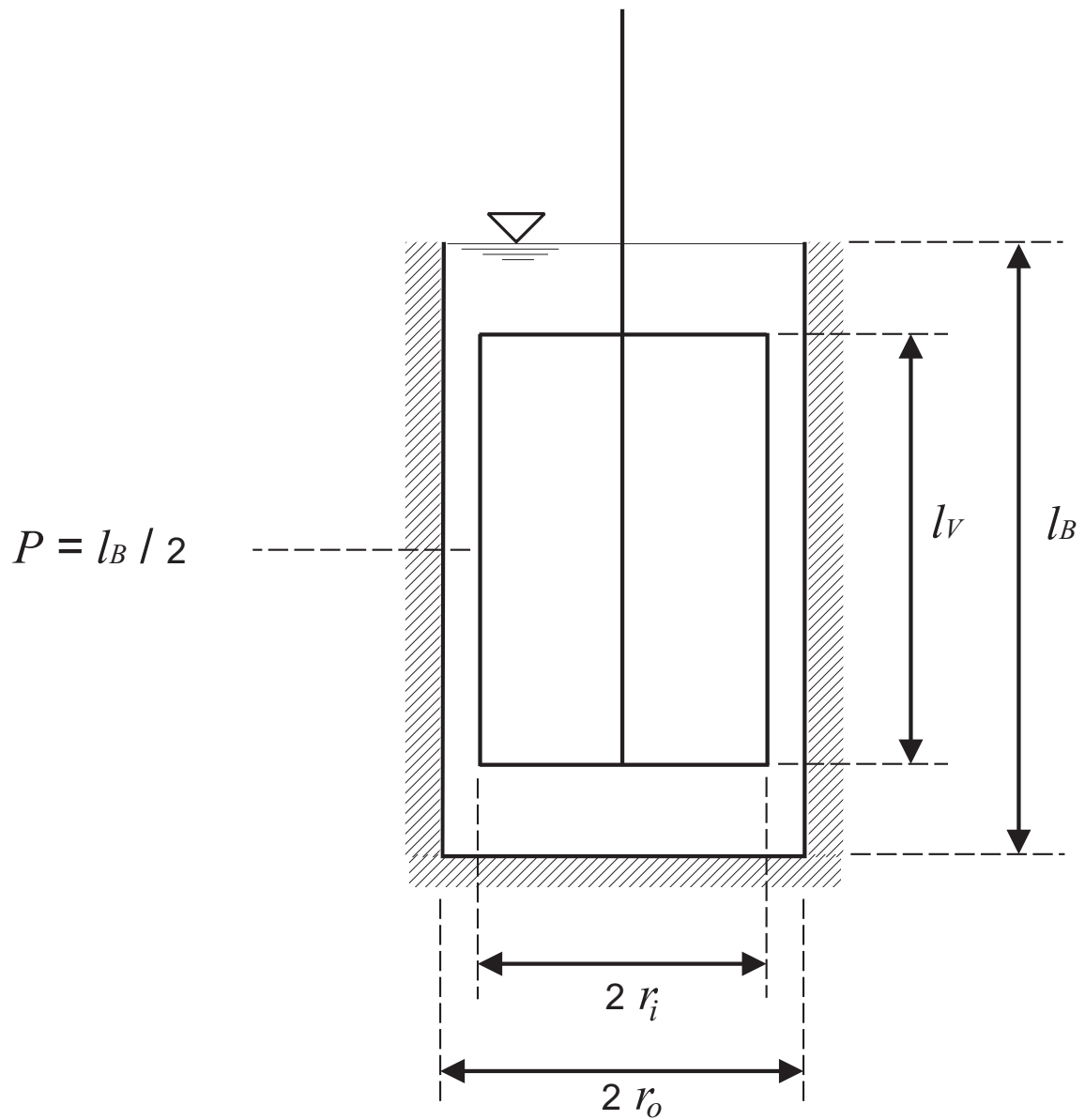


Figure 6.9: Location of the plane for the PIV-measurements in the vane-in-cup system.

7 Flow curves

Most polymeric liquids and suspensions show a shear–thinning behavior in viscometric flow. The intensity of shear thinning can be strengthened by increasing the molecular weight of the polymer and for the case of aqueous solutions by increasing the concentration of the polymer.

Changes in the concentration increase the viscosity at a faster rate. Indeed, there may be cases where viscosity varies proportional to the concentration as to the power 3 or higher ([13]). When flocculated structures occur in the suspensions the apparent phase–volume increases and –as consequence– the measured viscosity is higher than expected. Typically, polymeric shear–thinning solutions will exhibit a first Newtonian region at low shear rates followed by a shear–thinning region (power–law region). In many cases due to experimental limitations it is not possible to reach the second Newtonian region.

In the next sections we show the experimental flow curves and the models for Newtonian and non–Newtonian fluids used by us.

7.1 Newtonian fluids

In chapter 6 we already explained that silicon oil, depending upon its molecular weight, can be classified as a Newtonian or non–Newtonian fluid. For a chain of low–molecular weight, silicon oil shows Newtonian behavior.

The viscosity function is given by:

$$\eta = \frac{\tau}{\dot{\gamma}}. \tag{7.1}$$

Here τ is the shear stress and $\dot{\gamma}$ the shear rate. For a Newtonian silicon oil the viscosity η is independent of the shear–rate (or shear–stress).

7.2 Non–Newtonian fluids

Non–Newtonian fluids in general show a viscosity dependence of the form $\eta = \eta(\dot{\gamma})$ or $\eta = \eta(\tau)$. Many NNF used in industry, research and daily life are of this type. Suspensions or solutions that contain flocs (conglomerates), macro molecules or dispersed solids are of that kind.

The intensity of the applied stress governs the degree of rupture of the structures that give the fluid its representative viscosity. Most NNF are shear–thinning fluids. In [78] models for Generalized Newtonian fluids (GNF) can be found. The models that describe the GNF used in this thesis are the 4–parameter Cross model and the 5–parameter Carreau–Yasuda model.

The Cross model is given by ([27]):

$$\eta = \eta_{\infty} + \frac{\eta_0 - \eta_{\infty}}{1 + (\lambda\dot{\gamma})^{\alpha}}, \quad \alpha > 0. \quad (7.2)$$

Here η_0 represents the zero–shear–rate viscosity:

$$\eta_0 = \lim_{\dot{\gamma} \rightarrow 0} \frac{\tau}{\dot{\gamma}}, \quad (7.3)$$

and η_{∞} the infinite–shear–rate viscosity:

$$\eta_{\infty} = \lim_{\dot{\gamma} \rightarrow \infty} \frac{\tau}{\dot{\gamma}}, \quad (7.4)$$

λ is a characteristic time (transition from the Newtonian plateau to the power–law region) and α a dimensionless parameter that describes the power–law behavior at higher shear–rates.

The Carreau–Yasuda model is:

$$\eta = \eta_{\infty} + \frac{\eta_0 - \eta_{\infty}}{[1 + (\lambda\dot{\gamma})^{\beta}]^{\frac{1-n}{\beta}}}. \quad (7.5)$$

In contrast to the parameter α used in eq. 7.2 for the power-law region, β is used in eq. 7.5 to improve the transition from the Newtonian plateau to the power-law region. In eq. 7.5 $(1 - n)$ is used to predict the behavior in the power-law region.

7.2.1 Preparation of the solutions

All samples were prepared in one liter of deionized water at 298 K¹. To avoid the formation of lumps in the solution, the polymer was added slowly at a constant stirring rate.

The concentration for all solutions was calculated with:

$$[c] = \frac{m_p}{m_s} \cdot 100. \quad (7.6)$$

Here m_p represents the mass of the polymer, m_s the mass of the solvent and $[c]$ the concentration of the solution in w/w%.

Fluid	Solute (g)	Concentration [c] (w/w%)
Hydroxypropyl guar	4.0	0.40
	5.0	0.50
	6.0	0.60
Xanthan gum	2.0	0.27
	2.0	0.33
	4.0	0.40
Polyacrylamide	0.5	0.05
	1.0	0.10
	2.0	0.20

Table 7.1: Different concentrations of polymer solutions used for the experimental and numerical work.

¹With exception of xanthan gum solutions of concentrations 0.27 and 0.33 w/w%, which were prepared in 0.75 and 0.60 liters of deionized water, respectively.

7.2.2 Hydroxypropyl guar

The characterization of Hydroxypropyl guar (hpg) was performed with data obtained from measurements carried out with the bob-in-cup rheometer. The characteristic shear-thinning curves (fig. 7.1(b)) were fitted with the Cross model written in Matlab v7 R14. In this diagram, a strong dependence of the viscosity η on the shear-rate $\dot{\gamma}$ can be observed.

It can be seen that small changes in the concentration of the polymer lead to relatively large changes of the viscosity of the fluid (parameter η_0 is indicative of this). With an increasing shear-rate these curves approach a common value η_∞ .

Fluid	[c] (w/w) %	η_0 (Pa s)	η_∞ (Pa s)	α (-)	λ (s)
Hydroxypropyl guar	0.40	0.15	0.01	0.574	0.029
	0.50	0.33	0.01	0.624	0.059
	0.60	0.69	0.01	0.663	0.111
Xanthan gum	0.27	27.254	0.016	0.777	47.2825
	0.33	102.38	0.016	0.810	129.6086
	0.40	136.94	0.016	0.832	111.2683

Table 7.2: Parameters for the Cross model.

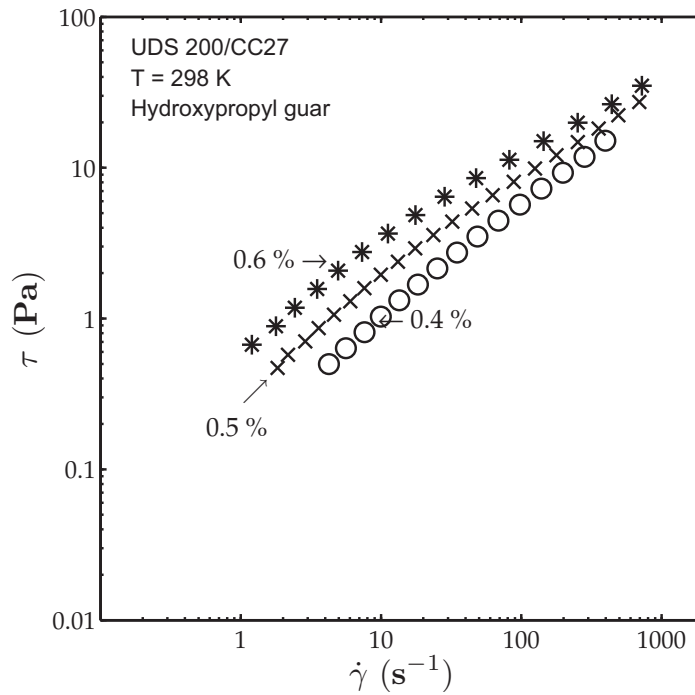
7.2.3 Xanthan gum

The characterization of the solutions of xanthan gum (xg) was performed analogously to the solutions of hpg. In fig. B.1(b) one can observe a similar shear-thinning behavior for moderate low-concentrations.

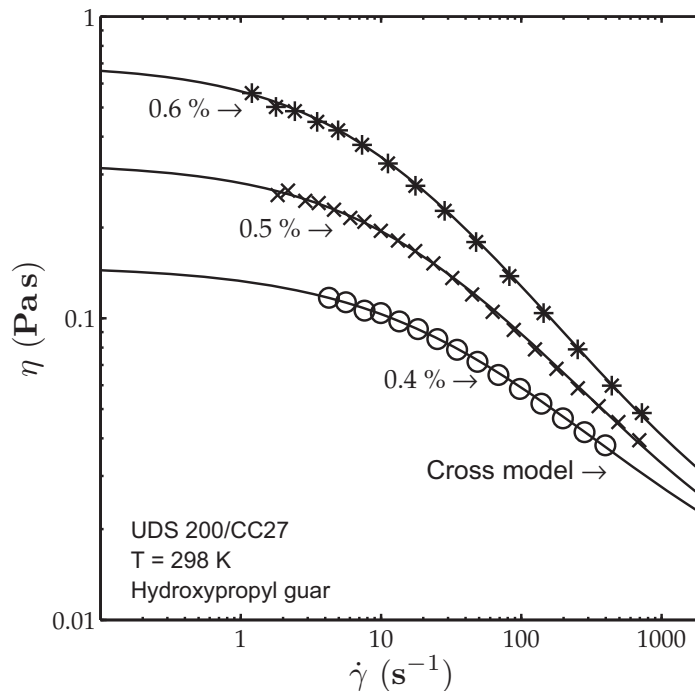
These flow curves were also fitted with eq. 7.2 and Matlab v7 R14. The Parameters that satisfy eq. 7.2 for the experimental data-set are given in table 7.2. Notice that for similar changes on the concentration of the polymers in the solutions (about 20 %), the increase of the viscosity was not as pronounced as those of the hpg solutions (fig. 7.1(b)) for a given shear rate. A predominant power-law region can also be observed.

7.2.4 Polyacrylamide

Polyacrylamide solutions, similarly as the xg solutions, show a predominant shear-thinning behavior for about three decades. The concentrations of the solutions were



(a) Shear stress versus shear rate.



(b) Viscosity versus shear rate.

Figure 7.1: Flow curves for the hydroxypropyl guar solutions.

kept at values much lower than the hpg and xg solutions (0.05 up to 0.20 %).

One reason for this behavior can be attributed to its very high molecular-weight (10^6g/gmol) combined with its linear shape (see fig. 6.5). To approximate the experimental data the Carreau–Yasuda had to be used (fitting the data via the Cross model produced unsatisfactory results). Values of the parameters for this model are given in table 7.3.

Fluid	[c] (w/w) %	η_0 (Pa s)	η_∞ (Pa s)	λ (s)	β (–)	n (–)
Polyacrylamide	0.05	4.7122	0.0180	31.32	1.5	0.28
	0.10	8.7438	0.0180	31.23	1.5	0.28
	0.20	27.63	0.0180	48.64	1.5	0.28

Table 7.3: Parameters for the Carreau–Yasuda model.

7.3 Characterization with the solvent viscosity

We have seen in previous sections that the aqueous polymer–solutions exhibited a shear-thinning behavior. Such behavior can be seen as being of modest proportions since the concentrations used were relatively small. However, the tendency of the viscosity is to increase as the concentration grows and/or the molecule chain becomes larger (η_0 is an indication of this).

Because of experimental limitations we cannot reach the first and the second Newtonian plateau and it is especially difficult to reach high shear-rates. In general, the shear–thinning behavior of dilute aqueous polymer-solutions and polymer melts (those of very high molecular weight) is qualitatively similar. This behavior is strengthened as the polymer concentration in the solution increases (similar behavior for polymers with large molecule–chains). Notice that as $\dot{\gamma} \rightarrow \infty$ the functional $\eta \rightarrow \eta_\infty$ (see eq. 7.4).

The dissolved polymer contributes to the solution viscosity in a certain amount depending on the concentration (for a given molecular weight). At very high shear-rates, in the hypothetical experimental–case in which the structures are oriented in the flow direction it is expected that the viscosity solution approaches that of the solvent viscosity. There is some evidence ([13]) that even at very high shear-rates the polymer viscosity still contributes to the solution viscosity. In this situation η_∞ will lie between η_0 and the solvent viscosity.

When a model is fitted to experimental data the solvent viscosity can be used to account for shear-thinning effects at high shear-rates. At very high shear-rates the polymer would not contribute to the solution viscosity or its contribution is weak. Figure 7.2 shows the results when the solvent viscosity is used. The parameters are given in table 7.4.

Fluid	[c] (w/w) %	η_0 (Pa s)	η_∞ (Pa s)	α (-)	λ (s)
Hydroxypropyl guar	0.40	0.1462	0.001	0.60	0.02
	0.50	0.3388	0.001	0.60	0.06
	0.60	0.7475	0.001	0.60	0.14

Table 7.4: Parameters for the Cross model when the solvent viscosity is used.

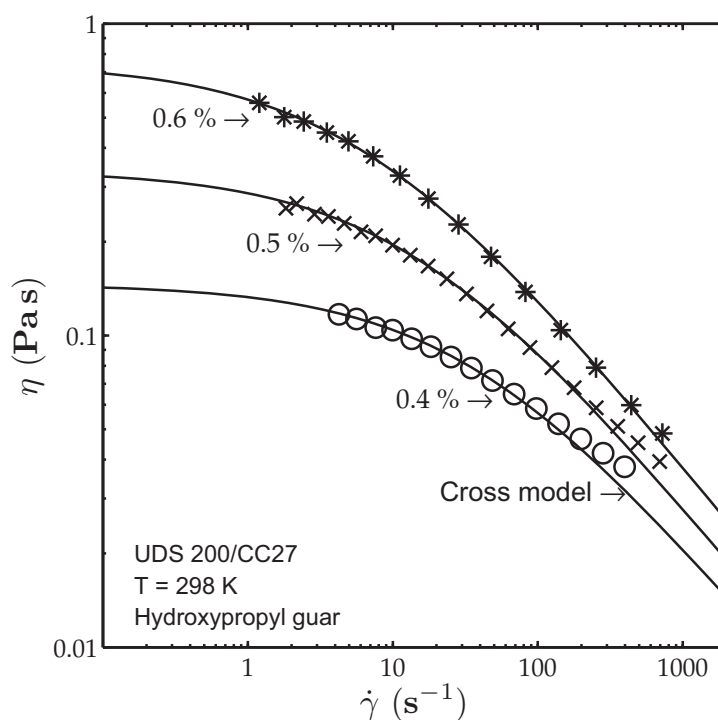


Figure 7.2: Flow curve for the hydroxypropyl guar solutions. The solvent viscosity is used.

8 The vane as viscometer

One of the most important aspects of the vane geometry that has already been mentioned in previous chapters, is the simplicity of its shape. This shape provides the vane certain features that are characteristic in mixing systems ([54],[43],[60],[84],[7]). Typically in mixing operations one is interested in the energy consumption and the degree of mixing.

Obviously this is related to the geometry of the system and the rheology of the materials. For a given system–geometry and material, this relationship cannot a priori be derived, i.e. the dependence of mixing on the energy supplied, since the flow for mixing operations is rather complex and there is no theoretical calculation for the power input ([84], [60]). Dimensional analysis is an important tool to study the flow phenomena for the vane.

8.1 Non–dimensional formulation

Dimensional arguments show that for vane flow of a Newtonian fluid (of viscosity η) the Newton number

$$Ne = \frac{1}{\rho d_v^5} \frac{M}{\Omega^2}, \quad (8.1)$$

must be a unique function of the Reynolds number¹

$$Re = \frac{\rho d_v^2}{\eta} \Omega, \quad (8.2)$$

i.e.

$$Ne = f(Re). \quad (8.3)$$

¹Here we assume constant geometrical dimensions.

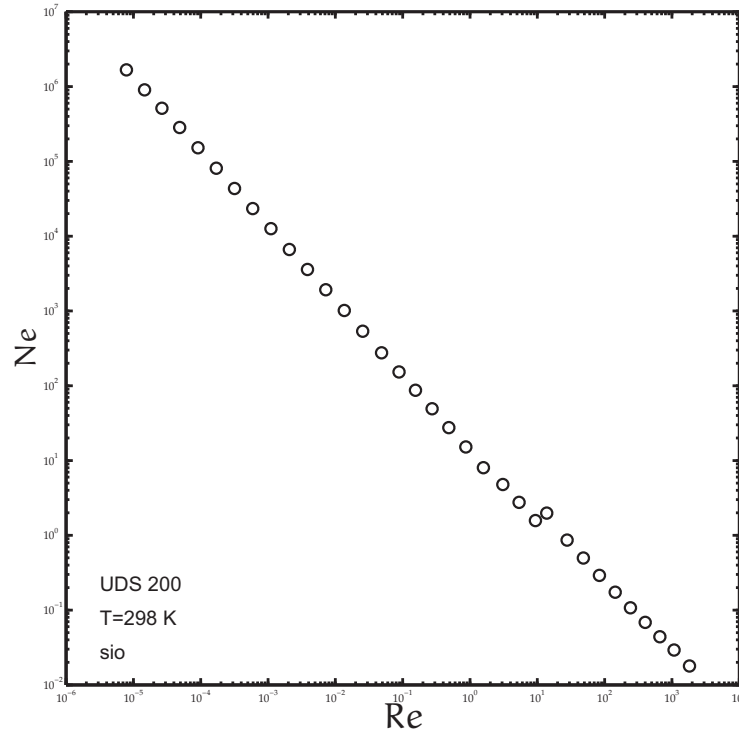


Figure 8.1: Characteristic curve for the vane flow (Ne vs Re).

where M is the torque applied in order to rotate the vane with angular velocity Ω , d_v is the diameter of the vane and ρ and η are the mass density and shear viscosity of the liquid. In the creeping motion limit ($Re \rightarrow 0$) ρ can play no role and $Ne \propto 1/Re$ is the consequence.

Starting from the creeping motion regime ($Ne \propto 1/Re$) the influence of the viscosity diminishes as the Reynolds number increases since $Ne = \text{const.}$ has to prevail for sufficiently high Reynolds numbers (highly turbulent flow).

From now on we shall concentrate on the creeping motion regime (CMR), i.e.

$$Ne = \frac{c}{Re}, \quad (8.4)$$

The constant c crucially depends on the geometry of the system. For the vane used by us the creeping motion regime extended up to a Reynolds number of about 5 as fig. 8.2 shows.

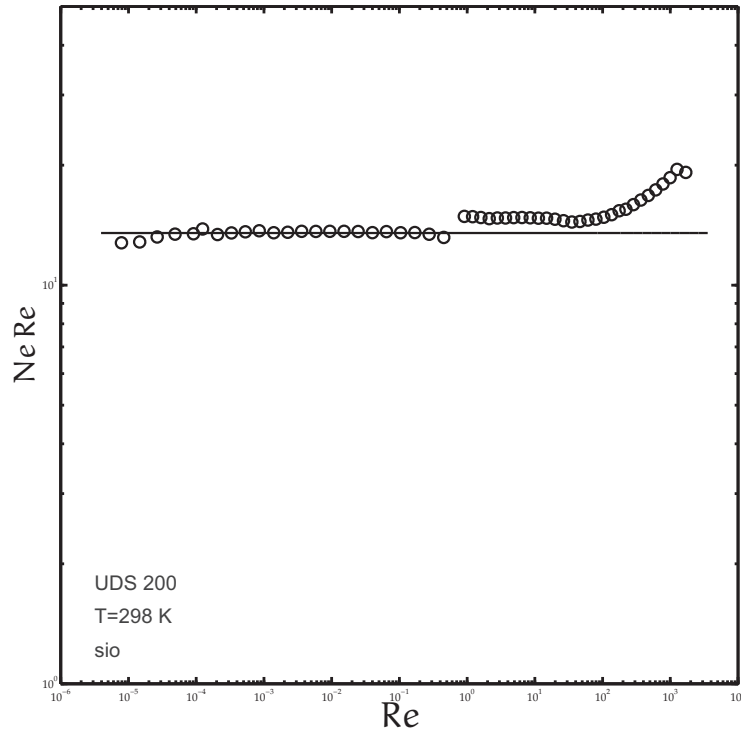


Figure 8.2: Data of fig. 8.1 plotted as $NeRe$ vs Re .

Expressed dimensionally eq. 8.4 reads

$$\eta = C_v \frac{M}{\Omega}, \quad (8.5)$$

where

$$C_v = \frac{1}{cd_v^3}. \quad (8.6)$$

Equation 8.5 is the fundamental equation for the determination of η in all rotational

viscometers. There it is assumed that (an ideal) viscometric flow (VF) prevails, thus allowing an analytic expression for the device constant C_v . For example, for tangential annular flow C_v is given by

$$C_v = \frac{\kappa^2 - 1}{4\pi l_v r_o^2}. \quad (8.7)$$

If the bob–cup dimensions are identical to the vane–cup dimensions used by us (bob radius = r_v) then

$$C_v = 1631.52 \text{ m}^{-3} \quad (8.8)$$

results. The bob–in–cup geometry used by us for the experimental work uses a $C_v = 1527.1 \text{ m}^{-3}$ as given in [3]. For the vane used by us one gets $c = 13.51$ and consequently

$$C_v = 3906.3 \text{ m}^{-3}. \quad (8.9)$$

This differs rather drastically from the theoretical value for tangential annular flow (eq. 8.8). This implies that the intuitive ideal assumption for vane flow, namely solid body rotation up to the vane tips and viscometric flow (VF) from these up to the cup is wrong (as anticipated in [23],[62], [58], [59], [48], [28], [36], [48], [11] and [63]). Despite these differences it is tempting to use the vane as a viscometer. The rationale for such an attempt rests on experimental facts.

For most rotational viscometers the kinematics of VF require fluid inertia to be neglected. Prominent examples are plate–plate (PP) flow and cone–plate flow (CP). Yet, experimentally it is well known that in these devices a three dimensional (3D) flow prevails at all Reynolds numbers ([46], [19]). Global relations like eq. 8.5 are not affected by these facts up to rather moderate Reynolds numbers (e.g [25]). Based on these facts it seems rather natural to anticipate that eq. 8.4 (which implies eq. 8.5) should hold in the CMR for purely viscous fluids and, within limits (to be discussed later), for viscoelastic fluids as well.

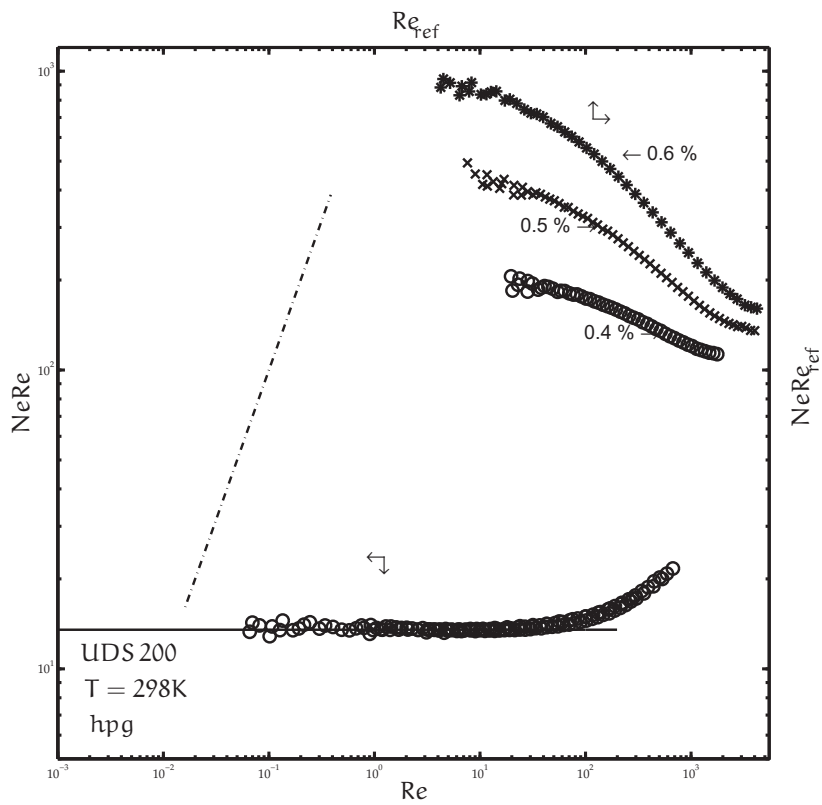
These conjectures are strengthened by the fact that porous medium flow and flow

around an excentrically rotating sphere have both been succesfully used for determining the viscosity of non-Newtonian fluids (e.g. [74], [24]).

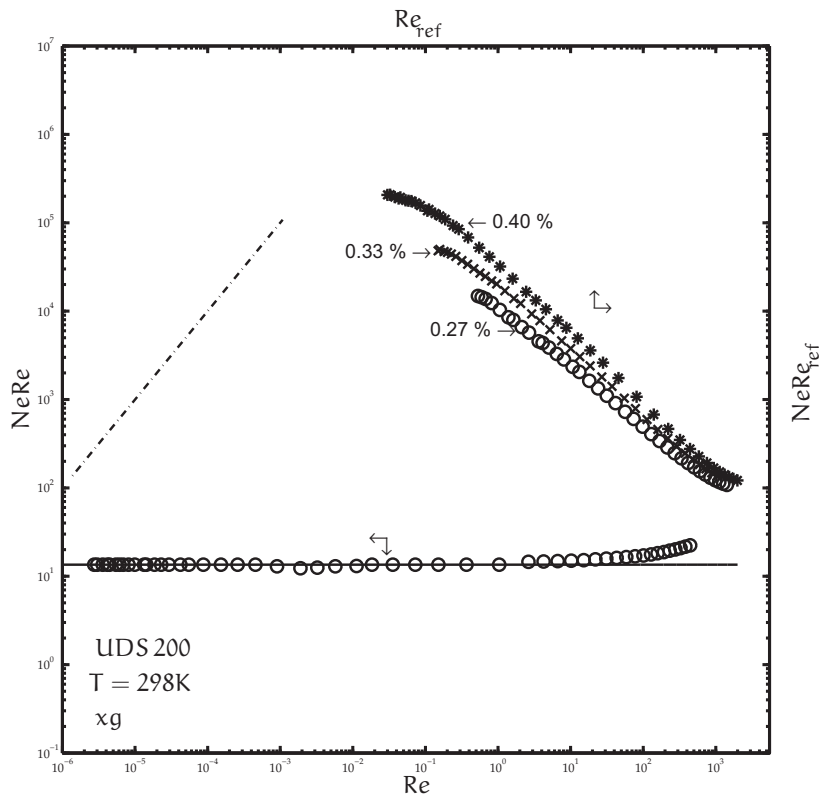
In the CMR measuring the torque of a Newtonian reference fluid (subscript ref) and of another Newtonian or non-Newtonian fluid implies by eq. 8.5 the relation

$$\frac{\eta}{\eta_{\text{ref}}} = \frac{M}{M_{\text{ref}}}\bigg|_{\Omega}, \quad (8.10)$$

provided the measurements are taken at the same angular velocity Ω . Thus, determination of η is readily accomplished. In an $\text{NeRe}_{\text{ref}} = f(\text{Re}_{\text{ref}})$ diagram this implies a shift along a 45 degrees line in order to reach the $\text{NeRe} = c$ curve. Note that $\text{Re}_{\text{ref}} > 5$ may very well imply $\text{Re} < 5$, i.e. data within CMR. Figure 8.3 demonstrates this quite clearly.



(a) Hydroxypropyl guar



(b) Xanthan gum

Figure 8.3: $NeRe$ vs Re and $NeRe_{ref}$ vs Re_{ref} .

For non-Newtonian fluids η is not in general a constant but varies with the shear rate $\dot{\gamma}$ and shear stress τ , respectively. By dimensional reasoning one can assume relations of the kind

$$\begin{aligned}\dot{\gamma} &= c_{\gamma}\Omega, \\ \tau &= c_{\tau}M.\end{aligned}\tag{8.11}$$

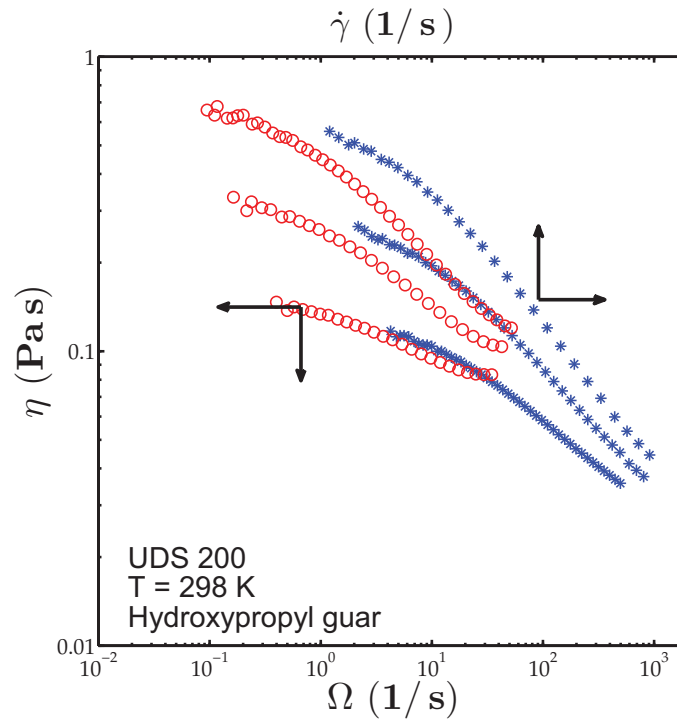
These two constants are not independent but are related by

$$C_v = \frac{c_{\tau}}{c_{\gamma}}.\tag{8.12}$$

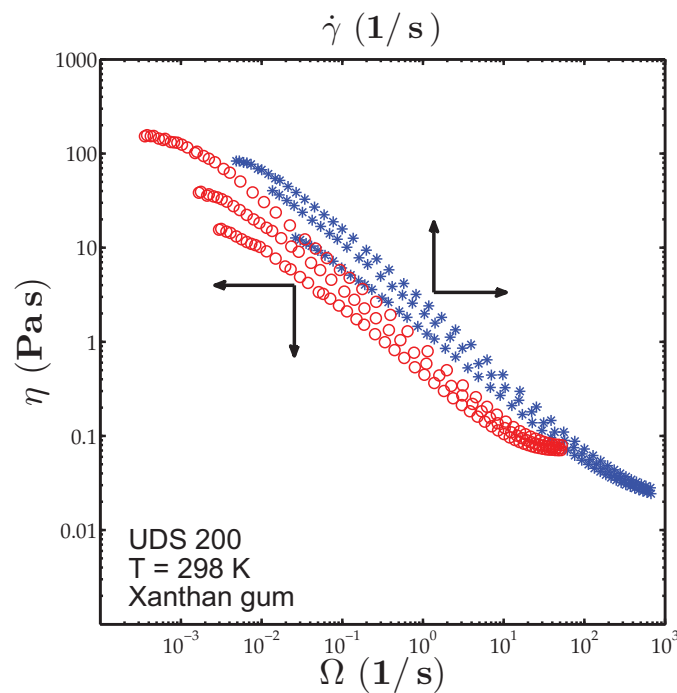
Since C_v is known (eq. 8.9) it thus suffices to concentrate on one of them and we choose c_{γ} .

8.2 Determining the shear rate in vane flow

Pointwise measurements of η in vane flow furnishes $\eta = \eta(\Omega)$, by eq. 8.5. In a viscometer η is determined as $\eta = \eta(\dot{\gamma})$. To determine the flow curve $\eta = \eta(\dot{\gamma})$ in vane flow it requires a shift from the $\eta = \eta(\Omega)$ shear viscosity function (determined from vane flow) to the viscometrically determined flow curve $\eta = \eta(\dot{\gamma})$, see figures 8.4 and 8.5.

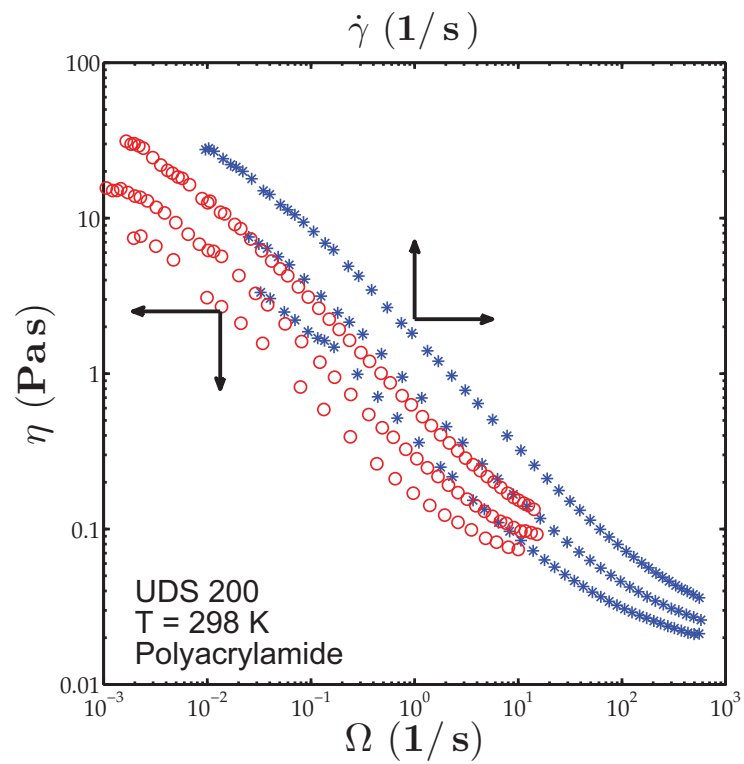


(a) Hydroxypropyl guar



(b) Xanthan gum

Figure 8.4: Viscosity curves. The symbol o corresponds to vane geometry, $\eta = \eta(\Omega)$, and * to bob-in-cup geometry, $\eta = \eta(\dot{\gamma})$.



(a) Polyacrylamide

Figure 8.5: Viscosity curves. The symbol o corresponds to vane geometry, $\eta = \eta(\Omega)$, and * to bob-in-cup geometry, $\eta = \eta(\dot{\gamma})$.

A horizontal shift of the curves at constant η can be mathematically expressed as

$$\eta(c_\gamma \Omega) = \eta(\dot{\gamma}), \quad (8.13)$$

in this way the shift factor c_γ , as defined in eq. 8.11 can be evaluated. Plotting for the same η as a function of Ω the slope of this graph will furnish c_γ . Figure 8.6 shows this further.

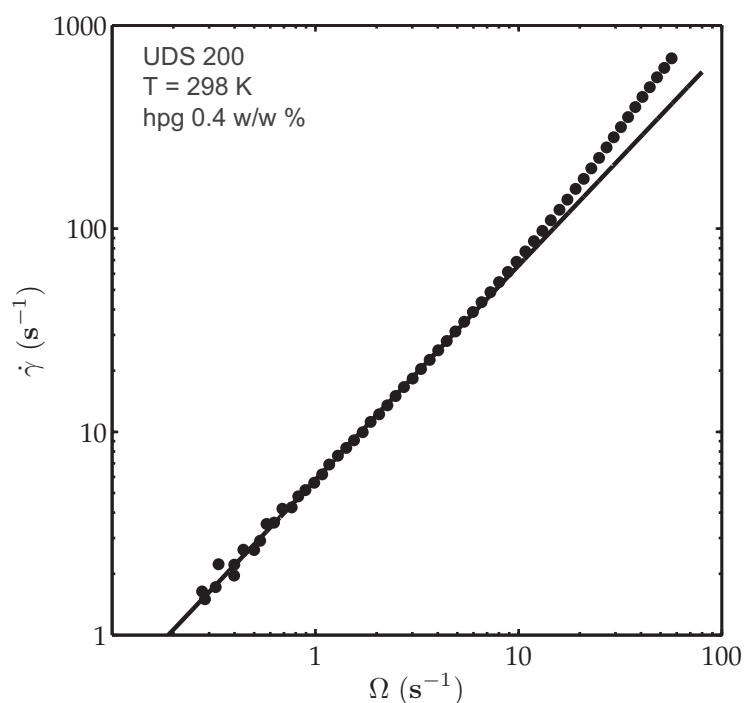


Figure 8.6: Shear rate vs angular velocity (bob and vane geometries).

It can be seen that for small Ω the shear rate is a linear function of Ω , i.e. c_γ is a constant. Table 8.1 lists this constant c_γ .

Fluid	Concentration [c] (w/w%)	c_γ (s/s)
Hydroxypropyl guar	0.40	1.6804
	0.50	3.0734
	0.60	3.5957
	Averaged c_γ	3.3346
Xanthan gum	0.27	4.4474
	0.33	4.4455
	0.40	4.0000
	Averaged c_γ	4.2976
Polyacrylamide	0.05	3.8418
	0.10	4.7382
	0.20	4.4504
	Averaged c_γ	4.3435

Table 8.1: Device constants for the vane geometry.

Using for each type of solution used by us one c_γ value, a comparison between viscometrically determined flow curves and flow curves determined from vane flow is shown in figures 8.7 and 8.8.

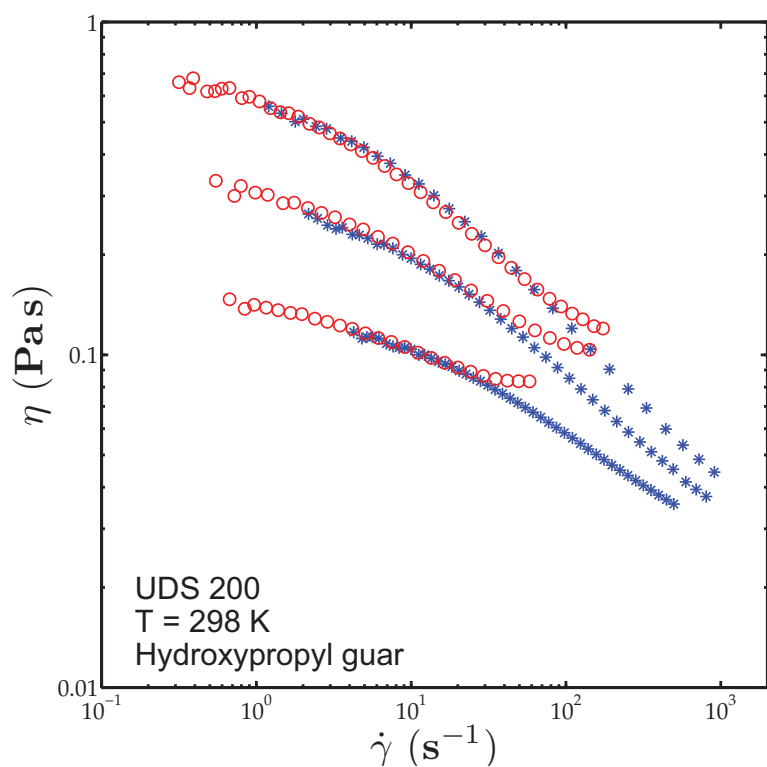
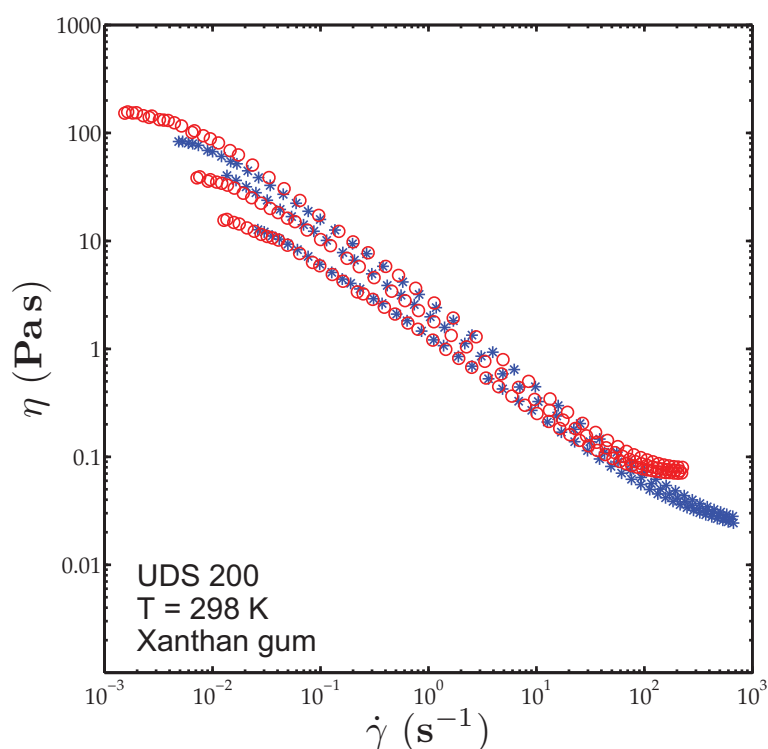
(a) Hydroxypropyl guar ($c_\gamma = 3.3346$)(b) Xanthan gum ($c_\gamma = 4.2976$)

Figure 8.7: Viscosity curves. The symbol o corresponds to the vane geometry, and * to the bob-in-cup geometry. Calculations were made with c_γ from table 8.1.

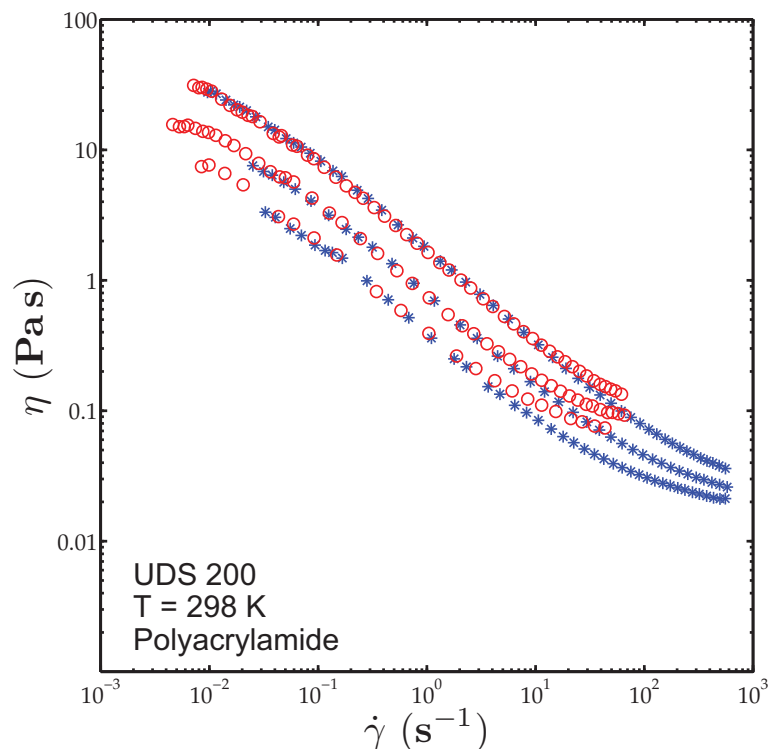
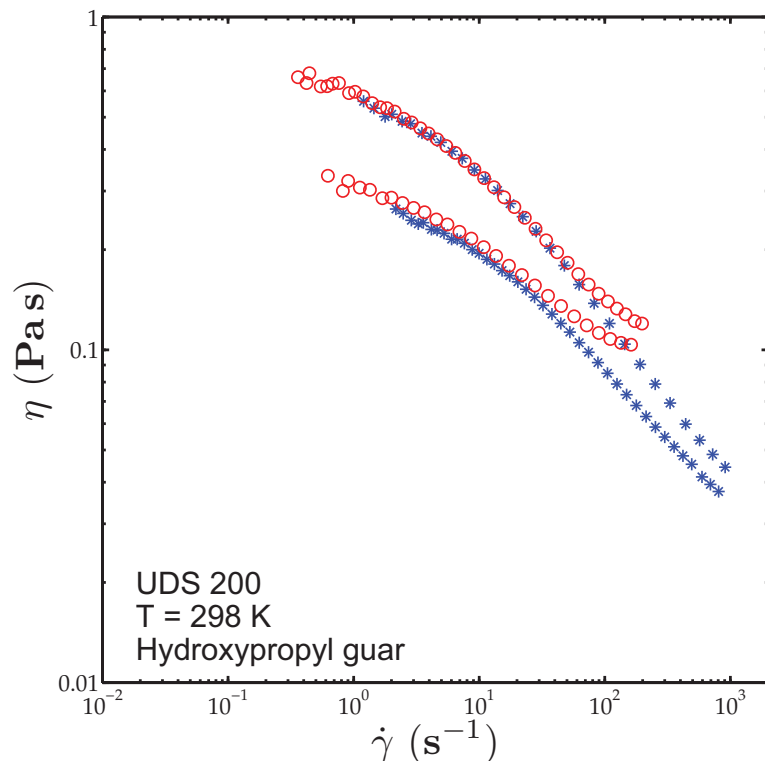
(a) Polyacrylamide ($c_\gamma = 3.9519$)

Figure 8.8: Viscosity curves. The symbol o corresponds to the vane geometry, and * to the bob-in-cup geometry. Calculations were made with c_γ from table 8.1.

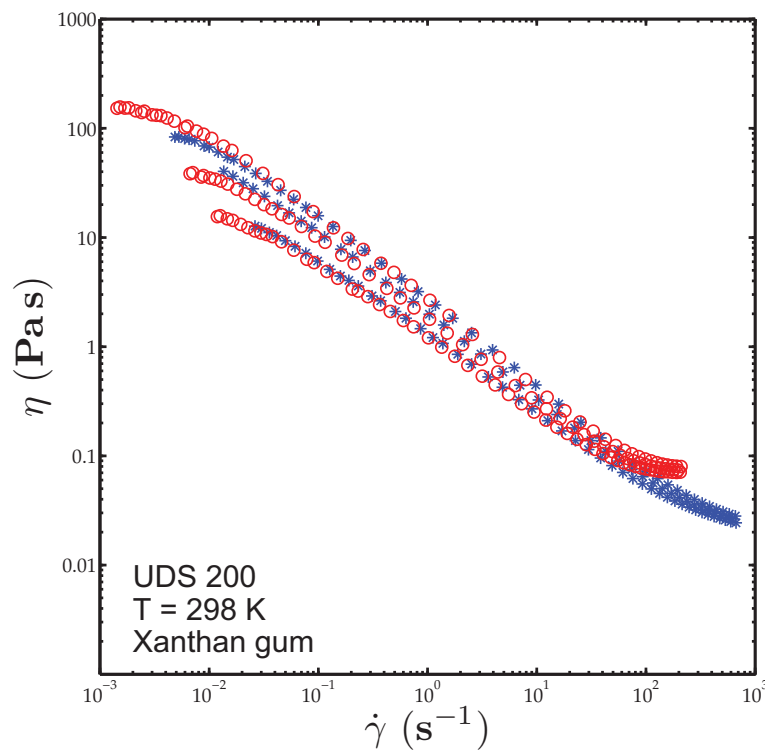
It can be clearly seen that the vane correctly predicts the viscosity function, especially for sufficiently small shear rates. Deviations at higher shear rates cannot be disputed, however. This is the case whenever c_γ is not a constant but depends on Ω , i.e. $c_\gamma = c_\gamma(\Omega)$ (non-linear regime of fig. 8.6). The reason for this is easy to comprehend. All fluids studied are known to be viscoelastic.

Elasticity of a fluid leads to local changes in the flow field from the purely viscous ones. Being non-linear these changes become more and more pronounced the higher the shear rate is. Deviations of relations between global quantities are the consequence. Only as long as the effect of elasticity can be neglected in global relations between M and Ω can vane experiments be used to determine η . Outside this range they cannot.

In order to use the vane for viscoelastic fluids as a viscometer within this, limited, range of validity, it requires a fluid independent constant c_γ . The data of table 8.1 reveal that an arithmetically averaged c_γ of all our measurements is close to 4. Using this value for c_γ produces satisfactory results for the vane viscosity function as figs. 8.9 and 8.10 show.



(a) Hydroxypropyl guar



(b) Xanthan gum

Figure 8.9: Viscosity curves. The symbol o corresponds to vane-in-cup geometry, and * to bob-in-cup geometry. Calculations were made with the averaged $c_\gamma = 4.0$.

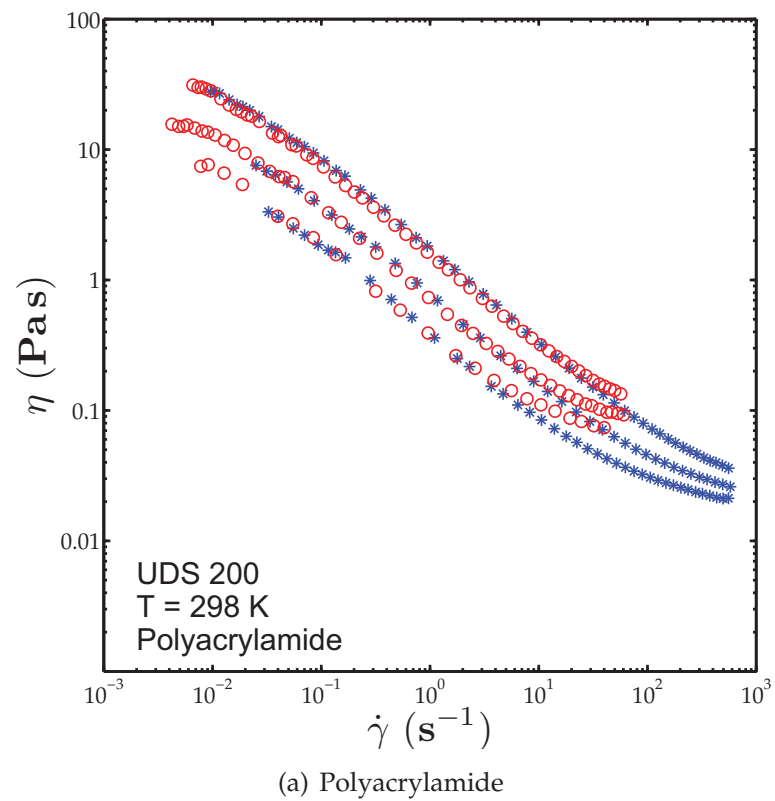


Figure 8.10: Viscosity curves. The symbol o corresponds to vane-in-cup geometry, and * to the bob-in-cup geometry. Calculations were made with the averaged $c_\gamma = 4.0$.

This reveals that the vane can indeed be used as a viscometer for viscoelastic fluids. It thus supplements –on an analogous basis– the porous medium flow viscometer ([75], [44], [42], [57], [50]) and the viscometer based on the principle of a sphere rotating around an axis eccentric from the sphere ([52]). This latter viscometer seems to be the proper choice for highly filled suspensions (e.g. cement slurries) where viscometric flow can lead to internal fracture of the fluid and thus to disastrous results ([74]). The vane, on the other hand, seems applicable for ‘ordinary’ viscoelastic fluids like polymer solutions.

9 PIV measurements

In the present chapter we show the results of the PIV-measurements carried out for vane flow. Before going into details and discussing the results, here is a short description of both the set-up and the procedure from the experimental part.

In section 6.2.4 we have shown the equipment set-up used for the visualization. There, the rheometer UDS 200 was modified allowing the measurements to be taken. First, the metallic cup was replaced with one made of polymeric glass, whose refractive index matches that of the fluid. We were interested in the flow between the blades of the vane at a plane perpendicular to the axis of rotation which is located at the middle of the vertical face of the vane (see fig. 6.9). For that situation all lateral faces were painted to black except one (where the laser beam illuminates the flow) in order to reduce interferences due to reflection of the light (see fig. 9.1).

The light source was coupled with the computer so that the triggering (shooting of the pictures) could be automated and set-up according to the flow conditions. The light source was a pulsed laser with a wavelength of 532 nm produced by the company Meillot. All pictures were taken with a HighSense camera model 80C60 CCD and a macro-objective Nikon of 60 mm of focal length. The laser device was connected to the digital interface in the PIV-hardware.

PIV measurements were performed with a transparent Newtonian fluid (silicon oil) at moderately low angular velocities. Since the PIV device was borrowed from another research group at Lehrstuhl für Strömungsmechanik Erlangen, a tight time span was granted during which we could use the device. Thus, it was not possible to use non-Newtonian fluids.

9.1 Flow between the blades

Our main interest in the experimental part with the PIV-technique was the visualization of the flow in the region between the blades of the vane. For that we selected as tracer-particles silicon-coated glass-spheres with a diameter $\approx 10 \mu\text{m}$. To prepare the fluid for the measurements the tracer was added slowly to the silicon oil and stirred as the tracers were poured to avoid conglomerates.

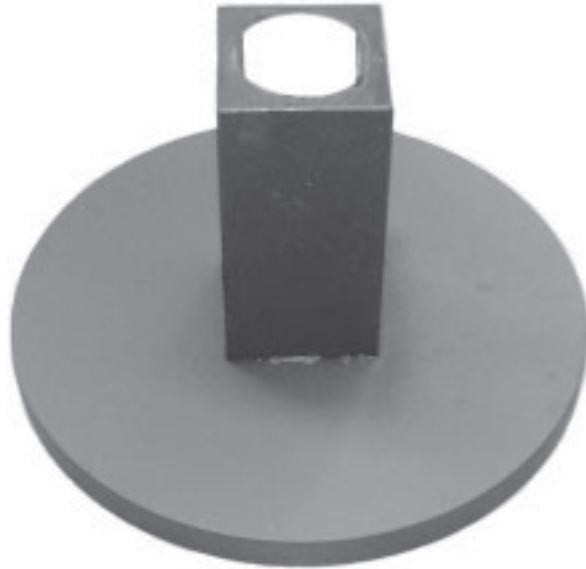


Figure 9.1: Cup of glass used for the PIV measurements.

The velocity vectors did not show a cylindrical shape in the whole domain as fig. 9.2 (for an angular velocity $\Omega = 0.064$ 1/s) shows. The assumption of a purely azimuthal velocity field is wrong.

In the same fig. 9.2 for the same angular velocity it can be seen that deviations from the cylindrical shape are accentuated in the region between the blades (approximately in the region toward the outer cup from the middle of the vane up to the tips). Near the corners of the vane, the velocity tends to have a circular shape. This region is indeed small and not comparable to the remaining part of the flow domain.

In the experimental part it was not always straightforward to obtain a signal free of interferences (caused by the surface of glass which increases the number of outliers). Furthermore, the regions near the outer cup and the gap between the vane edge and the outer cup could not be resolved. These regions are very small. The objective and the chip of the CCD camera did not allow to obtain acceptable measurements at these locations.

The parts where the flow could be visualized with less interferences are located within the blades of the vane. We extracted from selected regions the velocity.

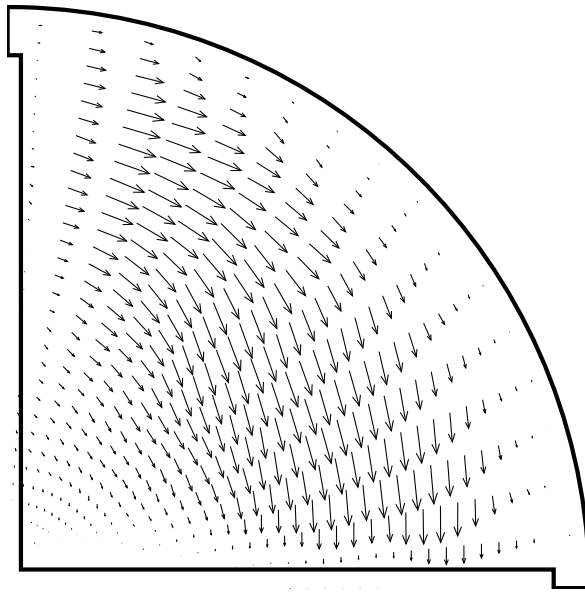


Figure 9.2: PIV measurement at $\Omega = 0.064 \text{ s}^{-1}$, Newtonian fluid sio80.

The results of the PIV measurements give an instantaneous view of the flow field. Despite this, if accurate (quantitative) measurements are sought, specially near the solid boundaries another technique should be employed. In the next section we will define the coordinate system we need for the velocity profiles from the PIV measurements.

9.2 Transformation of coordinates

In previous section we have seen how the total velocity deviated from the usually assumed circular shape. In this section we show the profiles of the total velocity along selected regions of the vane-in-cup domain. It is interesting to see the be-

havior of the flow between the blades of the vane, from the common point where they unite, up to the outer cup. For the visualization we select three segments along different radial locations.

Boundary conditions have been imposed accordingly at the corresponding locations. A spatially fixed global coordinate-system whose origin is located at the axis of rotation of the vane was used for the numerical simulations. To show the flow field between the vanes another coordinate system is fixed within the global coordinate-system (the one that was used to perform the numerical simulations (fig. 4.4)). In this way the solid regions are separated from the fluid. Since this new coordinate system will have its origin at the intersection point of the vanes (corner) we define this coordinate system in terms of the global one.

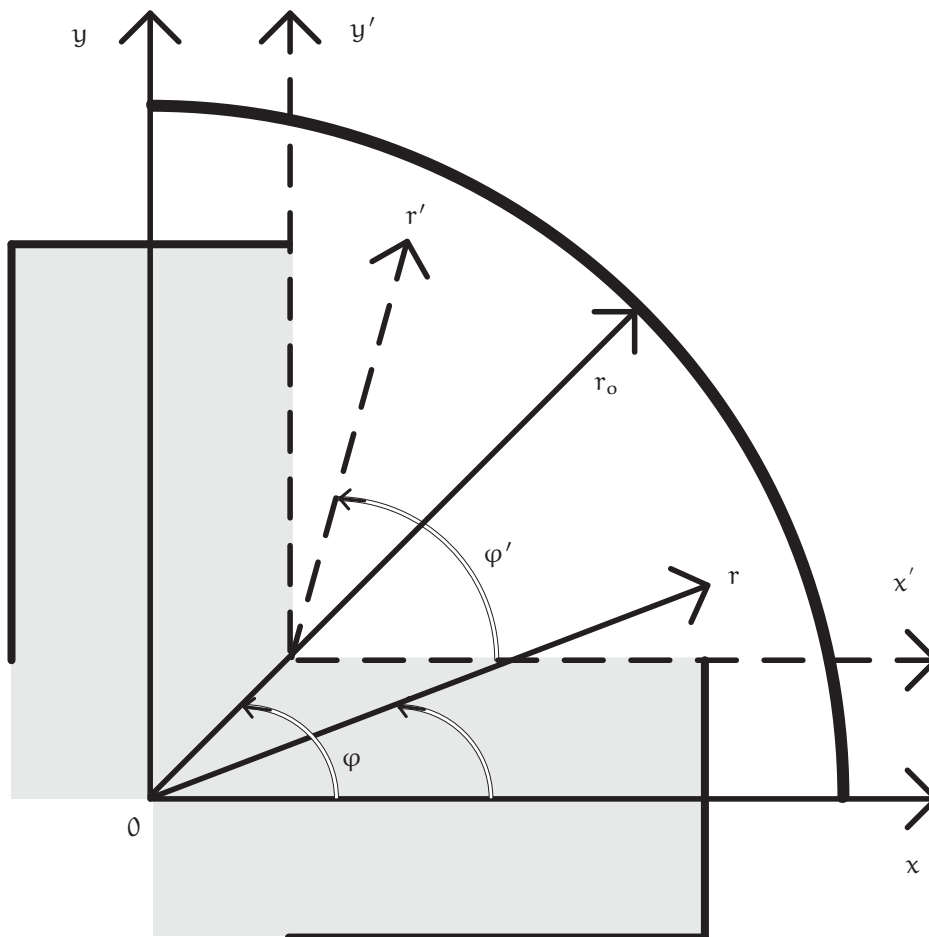


Figure 9.3: Sketch of the global and the local coordinate-systems.

In fig.9.3 the local-coordinate system and the global-coordinate system are shown. The global-coordinate system (axis x and y) is notated with solid lines whereas the local-system with dashed lines (axis x' and y').

Both coordinate systems can be related with the following transformations.

$$r = \sqrt{x^2 + y^2} \quad (9.1)$$

$$r' = \sqrt{x'^2 + y'^2}. \quad (9.2)$$

The global coordinate-system can be written in terms of the local coordinates as

$$x = x' + x_{00} = r \cos \varphi \quad (9.3)$$

$$y = y' + y_{00} = r \sin \varphi \quad (9.4)$$

with

$$x' = r' \cos \varphi' \quad (9.5)$$

$$y' = r' \sin \varphi'. \quad (9.6)$$

In this relationship the point $x_{00} = y_{00}$ (here 0.5 mm) corresponds to the intersection point of adjacent vanes (half the thickness of the blade of the vane). That is to say the origin of the local coordinate system.

The radius r' in the local coordinate-system in terms of the global is given by

$$r' = \sqrt{(x - x_{00})^2 + (y - y_{00})^2}. \quad (9.7)$$

In both systems the angles φ and φ' can be related through the radius r , then

$$\varphi = \tan^{-1} \frac{y}{x} = \tan^{-1} \frac{r' \sin \varphi' + y_{00}}{r' \cos \varphi' + x_{00}}. \quad (9.8)$$

Finally, by replacing equations 9.3 and 9.4 into 9.1 and solving for r' ($r = r_o, \varphi'$) we get

$$r'(\varphi') = \sqrt{r_o^2 - x_{00}^2(1 - 2 \cos \varphi' \sin \varphi')} - x_{00}(\cos \varphi' + \sin \varphi'). \quad (9.9)$$

In equation 9.9 $r'(\varphi')$ is the maximum value r' reaches as a function of the angle φ' in the local coordinate system since $r = r_o$ is constant. The maximum value $r'(\varphi')$ reaches in the local coordinate system occurs when $(\cos \varphi' + \sin \varphi') = 1$ (and consequently the product $\cos \varphi' \sin \varphi' = 0$). This occurs at $\varphi' = 0$ and $\varphi' = 90^\circ$.

The transformations given by equations 9.8 and 9.9 allow us to extract and visualize the flow information along the desired regions in the local system in terms of the global one.

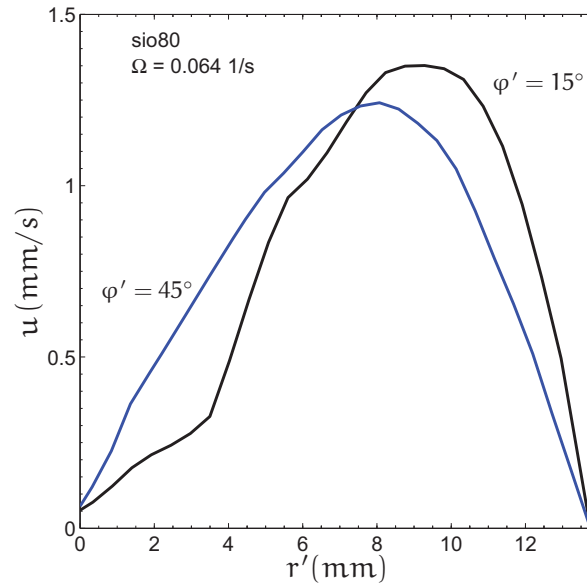
We perform our simulations in a quarter of the vane therefore $0 \leq \varphi \leq 90$. The angle φ' can be calculated analogously to eq. 9.8 and restricted to one quarter of the domain where the vane rotates.

The angle φ' as measured from the edge of the vane is taken as 15, 45 and 75 degrees, that is, a line that is half way apart between the vanes ($\varphi' = 45^\circ$) and two additional lines, each near the vane tips ($\varphi' = 15^\circ, 75^\circ$). The visualization of the results is shown in the range $0 \leq r' \leq r'(\varphi')$.

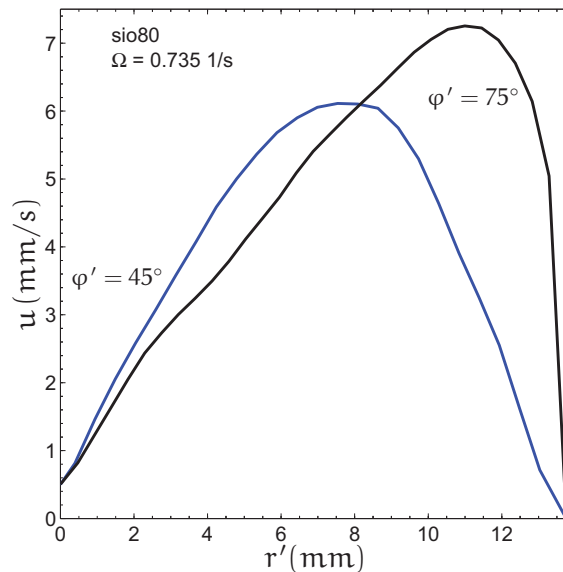
9.3 Velocity profiles

Experiments for vane flow were carried out at low angular velocities. For this purpose a transparent Newtonian fluid with viscosity of 80 mPa s was used. We were particularly interested in the region between the blades. The region selected for the experiments was perpendicular to the axis of rotation, located midway from the top and bottom of the vane. The digital information collected from the measurements was pre and post-processed with a commercial software marketed as Flowmap version 3.60, produced by the company DANTEC GmbH. In the post-processing an interrogation area of 64×64 pixels and cross-correlation for the calculation of the velocity was used with 50 % of overlapping.

In fig. 9.4(a) we can see the velocity profile of the NF at different locations. There the total velocity rises from a small value toward the cup and reaches at a radial location which is smaller than the radius r_v of the vane its maximum value. From this location, up to the outer cup the total velocity starts to decrease.



(a) Velocity profiles at $\varphi' = 15^\circ$ and 45° .



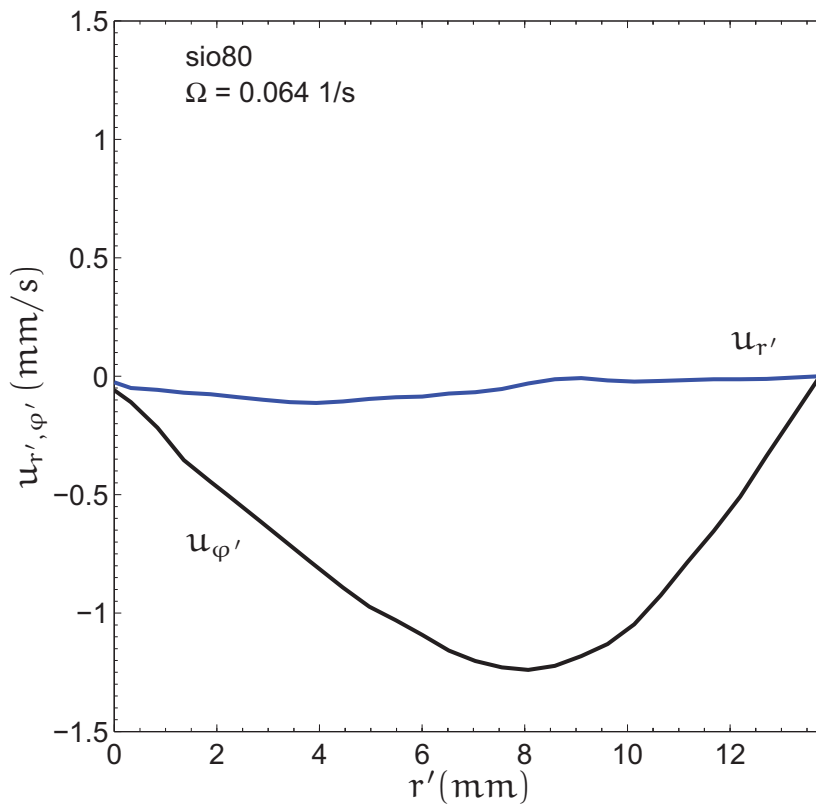
(b) Velocity profiles at $\varphi' = 45^\circ$ and 75° .

Figure 9.4: Total velocity profiles along selected regions, NF at $\Omega = 0.064 \text{ s}^{-1}$ and 0.735 s^{-1} .

The qualitative behavior of the shape of the velocity profile is similar at the different φ' selected, however, in these cases the maximum of the velocity occurs at different radial locations. This suggests that the velocity is not constant for an arbitrary φ' . A circular pattern in which the velocity is constant is not possible with the behavior that is observed in figs. 9.4(a) and 9.4(b). In fig. 9.4(b) the angular velocity is higher than in fig. 9.4(a), despite this, we can observe that the qualitative behavior is still similar for both cases.

The explanation of the behavior of each of the velocity profiles can be complemented with their respective velocity components $u_{\varphi'}$ and $u_{r'}$. Figures 9.5–9.6 summarize this.

One can see in figs. 9.5(a)–9.6(b) that in all cases the velocity component $u_{\varphi'}$ dominates over the component $u_{r'}$.



(a) $\varphi' = 45^\circ$.

Figure 9.5: Components of the velocity profile along different sections in the vane geometry. Newtonian fluid at $\Omega = 0.064 \text{ s}^{-1}$ and 0.735 s^{-1} .

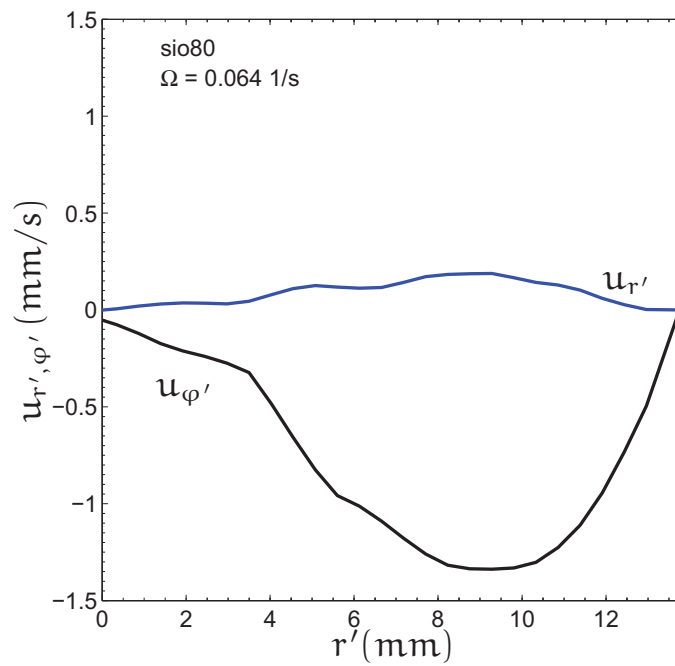
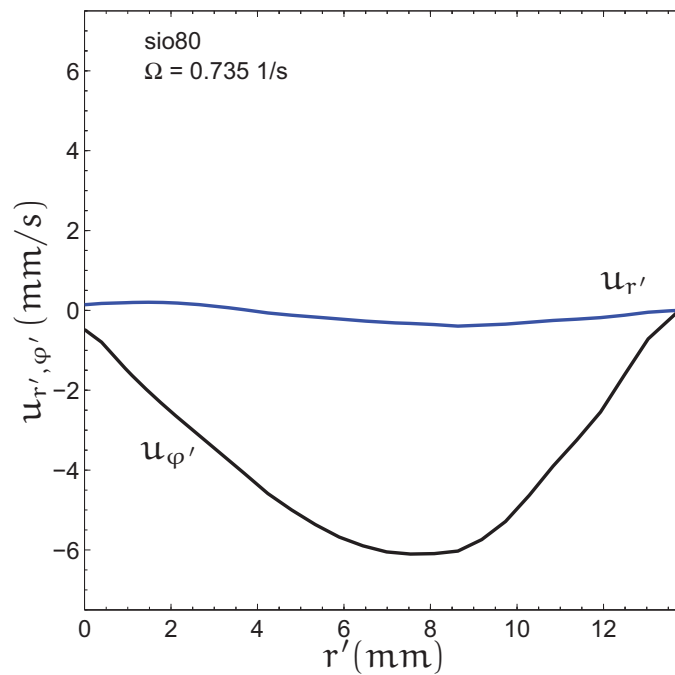
(a) $\varphi' = 15^\circ$.(b) $\varphi' = 45^\circ$.

Figure 9.6: Components of the velocity profile along different sections in the vane geometry. Newtonian fluid at $\Omega = 0.064$ s⁻¹ and 0.735 s⁻¹.

10 Numerical simulations for vane flow

In the following chapter we are going to present and discuss the results of the numerical simulations performed for vane flow. The purpose of these simulations is to gain an insight into the flow structure in the vane flow while using different fluids in the creeping motion regime (CMR) –see chapter 3 section 3.3.

In chapter 8 we showed through experiments that the assumption of a solid–body rotation is not appropriate for calculating the viscosity of a fluid, since no viscometric flow occurs and consequently the device constants differ, for example, from that used for a concentric cylinder where a viscometric flow can theoretically take place. Our method to evaluate the viscosity and the shear rate is applicable in the CMR without such an assumption for any of the fluids used. In the literature most of the work devoted to investigate the vane flow assume a solid–body rotation (see chapter 2).

We have formulated the problem for the simulations in chapter 3. This formulation consisted of an overview of the numerical method used by the simulation package, the boundary conditions imposed and the mesh of the geometry. Since we scaled the general transport equation we were able to formulate a quasi–steady simulation ($Re \rightarrow 0$). Numerical simulations with high spatial resolution (very fine mesh), require a high amount of computer memory and take a long time until they converge to a solution. Therefore, to save computer memory and computation time only a quarter of the whole two–dimensional vane–in–cup domain was used. All simulations were carried out using a personal computer equipped with 1 GB of physical memory and an Intel Pentium processor of 1.8 Hz frequency.

The fluids employed for the simulations were NF and GNF, where the model parameters were determined from rheological measurements. The simulations were initially performed with a bob–in–cup geometry for validation purposes.

The numerical simulations were performed at relatively small angular velocities in order to approximate the creeping motion regime. The model fluids used were a NF, the Cross model and the Carreau–Yasuda model.

The effective viscosity of each GNF is, respectively:

$$\eta_{\text{eff}} = \eta_{\infty} + \frac{\eta_0 - \eta_{\infty}}{1 + (\lambda C_{\gamma} \Omega)^{\alpha}}, \quad (10.1)$$

and

$$\eta_{\text{eff}} = \eta_{\infty} + \frac{\eta_0 - \eta_{\infty}}{[1 + (\lambda C_{\gamma} \Omega)^{\beta}]^{\frac{1-n}{\beta}}}. \quad (10.2)$$

Some additional information concerning the numerical results can be found in the Appendix.

10.1 Flow field

The fluid within the blades of the vane is often assumed to move together with the vane as a solid body. This implies that the velocity will be constant at a given constant radius r' for any φ' .

In our work, the rheological models of the GNF used for the simulations consider Newtonian plateau and power-law regions with a relatively strong shear-thinning behavior in the range of shear-rates used in the experimental part.

Figures 10.1 and 10.2 show the stream and contour lines for the NF and the GNF at an angular velocity $\Omega = 0.01$ 1/s (clockwise rotation, unless otherwise stated).

For either the NF or the GNF, in these figures there is no evidence of a solid-body rotation. The stream lines show that a weak cylindrical shape occurs near the corner of the vanes. Toward the outer cup the streamlines take a flatter shape and clearly the velocity is not constant for a given constant radius r' at any φ' .

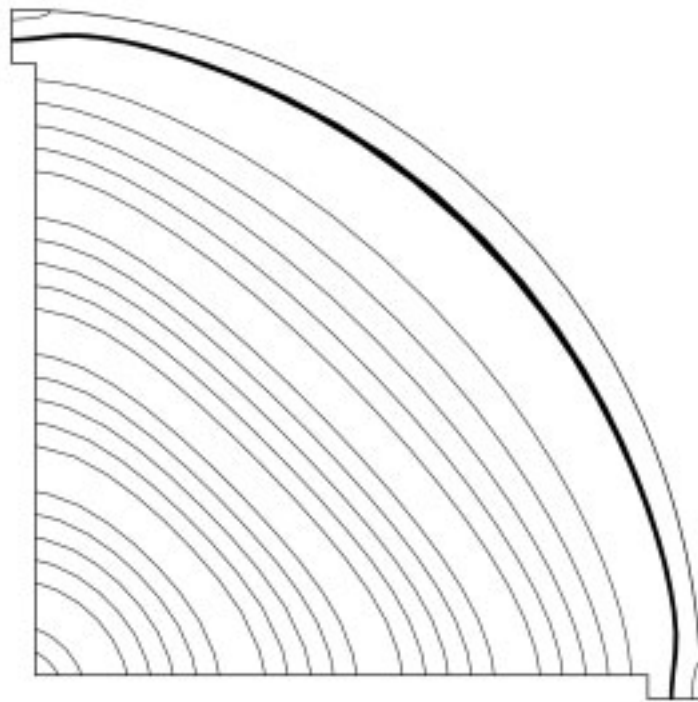
The qualitative behavior is similar for both type of fluids implying that the flow situations are not merely due to the type of material.

The fact that the velocity distribution does not represent a circumscribed solid-cylinder within the blades of the vane suggests that the shear rate may not be a constant in the φ' direction. A cylindrical shearing-zone (Keentok et al. [48]) is unlikely to exist. The cylinder analogy as used for concentric rotational-viscometers

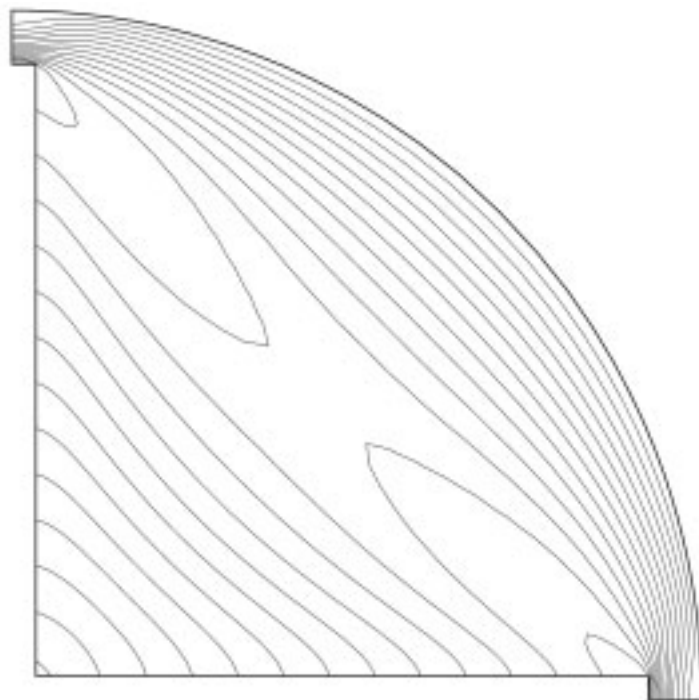
does not apply for vane flow because there is no uniform velocity distribution, as required for a bob-in-cup system.

Concerning the flow structure, our results differ, for example, from those obtained by Keentok et. al [48] and Barnes et al. [11] (results of Barnes et al. are shown in the appendix in fig. E.1). Keentok et al. found a discrepancy between theory and experiment that he could not explain. The so-called 'shearing-region' (imaginary circular region around the tips of the vane whose radius is slightly greater than the radius of the vane) was found to increase linearly with increasing ratio of yield stress to viscosity while their simulations showed a different behavior, i.e., an exponential decrease.

The results of the simulations by Barnes et al. with their finite element code show circular streamlines for the non-Newtonian fluid and slightly flatted streamlines for the Newtonian case. In our simulations the results are similar for both type of fluids and there is no evidence that somewhere between the vanes such a circular pattern develops for any angular velocity or type of fluid. Recall that our generalized Newtonian models also account for the power law region.

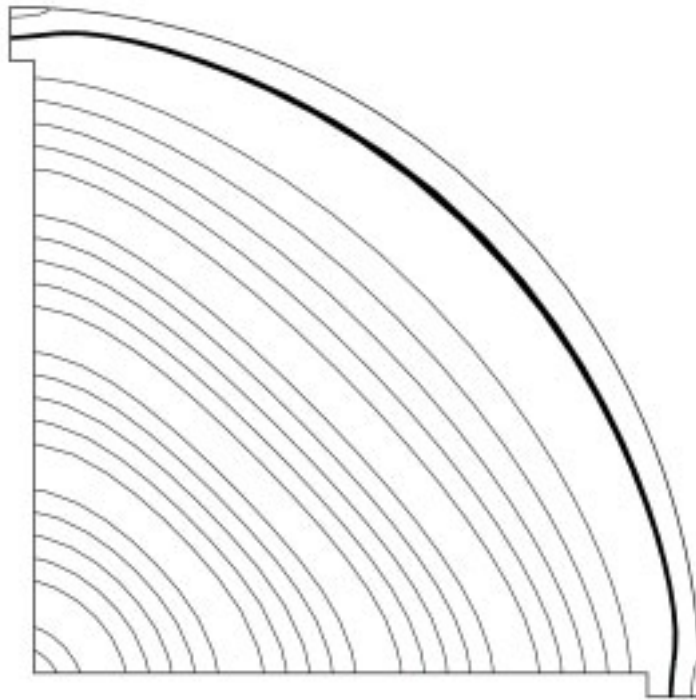


(a) Streamlines.

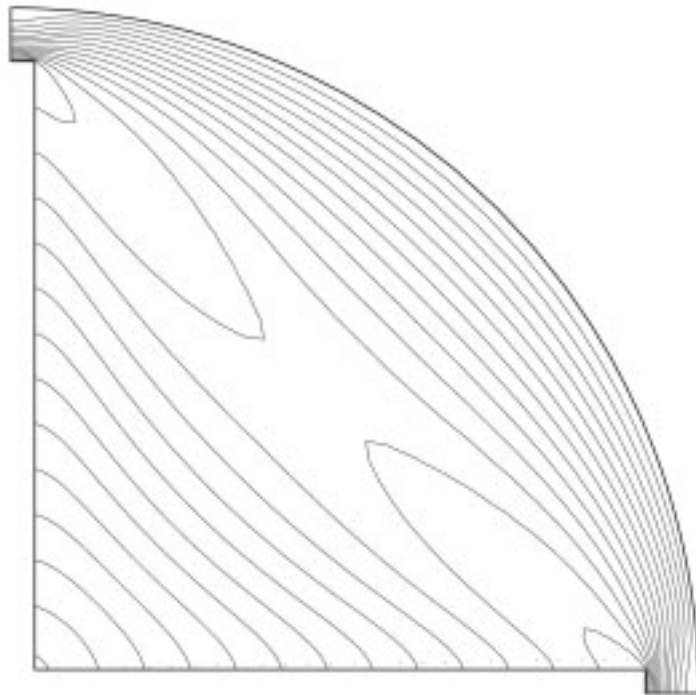


(b) Contour lines.

Figure 10.1: Stream and contour lines for the NF sio500. Angular velocity $\Omega = 0.01s^{-1}$, \circ .



(a) Streamlines.



(b) Contour lines.

Figure 10.2: Stream and contour lines for the GNF hpg 0.6 w/w %. Angular velocity $\Omega = 0.01\text{s}^{-1}$, \circ .

10.2 Profiles of the velocity within the blades

Stream and contour lines have shown a non-uniform velocity distribution in the φ' direction. The radial distributions of the total velocity and its components for different φ' 's are shown in figs. 10.3–10.6. The angles selected for the profiles are $\varphi' = 3^\circ, 15^\circ, 45^\circ, 75^\circ$ and 87° (See section 9.2 for the transformation of coordinates and fig. 9.3).

Figures 10.3 and 10.4 show increasing profiles of the total velocity toward the outer cup for both, the NF and the GNF. In these profiles the total velocity reaches a maximum and starts to decrease until it gets its minimum at the outer cup. The radius r' where the velocity reaches its maximum ($\varphi' = \text{cte.}$) in each case is summarized in table 10.1.

φ'	r' (mm) (NF)	r' (mm) (GNF)
3°	12.28	12.27
15°	9.93	9.93
45°	8.06	8.06
75°	9.93	9.93
87°	12.31	12.31

Table 10.1: Radial locations for the occurrence of the maximum velocity at given angles φ' (data from figs. 10.3–10.6).

The numerical simulations are in agreement with PIV measurements. Figures 9.4(a) and 9.4(b) show the same pattern of the total velocity profile as in the numerical simulations. One can see in figs. 10.3 and 10.4 that the values of r' where the velocity reaches its maximum are smaller than the radius of the vane r_v . A condition for a solid-body rotation is that the maximum of the velocity occurs always at the same radial position being this at a radius equal to the radius r_v of the vane.

The components of the total velocity plotted in figs. 10.3 and 10.4 show that the contribution of each of them is different in magnitude and shape for each φ' , being $u_{\varphi'}$ always dominant.

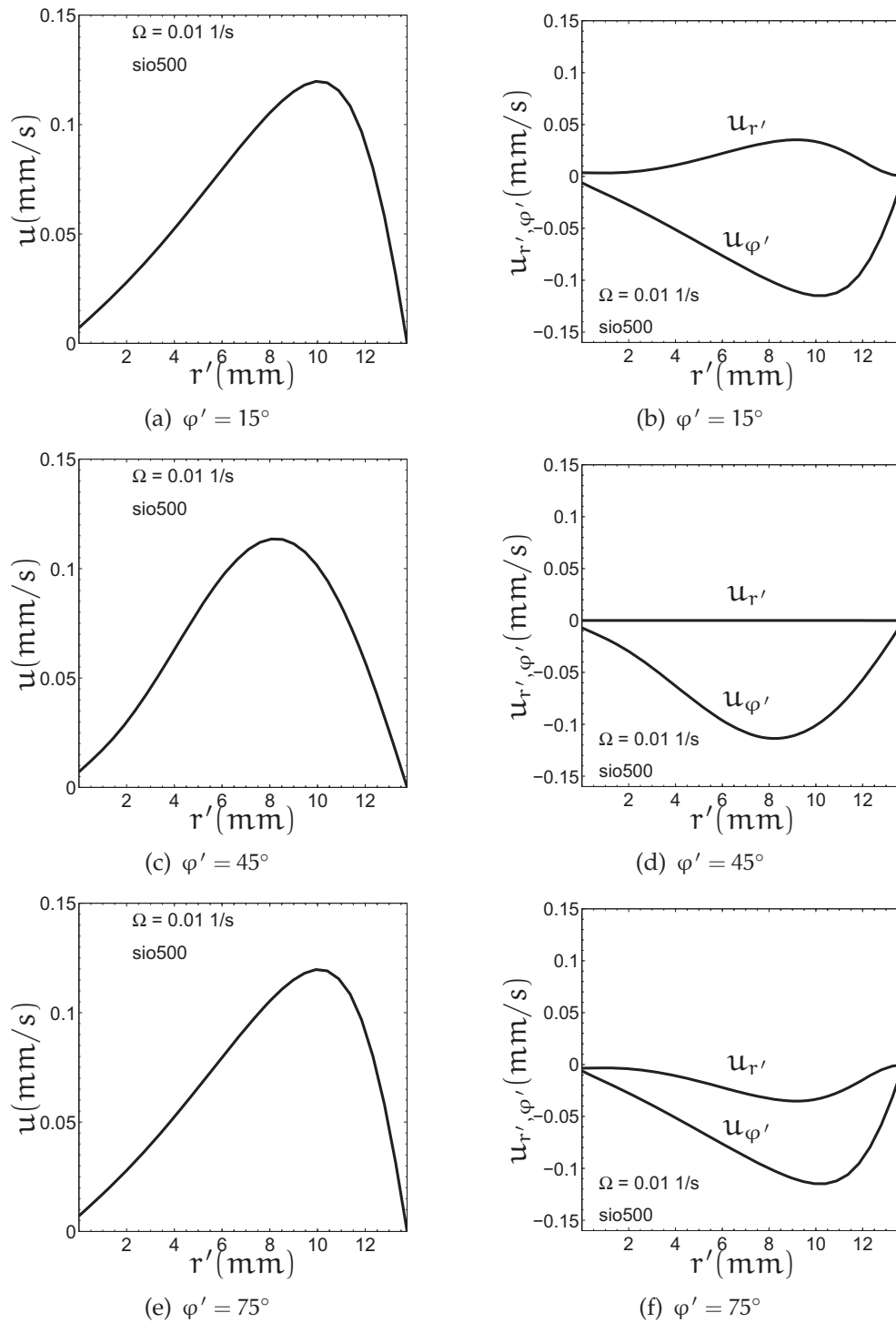


Figure 10.3: Profiles of the total velocity and its components at different angles and radial locations for the NF. Angular velocity $\Omega = 0.01 \text{ s}^{-1}$, \circ .

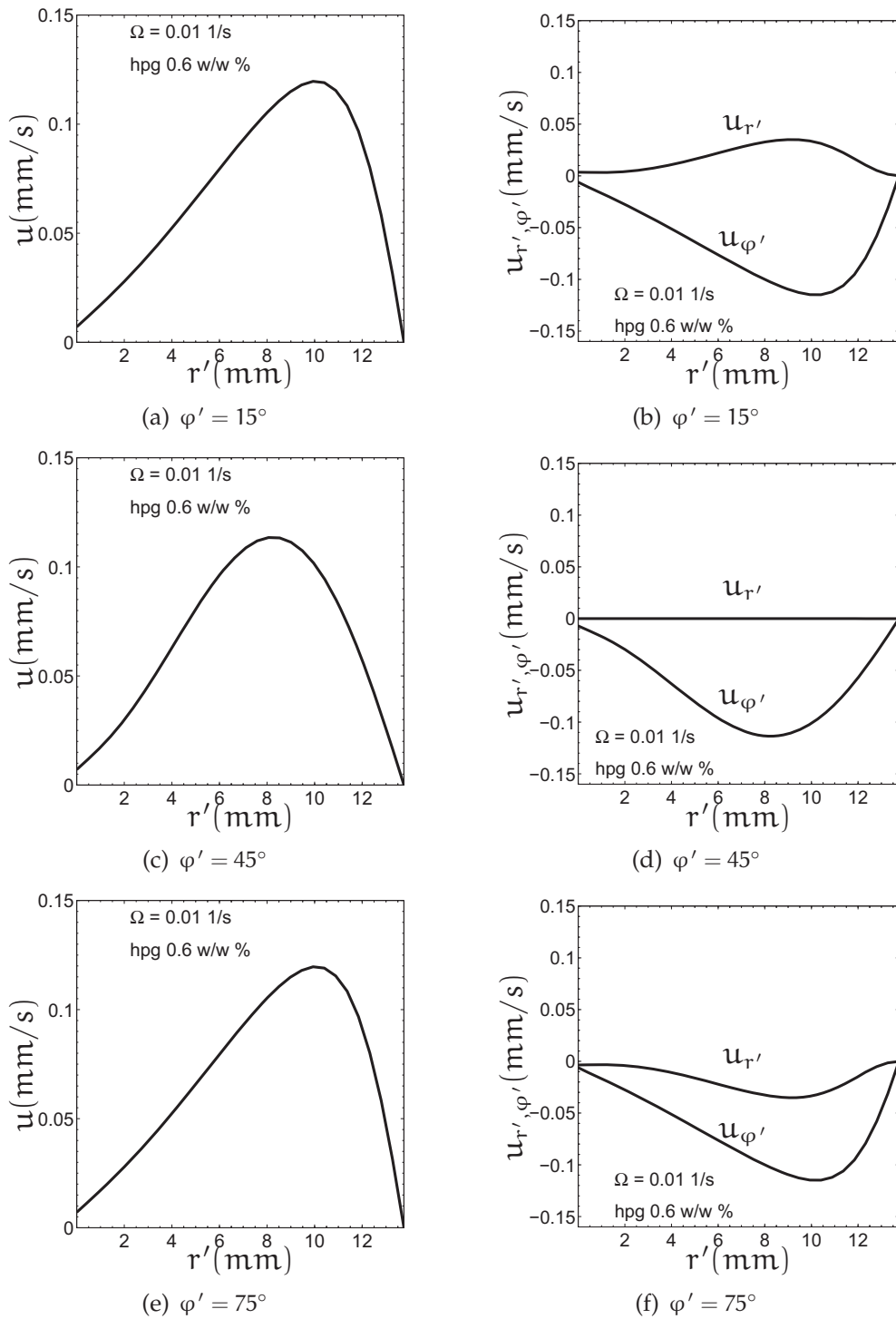


Figure 10.4: Profiles of the total velocity and its components at different angles and radial locations for the GNF. Angular velocity $\Omega = 0.01\text{s}^{-1}$, \odot .

10.3 Profiles of the velocities near the vane

Something that could not be resolved in PIV measurements were the velocity profiles near the solid boundaries, e.g. in the radial direction near the rotating vane at a small φ' . Figures 10.5 and 10.6 show that near the tips of the vane (at $\varphi' = 3^\circ, 87^\circ$) the total velocity increases linearly and gets its maximum at a radius r' greater than the radius r' ($\varphi' = 15^\circ, 45^\circ, 75^\circ$) but still smaller than the radius of the vane (figs. 10.5 and 10.6).

In figs. 10.5(b), 10.5(d), 10.6(b) and 10.6(d) two peaks can be seen in the profile of $u_{r'}$. There, $u_{\varphi'}$ dominates over $u_{r'}$ similarly as at the other φ' 's. The component $u_{r'}$ changes its direction near the tips of the vane. The same happens at $\varphi' = 87^\circ$ which is also near the tips of the vane. Keentok et al. [48] and Farias et al. [33] presume that secondary motions can appear behind the vanes. This is not in agreement with the results of Keentok et al. who claim that a cylindrical shearing-surface appears circumscribed in the vane as it rotates with a radius slightly greater than the radius of the vane.

Atkinson et al. [5] showed mathematically that near the vanes a singularity can occur. This certainly complicates the interpretation of the vane-flow in terms of the total velocity (or its components). Stream and contour lines have shown for both, the NF and the GNF, that the type of flow occurring in the vane cannot be strictly a function of the type of fluid even at low motions. In the experiments carried out in chapter 8 we have shown that as we depart from the CMR the vane can not estimate the viscosity of the fluids as inertial forces and effects caused by the GNF change the vane flow. Thus, the vane is restricted to operating as a viscometer at low angular velocities.

Most rotational viscometers are designed so that the range of the torque for the measurements is relatively small. For this reason an approximate value can be obtained even when the viscosity varies in an unknown or unsuspected way.

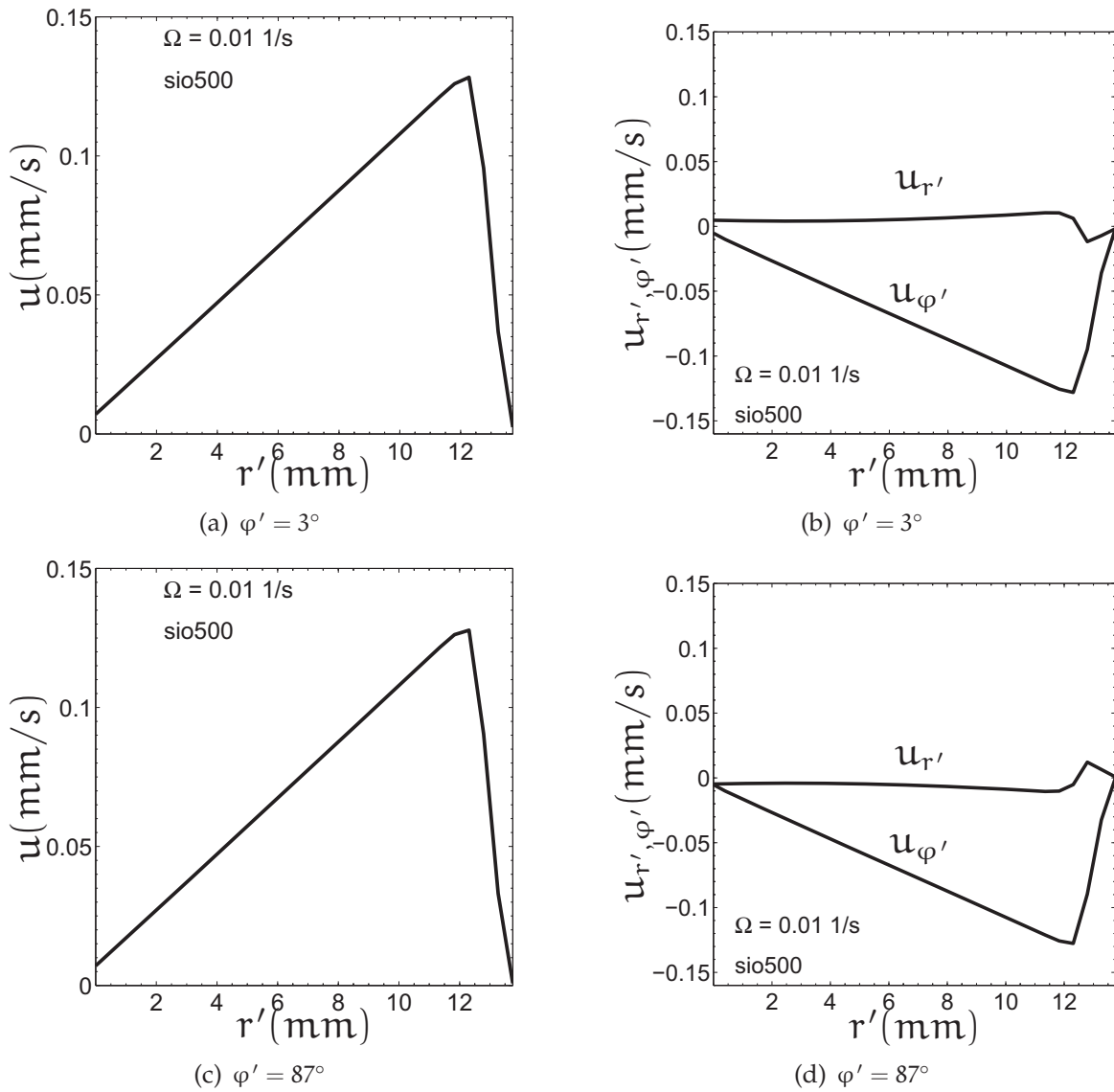


Figure 10.5: Profiles of the total velocity and its components at different angles and radial locations for the NF. Angular velocity $\Omega = 0.01\text{s}^{-1}$, \circ .

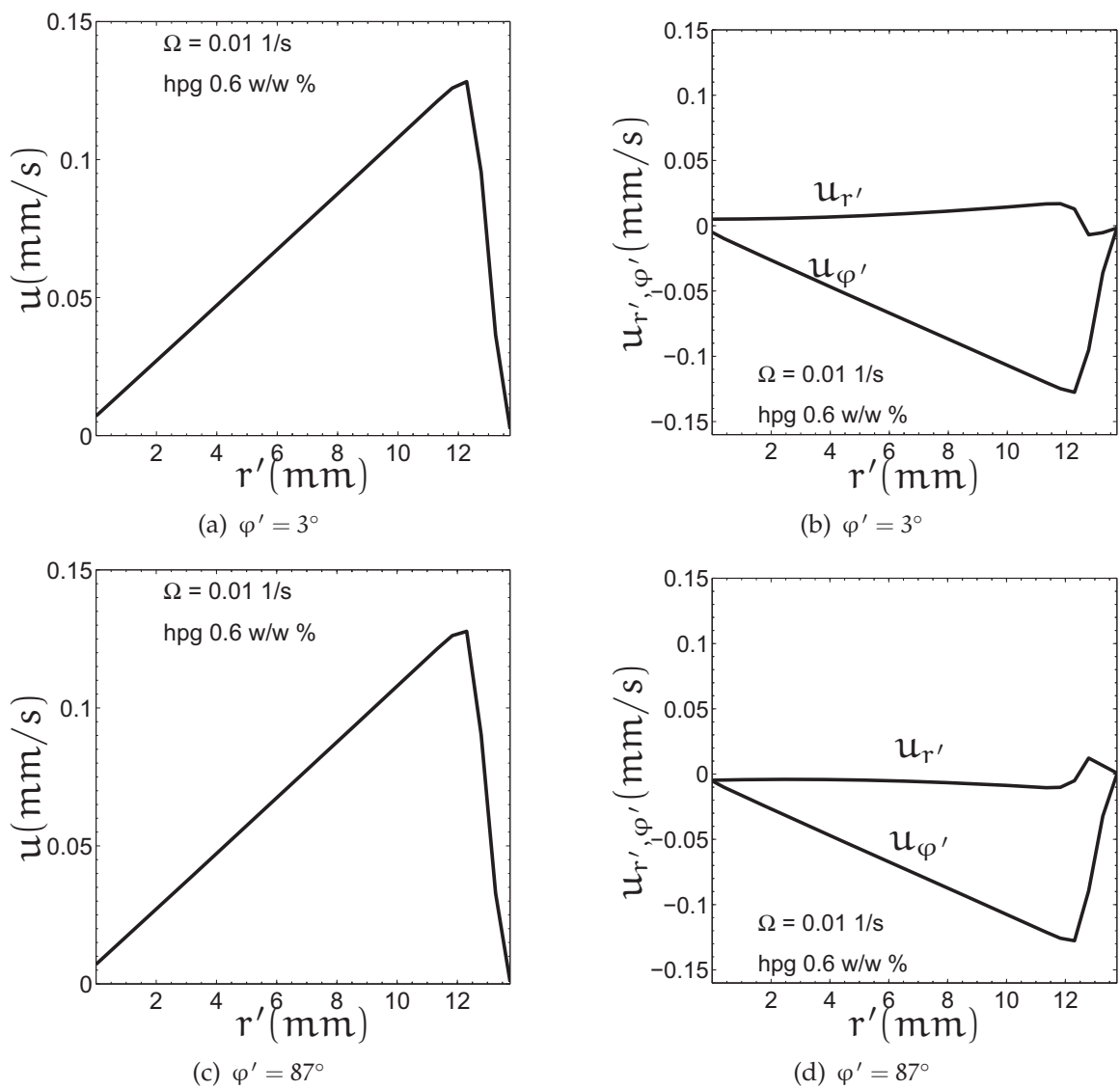


Figure 10.6: Profiles of the total velocity and its components at different angles and radial locations for the GNF. Angular velocity $\Omega = 0.01 \text{ s}^{-1}$, \circ .

10.4 Profiles of the velocity along the gap

The profiles of the total velocity along the gap (region between the edge of the vane and the outer cup) decrease continuously for any type of fluid used, from any selected location on the edge of the vane up to the outer cup.

Concerning the shape of the profiles there is practically no difference among them as figs. 10.7 and 10.8 show. The velocity is slightly higher at $x = 0.0$ mm. At the other locations it can be interpreted as a symmetric profile. For example, at $y = 0.5$ u_x dominates over u_y whereas at $x = 0.5$ mm the roles are inverted but the shape and the magnitudes are preserved. In table 10.2 the locations are given for the velocity profiles along the gap.

Velocity			
along	$x = 0.5$	$r_v \leq y \leq r_o$	$\varphi' = 90$
along	$x = 0.0$	$r_v \leq y \leq r_o$	$\varphi = 90$
along	$y = 0.5$	$r_v \leq x \leq r_o$	$\varphi' = 0$

Table 10.2: Locations for the velocity profiles along the gap.

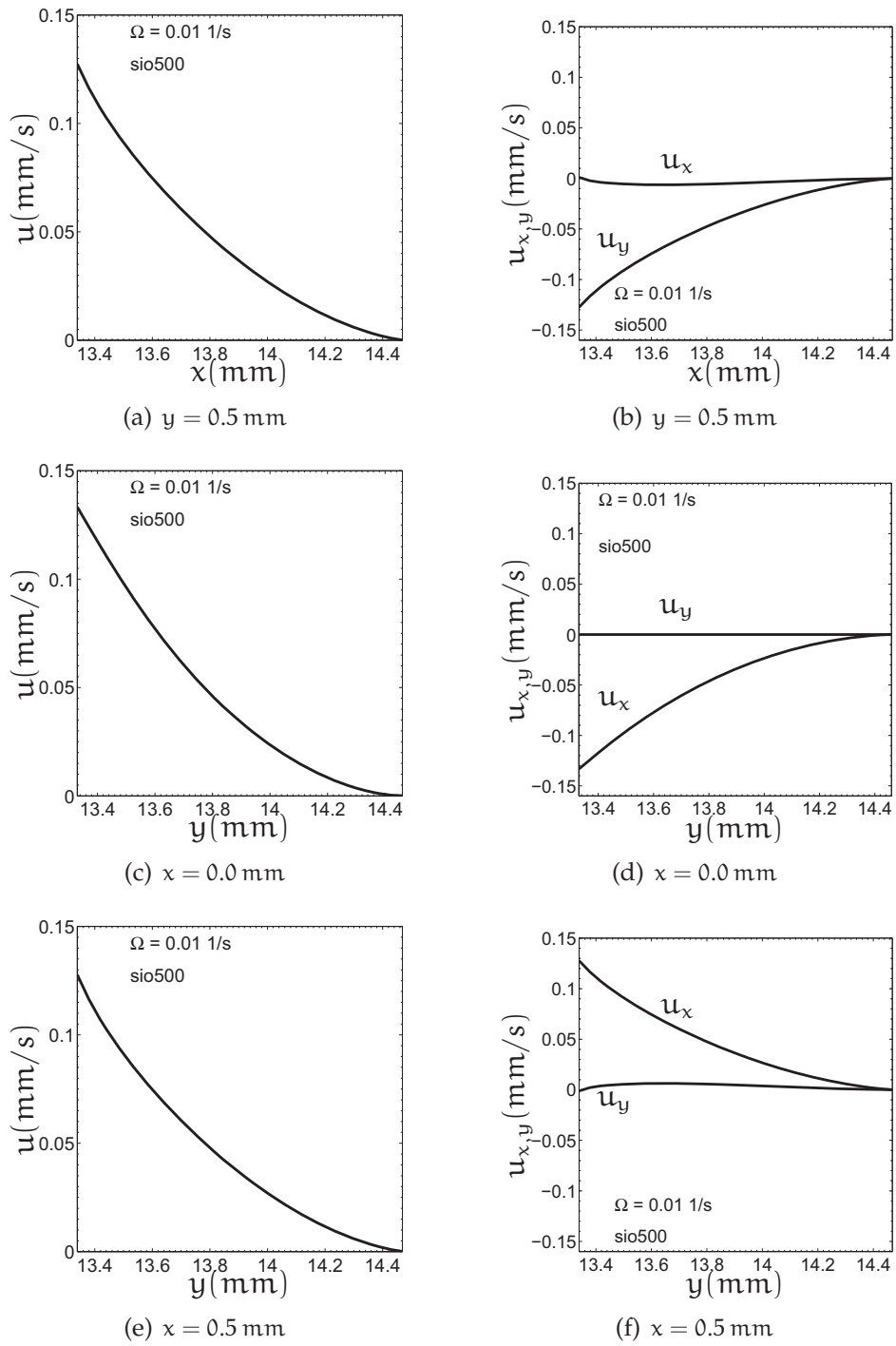


Figure 10.7: Profiles of the total velocity and its components at different angles and radial locations for the NF. Angular velocity $\Omega = 0.01 \text{ s}^{-1}$, \circ .

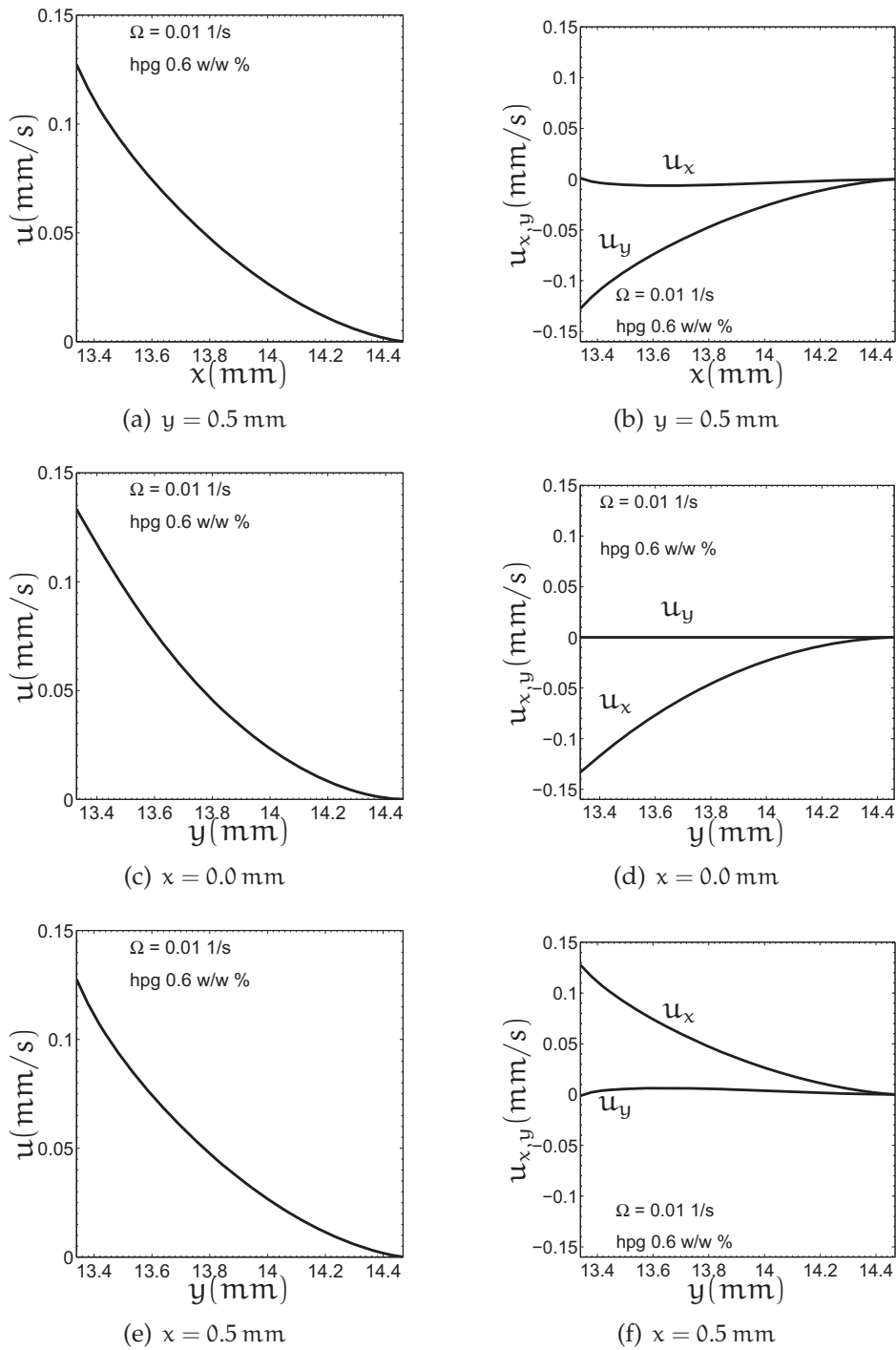


Figure 10.8: Profiles of the total velocity at different angles and radial locations for the GNF. Angular velocity $\Omega = 0.01 \text{ s}^{-1}$, \circ .

10.5 Vane flow and ideal solid-body rotation

In previous sections we have seen that the usual assumptions of solid-body rotation do not apply for vane flow. A direct comparison of the velocity profile for vane flow at $\varphi = 45^\circ$ with the velocity profile of a solid-body rotation that would occur is shown in fig. 10.9.

There it can be seen that there is no similitude neither in quantitative nor qualitative behavior. If a circular pattern would develop, as usually assumed, the velocity profiles would get a constant value in the φ' direction ($0 \leq r' \leq r'_{\max}$) and the velocity profiles would have the same shape. We have seen that the profiles of the total velocity and its components differ in shape and in magnitude at any φ' (figs. 10.3–10.6).

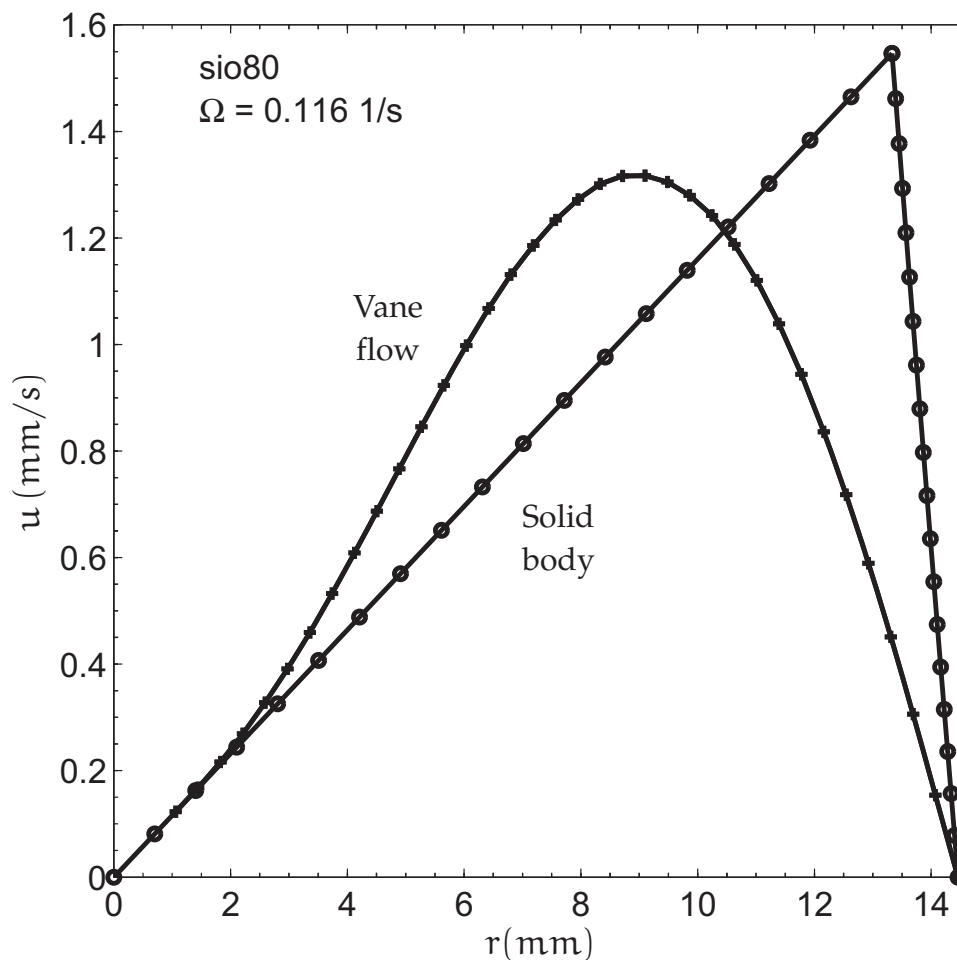


Figure 10.9: Profile of the total velocity: at $\varphi = 45^\circ$ for vane flow and ideal profile (solid-body rotation), Newtonian fluid at $\Omega = 0.116\text{s}^{-1}$.

10.6 Shear rate along the gap and the edge of the vane

The fluid within the blades of the vanes are less subject to shear. Figures 10.10 and 10.11 show the shear-rate distribution for the NF and the GNF along the edge of the vane.

At the tips of the vane a singularity can occur (Atkinson et al. [5]). In our case, to overcome these difficulties, we use data from locations very close to the tips. Previous research works carried out by Keentok ([48]) and by Barnes et al. ([11]) for vane blades of zero thickness already pointed out that stress at the tip of the vane has a sharp peak. In fig. 10.10 one can clearly see for the NF case that the shear rate along the edge of the vane starts to increase at the vane tips. It reaches a maximum value at a position near the vane tip and then it starts to decrease gradually until it reaches a local minimum-value at the center of the edge. The center of the edge can be seen as an inflection point of the shear-rate profile. In the case of the NF the profile is symmetric. The GNF shows a symmetric-shape for low angular velocities.

The shape of the shear-rate profiles in fig. 10.10 differ from those plotted in fig. 10.11 at higher angular velocities. With increasing angular velocity the symmetry of the profiles is broken in the case of the GNF whereas in the NF this remains constant suggesting that the global relationship τ to $\dot{\gamma}$ is constant. In despite the similitude of the shape of the shear rates of both, the NF and the GNF at low angular velocities, the global relationship is not constant for the GNF but changing as the angular velocity is varied. At the point where the symmetry starts to brake non-Newtonian effects are stronger.

The tendency of the shear-rate profiles in the gap shown in figs. 10.12 and 10.13 is to decrease towards the outer cup. The value of the shear rate is of the same order at those selected locations (table 10.2) for each type of fluid. This region could not be resolved experimentally with the PIV technique.

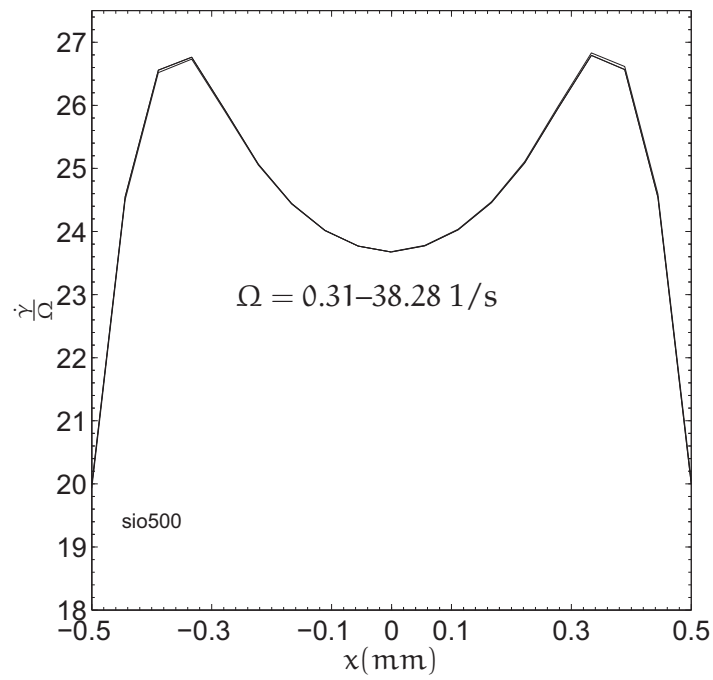


Figure 10.10: Shear rate along the edge of the vane for the NF.

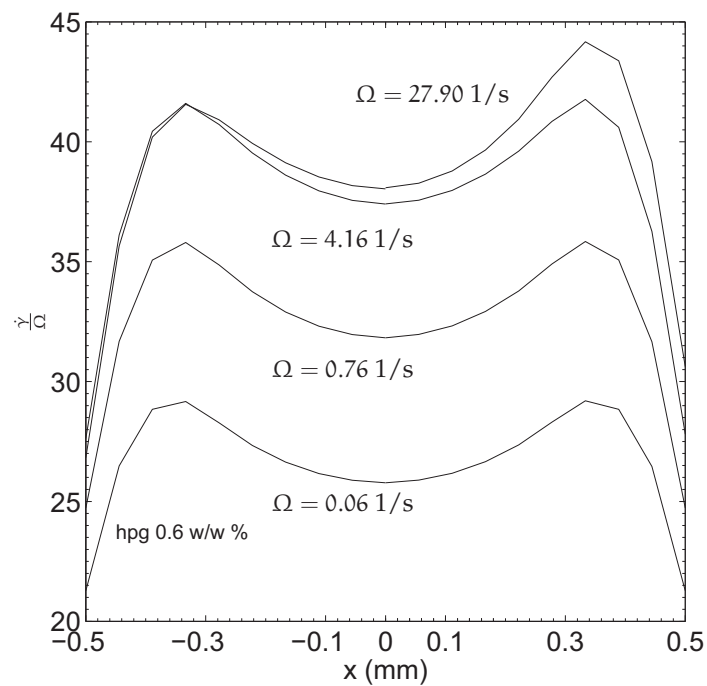


Figure 10.11: Shear rate along the edge of the vane for the GNF.

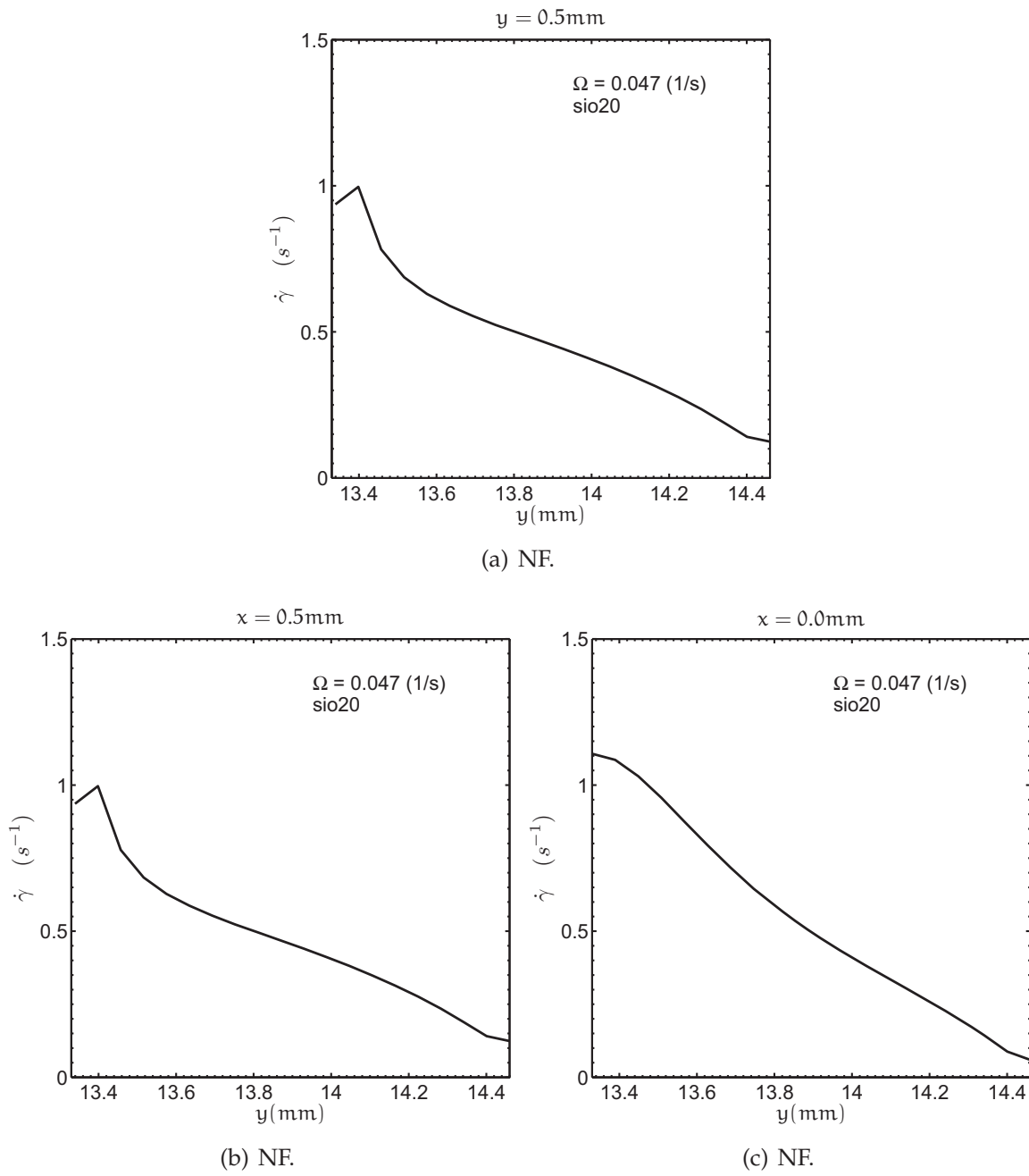


Figure 10.12: Shear rate along the gap for the NF.

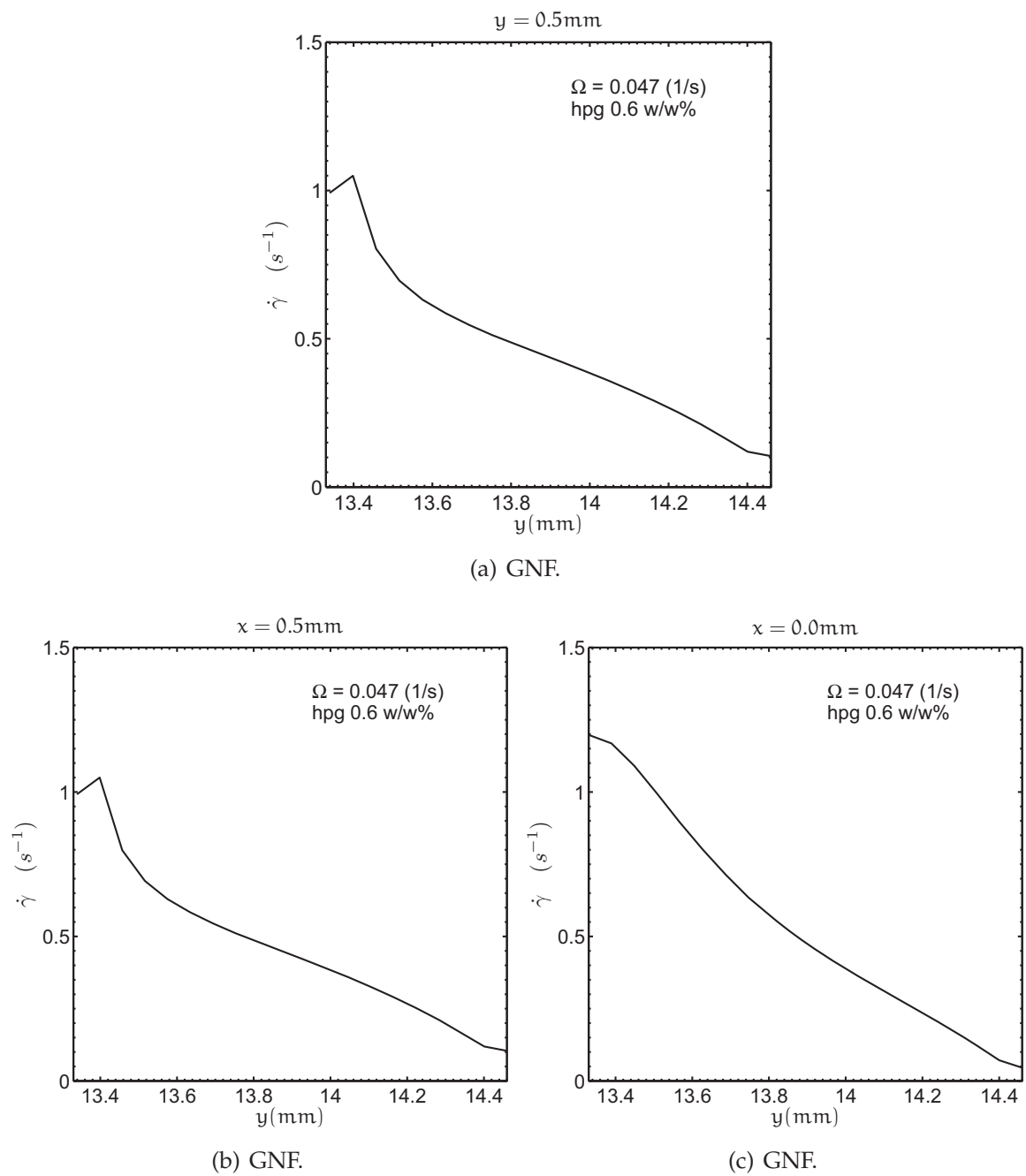


Figure 10.13: Shear rate along the gap for the GNF.

10.7 Torque

The use of a rotational viscometer requires a global relationship between the angular velocity and the applied torque. Unfortunately PIV-measurements could not deliver a flow resolution as high as that found in the numerical simulations near the walls (i.e. vane). Therefore, to complement the flow field we will show in the following sections the results of the simulations for the torque as this can show where our global relationships $M-\Omega$ hold for the measurement of the viscosity.

The numerical visualization of the vane flow is quite useful, especially in those regions where it is difficult or impossible to carry out measurements, for example in the gap or along the edge of the vane. Although experiments can never be performed in the true CMR-regime ($Re = 0$) global $M-\Omega$ correlations hold up to rather moderate Re values. To test our numerical $Re = 0$ calculations with respect to global $M-\Omega$ correlations the torque was calculated. Fig. 10.14 shows the results.

At low angular velocities our experiments are in good agreement with the numerical simulations (fig. 10.14). As we move from the CMR deviations it cannot be disputed: elastic effects can not be neglected. In the region of angular velocities where the numerics predict the experiments quite well a global relationship torque-to-angular velocity can be formulated. This again confirms the use of the vane for viscometric measurements.

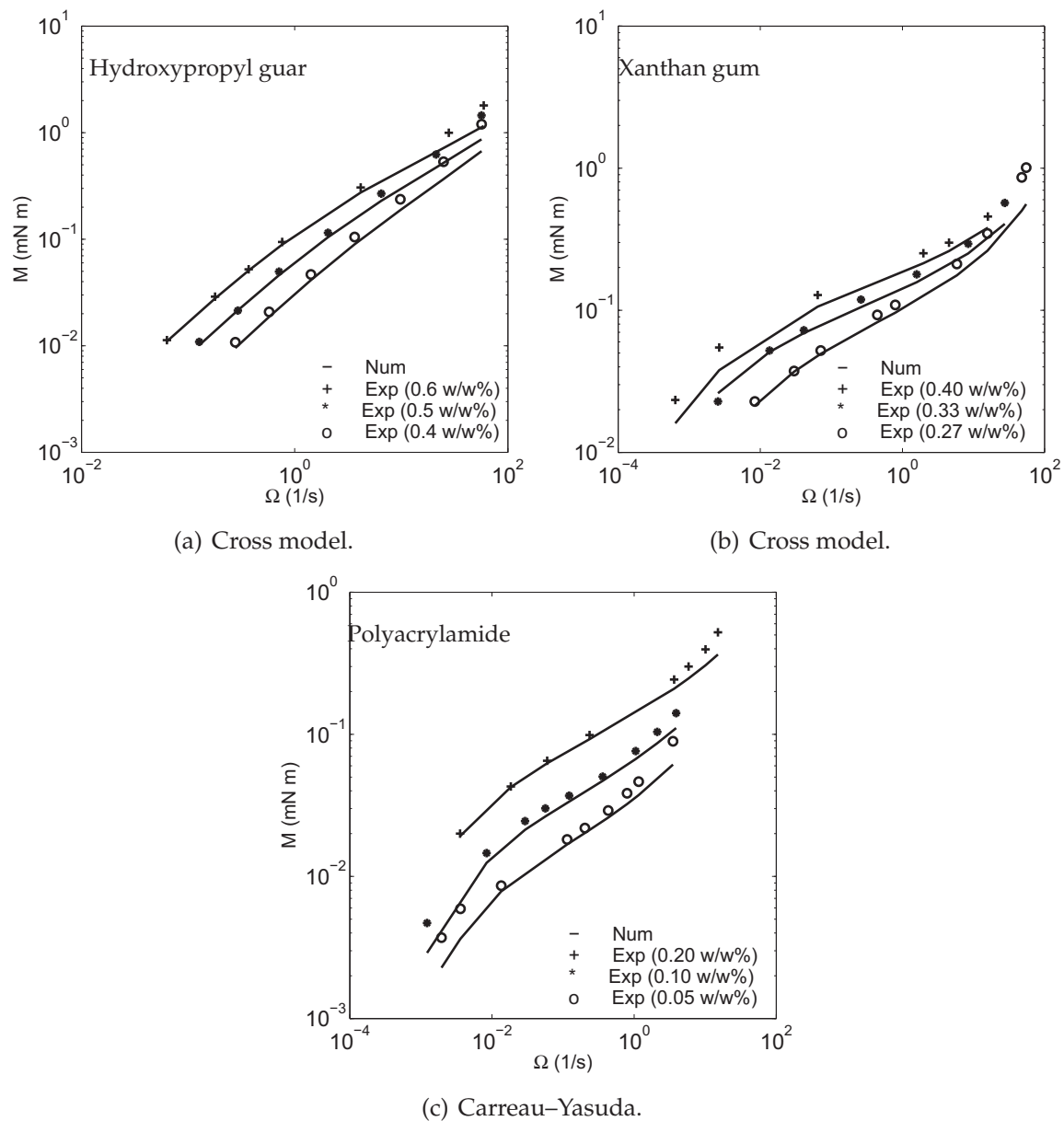


Figure 10.14: Torque vs angular velocity for GNFs with the vane-in-cup geometry (Exp: experimental, Num: numerical).

Bibliography

- [1] Adrian, R. J.: Particle-imaging techniques for experimental fluid mechanics. *Annual review of fluid mechanics*, vol. 23, 261–304, 1991.
- [2] Alderman N.J., Meeten G.H. and Sherwood J.D.: Vane rheometry of bentonite gels. *Journal of non-Newtonian fluid mechanics*, vol. 39, 291–310, 1991.
- [3] Anton-Paar Messtechnik: Measuring systems and manual of operation, 1998.
- [4] Aris R.: *Vectors, tensors, and the basic equations of fluid mechanics*. Dover publications, Inc., New York, 1962.
- [5] Atkinson C. and Sherwood J. D.: The torque on a rotating n-bladed vane in a Newtonian fluid or linear elastic medium. *Proceedings of the royal society London, A*, vol. 438, 183–196, 1992.
- [6] Jaehne B.: *Digital image processing: concepts, algorithms and scientific applications*. Springer, fourth ed., 1997.
- [7] Badino A.C. Jr., Facciotti M.C.R. and Schmidell W.: Construction and operation of an impeller rheometer for on-line rheological characterization of non-Newtonian fermentation broths. *Brazilian journal of chemical engineering*, vol. 14, 1–11, 1997.
- [8] Barnes H. A.: A review of the slip (wall depletion) of polymer solutions, emulsions and particle suspensions in viscometers: its cause, character, and cure. *Journal of non-Newtonian fluid mechanics*, vol. 56, 221–251, 1995.
- [9] Barnes H. A.: Thixotropy – a review. *Journal of non-Newtonian fluid mechanics*, vol. 70, 1–33, 1997.
- [10] Barnes H. A.: The yield stress –a review or 'παντα ρει' –everything flows? *Journal of non-Newtonian fluid mechanics*, vol. 81, 133–178, 1999.
- [11] Barnes H. A. and Carnali J. O.: The vane-in-cup as a novel rheometer geometry for shear thinning and thixotropic materials. *Journal of rheology*, vol. 6(36), 841–866, 1990.
- [12] Barnes H. A. and Nguyen Q.D.: Rotating vane rheometry – a review. *Journal of non-Newtonian fluid mechanics*, vol. 98, 1–14, 2001.
- [13] Barnes H.A., Hutton J.F. and Walters K.: *An introduction to rheology*. Rheology series, Elsevier, Netherlands, 3 ed., 1993.

BIBLIOGRAPHY

- [14] Bird B. R., Stewart W. E. and Lightfoot E.N.: Transport phenomena. John Wiley and sons, Inc., Wisconsin, USA, 1960.
- [15] Bravian C., Lalante A. and Parker A.: Vane rheometry with a large, finite gap. *Applied rheology*, vol. 12, 81–87, 2002.
- [16] Brenner G.: Numerische Simulation komplexer fluider Transportvorgänge in der Verfahrenstechnik, Habilitationsschrift. Lehrstuhl für Strömungsmechanik, Friedrich–Alexander–Universität, Erlangen–Nürnberg, 2001.
- [17] Breuer, M.: Numerische Strömungsmechanik 1, Vorlesungsskript. Lehrstuhl für Strömungsmechanik, Friedrich–Alexander–Universität Erlangen–Nürnberg, 2003.
- [18] Briggs J.L., Steffe J.F. and Ustunol Z.: Vane method to evaluate the yield stress of frozen ice cream. *Journal of dairy science*, vol. 79, 527–531, 1996.
- [19] Britton and Callaghan: Nuclear magnetic resonance visualization of anomalous flow in cone-and-plate rheometry. *Journal of rheology*, vol. 41, 1365, 1997.
- [20] Brunn, P. O.: Rheology/rheometry: an introduction, Lecture notes. Lehrstuhl für Strömungsmechanik, Friedrich–Alexander–Universität Erlangen–Nürnberg, 2003.
- [21] Brunn, P.O.: Non–Newtonian fluid mechanics, Lecture notes. Lehrstuhl für Strömungsmechanik, Friedrich–Alexander–Universität Erlangen–Nürnberg, 2000.
- [22] Servais C., Carozza S., Roberts I., Jones R. and Burbidge A.: Probing the bulk rheological properties of foam systems. Proceedings, 2001.
- [23] Castell–Perez E. and Steffe J.: Evaluating shear–rates for power law fluids in mixer viscosimetry. *Journal of texture studies*, vol. 21, 439–453, 1990.
- [24] Chakrabarti S., Seidl B., Vorwerk J. and Brunn P.O.: The rheology of hydroxypropylguar (HPG) solutions and its influence on the flow through a porous medium and turbulent tube flow, respectively (Part 1). *Rheologica acta*, vol. 30, 114–123, 1991.
- [25] Cheng, D. C. H.: The tensile strength of powders. *Chemical engineering science*, vol. 23, 1405–1420, 1968.
- [26] Churchill S. W. and Usag R.: A general expression for the correlation of rates of transfer and other phenomena. *American institute of chemical engineers journal*, vol. 18(6), 1121–1128, 1972.

- [27] Cross M. M.: Rheology of non-Newtonian fluids: a new flow equation for pseudoplastic systems. *Journal of colloid science*, vol. 20, 417–437, 1965.
- [28] Daubert C.R., Tkachuk J.A. and Truong V.D.: Quantitative measurement of food spreadability using the vane method. *Journal of texture studies*, vol. 29, 427–435, 1998.
- [29] De Souza Mendes P.R. and Dutra E.S.S.: Viscosity function for yield-stress liquids. *Applied rheology*, vol. 14(6), 296–302, 2004.
- [30] DIN13 342: Nicht-Newton'sche Flüssigkeiten. Begriffe, Stoffgesetze, 1976.
- [31] DIN53 018: Messung der dynamischen Viskosität newtonscher Flüssigkeiten mit Rotationsviskosimetern, 1976.
- [32] DIN53 019: Messung von viskositäten und Fließkurven mit Rotationsviskosimetern mit Standardgeometrie, 1980.
- [33] Farias M.E., De Souza Mendes P.R. and Maia Vinagre H.T.: Characterization of viscoplastic materials with rotating vane and bob rheometry, kindly provided by Prof. De Souza Mendes.
- [34] Ferziger J. H. and Perić, M.: Computational methods for fluid dynamics. Springer, second ed., 1999.
- [35] Fisher D. T., Boger D. V. and Scales P. J.: Measurement errors in yield stress rheometry that arise from torque auto zero. *Applied rheology*, vol. 16(4), 206–209, 2006.
- [36] Glenn III T. A., Keener K. M. and Daubert C. R.: A mixer viscometry approach to use vane tools as steady shear rheological attachments. *Applied rheology*, vol. 10(2), 80–89, 2000.
- [37] Godleski E. S. and Smith J.C.: Power requirements and blend times in the agitation of pseudoplastic fluids. *American institute of chemical engineers journal*, vol. 8(5), 617–620, 1962.
- [38] Gonzalez R.C. and Wintz, P.: Digital image processing. Addison-Wesley, second ed., 1987.
- [39] Haimoni A. and Hannant D.J.: Developments in the shear vane test to measure the gel strength of oilwell cement slurry. *Advances in cement research*, vol. 1(4), 221–229, 1988.
- [40] Hansen E. K. and Fellingner T. L.: Yield stress and physical data results for the tank F19 radioactive mound sample and tank 19F simulant samples (U). *Report wsrc-tr-2002-00070*, Westinghouse Savannah River company, USA, 2002.

BIBLIOGRAPHY

- [41] Harnett J. P. and Hu R.Y.Z.: Technical note: the yield stress –an engineering reality. *Journal of rheology*, vol. 4(33), 671–679, 1989.
- [42] Helmreich A., Vorwerk J., Steger R., Müller and Brunn P.O.: Non-viscous effects in the flow of xanthan gum solutions through a packed bed of spheres. *Chemical engineering journal*, vol. 59, 111, 1995.
- [43] Höcker H. and Langer G.: Zum Leistungsverhalten begaster Rührer in Newtonschen und nicht-Newtonschen Flüssigkeiten. *Rheologica acta*, vol. 16, 400–412, 1977.
- [44] Holweg J.: Charakterisierung von viskoelastischen Flüssigkeiten durch Ihr Strömungsverhalten in Kugelschüttungen. Ph.D. thesis, Friedrich–Alexander–Universität Erlangen–Nürnberg, 1989.
- [45] Krieger I. M.: Shear rate in the Couette viscometer. *Transactions of the society of rheology*, vol. 12(1), 5–11, 1968.
- [46] Savins J. G. and Metzner A. B.: Radial (secondary) flows in rheogoniometric devices. *Rheologica acta*, vol. 9(3), 365–373, 1970.
- [47] Jasak, H.: Error analysis and estimation for the finite volume to fluid flows. Ph.D. thesis, University of London, 1996.
- [48] Keentok M., Milthorpe, J. F. and O'Donovan, E.: On the shearing zone around rotating vanes in plastic liquids: theory and experiment. *Journal of non-Newtonian fluid mechanics*, vol. 17, 23–35, 1985.
- [49] Krulis M. and Rohm H.: Adaption of a vane tool for the viscosity determination of flavoured yoghurt. *European food and research technology*, vol. 218, 598–601, 2004.
- [50] Krüßmann R. and Brunn P.O.: Elastische Effekte bei der Strömung viskoelastischer Fluide durch Haufwerke. *Chemie Ingenieur Technik*, vol. 73, 1602, 2001.
- [51] Laney C. B.: Computational gas dynamics. Cambridge university press, United Kingdom, 1998.
- [52] Läger J., Müller M. and Tyrach J.: A new ball measuring system for large particle suspensions. *Applied rheology*, vol. 9, 143, 1999.
- [53] Martinez–Padilla L.P. and Rivera–Vargas C.: Flow behaviour of mexican sauces using a vane–in–a–large cup rheometer. *Journal of food engineering*, vol. 72(2), 189–196, 2006.

- [54] Metzner A. B., Feehs R. H., Lopez R. H., Otto R.E. and Tuthill J.D.: Agitation of viscous Newtonian and non-Newtonian fluids. *American insitute of chemical engineers journal*, vol. 7(1), 3–9, 1961.
- [55] Mooney M.: Explicit formulas for slip and fluidity. *Journal of rheology*, vol. 2, 210–222, 1931.
- [56] Mooney M. and Ewart R.H.: The conicylindrical viscometer. *Physics*, vol. 5, 530–534, 1935.
- [57] Müller M. and Brunn P.O.: Auslegung der Strömung in Schüttungen bei nicht-Newtonoschen Flüssigkeiten. *Chemie Ingenieur Technik*, vol. 69, 1636, 1997.
- [58] Nguyen D.Q. and Boger D. V.: Yield stress measurements for concentrated suspensions. *Journal of rheology*, vol. 27(4), 321–349, 1983.
- [59] Nguyen D.Q. and Boger D.V.: Direct yield stress measurement. *Journal of rheology*, vol. 29, 335–347, 1985.
- [60] Ottino J.M.: The kinematics of mixing: stretching, chaos and transport. Cambridge university press, 1989.
- [61] Owens R.G. and Phillips T. N.: Computational rheology. Imperial college press, 2002.
- [62] Liddell P. V. and Boger D. V.: Yield stress measurements with the vane. *Journal of non-Newtonian fluid mechanics*, vol. 63, 235–261, 1996.
- [63] Perez-Foguet A., Ledesma A. and Huerta A.: Analysis of the vane test considering size and time effects. *International journal for numerical and analytical methods in geomechanics*, vol. 23, 383–412, 1999.
- [64] Peters G.W.M., Schoonen J.F.M., Baaijens F.P.T. and Meijer H.E.H.: On the performance of enhanced constitutive models for polymer melts in a Cross-slot flow. *Journal of non-Newtonian fluid mechanics*, vol. 82, 387–427, 1999.
- [65] Popoff B., Egorov Y. and Menter F.: Simulation of the astar benchmark test cases with CFX-5. ASTAR international workshop on 'advanced numerical methods for multidimensional simulation of two-phase flow', Garching, Germany, 2003.
- [66] Princen H.M.: A novel design to eliminate end effects in a concentric cylinder viscometer. *Journal of rheology*, vol. 2(30), 271–283, 1986.
- [67] Raffel M., Willert C. and Kompenhans J.: Particle image velocimetry: a practical guide. Springer-Verlag, 1998.

BIBLIOGRAPHY

- [68] Rao M.A. and Cooley H.J.: Determination of effective shear rates in rotational viscometers with complex geometries. *Journal of texture studies*, vol. 15, 327–335, 1984.
- [69] Rolon–Garrido V.H., J., P.-G. and Acosta, M. V.: Vane rheometry of an aqueous solution of worm–like micelles. *Revista mexicana de fisica*, vol. 49(1), 40–44, 2002.
- [70] Schramm G.: A practical approach to rheology and rheometry. Gebrueder HAAKE GmbH, Karlsruhe, second ed., 2000.
- [71] Shermann F.: Viscous flow. McGraw–Hill, California, 1990.
- [72] Sherwood J. D. and Meeten G. H.: The use of the vane to measure the shear modulus of linear elastic solids. *Journal of non–Newtonian fluid mechanics*, vol. 41, 101–118, 1991.
- [73] Stokes J. R. and Telford J. H.: Measuring the yield behaviour of structured fluids. *Journal of non–Newtonian fluid mechanics*, vol. 124, 137–146, 2004.
- [74] Tyrach J.: Rheologische Charakterisierung von zementären Baustoffsystemen. Ph.D. thesis, Friedrich–Alexander–Universität Erlangen–Nürnberg, 2000.
- [75] Vorwerk J.: Separation elastischer und viskoser Effekte in der Haufwerkströmung. Ph.D. thesis, Friedrich–Alexander–Universität Erlangen–Nürnberg, 1993.
- [76] Wernet M. P.: Application of DPIV to study both steady and transient turbomachinery flows. *Optics and Laser Technology*, vol. 32, 497–525, 2000.
- [77] Westerweel J.: Fundamentals of particle image velocimetry. *Measurement science and technology*, vol. 8, 1379–1392, 1997.
- [78] Whorlow R. W.: Rheological techniques. Ellis Horwood Ltd., Chichester, 1980.
- [79] Willert C.E. and Gharib M.: Digital particle image velocimetry. *Experiments in fluids*, vol. 10, 181–193, 1991.
- [80] Yan J. and James A. E.: The yield surface of viscoelastic and plastic fluids in a vane. *Journal of non–Newtonian fluid mechanics*, vol. 70, 237–253, 1997.
- [81] Yang T.M.T. and Krieger I.M.: Comparison of methods for calculating shear rates in coaxial viscometers. *Journal of rheology*, vol. 22(4), 413–421, 1978.
- [82] Yoon W.B., Gunasekaran S. and Park J.W.: Evaluating viscosity of surimi paste at different moisture content. *Applied rheology*, vol. 14(3), 133–139, 2004.

- [83] Yoshimura A. S. and Prud'homme R. K.: A comparisson of techniques for measuring yield stresses. *Journal of rheology*, vol. 31(8), 699–710, 1987.
- [84] Zlokarnik Marko: Dimensional analysys and scale–up in chemical engineering. Springer–verlag, Berlin, 1991.

Experimentelle und numerische Untersuchungen für eine Flügeldrehkörperströmung

**Der technischen Fakultät der
Universität Erlangen–Nürnberg
zur Erlangung des Grades**

DOKTOR–INGENIEUR

vorgelegt von

Alejandro Peugnet

Erlangen, 2009

Als Dissertation genehmigt von
der technischen Fakultät der
Universität Erlangen–Nürnberg

Tag der Einreichung:	21.12.2005
Tag der Promotion:	25.07.2008
Dekan:	Prof. Dr.-Ing. habil. J. Huber
Berichterstatter:	Prof. Dr.-Ing. P. O. Brunn
	Prof. Dr.-Ing. B. Gampert

Inhaltsverzeichnis

Zusammenfassung	i
1 Einleitung	iv
2 Literaturübersicht	5
2.1 Einfluss der Abmessungen des Flügeldrehkörpers.....	14
2.2 Endeffekte.....	15
2.3 Ziel der Arbeit.....	16
3 Numerische Methode	19
3.1 Finite-Volumen-Methode (FVM).....	19
3.2 Allgemeine Transportgleichung.....	20
3.3 Dimensionlose Formulierung.....	23
3.4 Diskretisierung der allgemeinen Transportgleichung mit der FVM.....	24
3.5 Diskretisierung des diffusiven Flusses.....	24
3.6 Diskretisierung des Quellterms.....	27
3.7 Verwendete Software.....	27
3.7.1. CFX Simulationsmodule.....	28
4 Flügeldrehkörper und Aufgabestellung	31
4.1 Flügeldrehkörper.....	31
4.2 Idealisierte Voraussetzungen.....	31
4.3 Drehmoment eines rotierenden Flügeldrehkörpers.....	32
4.4 Grundgleichungen.....	34
4.4.1 Randbedingungen.....	35
4.5 Numerisches Gitter für die FVM des Flügeldrehkörpers.....	38
5 Optische Methode	41
5.1 Particle-Image Velocimetry (PIV) Technik.....	41
5.1.1 Bildaufnahme.....	42
5.1.2 Interrogation.....	44
5.1.3 Datenvalidierung.....	45
5.1.4 Datenanalyse	45
5.1.5 Verschiebung der Tracerpartikeln.....	46
6 Materialien und Geräte	49
6.1 Werkstoffe.....	49
6.1.1. Newtonsche Flüssigkeiten.....	49

6.1.2 Nicht-Newtonsche Flüssigkeiten.....	50
6.2 Geräte.....	52
6.2.1 Das Rheometer Physica UDS 200.....	52
6.2.2 Konzentrisches Zylinder Meßsystem (CC 27).....	53
6.2.3 Flügeldrehkörper Meßsystem	54
6.2.4 PIV Versuchsanlage.....	55
7 Fließkurven	59
7.1 Newtonsche Flüssigkeiten.....	59
7.2 Nicht-Newtonsche Flüssigkeiten.....	60
7.2.1 Vorbereitung der Lösungen.....	61
7.2.2 Hydroxypropyl guar.....	62
7.2.3 Xanthan Gum.....	62
7.2.4 Polyacrylamid.....	62
7.3 Charakterisierung mit der Viskosität der Lösungsmittel.....	64
8 Der Flügeldrehkörper als Viskometer	67
8.1 Dimensionlose Formulierung.....	67
8.2 Bestimmung der Scherrate mit dem Flügeldrehkörper.....	73
9 PIV Messungen	85
9.1 Strömung zwischen den Armen des Flügeldrehkörpers.....	85
9.2 Koordinatentransformation.....	87
9.3 Profile der Geschwindigkeit.....	90
10 Numerische Simulationen für die Flügeldrehkörperströmung	95
10.1 Strömungsfeld.....	96
10.2 Profile des Betrags der Geschwindigkeit.....	100
10.3 Profile der Geschwindigkeit neben dem Flügeldrehkörper.....	104
10.4 Profile der Geschwindigkeit entlang der Spalte.....	107
10.5 Flügeldrehkörperströmung und ideale Rotation eines festen Körpers.....	110
10.6 Scherrate entlang der Kante des Flügeldrehkörpers und außerhalb.....	111
10.7 Drehmoment.....	115
Literaturverzeichnis	117
A Meßsysteme für die PIV Messungen	137
A.1 Zylinder und Flügeldrehkörper.....	138
B Fließkurven	139
C Bestimmung der Fließgrenze	142

D Profile der Geschwindigkeit für NF und GNF	144
E Stromlinien für NF und GNF	150
Abbildungsverzeichnis	151
Tabellenverzeichnis	153
Index	155

Zusammenfassung

Ziel der Arbeit war herauszufinden ob, und falls ja unter welchen Einschränkungen, ein Flügeldrehkörper (FDK) als Viskometer verwendet werden kann selbst für viskoelastische Flüssigkeiten. Das Rational für diesen Versuch basiert auf der Tatsache, daß in allen Viskosimetern, die die Vernachlässigung der Trägheit voraussetzen, eine rein viskometrische Strömung nicht existiert und nicht existieren kann, wie klein auch immer Re ist. Bekannte Beispiele sind die Kegel-Platte und Platte-Platte Viskometer. Sekundärströmungen beeinflussen immer die ideale lokale Strömungskinetik. Nichts desto trotz muß Re hinreichend groß sein, bevor diese Änderungen des lokalen Strömungsfeldes meßbare Auswertung auf globale Beziehungen haben, die zur Bestimmung von η verwendet werden. Für Rotationsviskometer sind dies die $M-\Omega$ Beziehungen.

Als Flüssigkeiten wurden verschiedene kommerzielle Polymerlösungen verwendet. Drei unterschiedliche Typen kamen zum Einsatz nämlich Polyacrylamid, das Biopolymer Hydroxypropyl guar und Xanthan Gum, ebenfalls ein Biopolymer allerdings mit Helixstruktur. Drei bzw. vier verschiedene Konzentrationen wurden für jede Lösung angesetzt.

Mit Hilfe eines konzentrischen Zylinders Viskometers (KZV) vom Searle Typ wurden die Fließkurven ermittelt. Abhängig von Konzentration ergeben sich quantitativ unterschiedliche Fließkurven, die aber für jeden Polymertyp qualitativ ähnlich aussehen. Damit liegt es nahe nach einer universellen Darstellung zu suchen, bei der η_0 die einzige Größe ist, die von der Konzentration abhängt. Es zeigte sich, daß für die beiden Biopolymere eine universelle Cross-ähnliche Beschreibung ausreicht, während für Polyacrylamid ein Carreau-Yasuda Modell bessere Dienste tut. Unabhängig von diesen Details erlaubt eine universelle Darstellung die Bestimmung einer Fließkurve $\eta(\dot{\gamma})$ für jede Konzentration.

Um den FDK als Viskometer zu verwenden bedarf es zunächst der Kenntnis der Master-curve (MC) $Ne = Ne(Re)$. Diese wurde mit Newtonschen Flüssigkeiten (NF) erstellt. Dazu dienten verschiedene Silikonöle mit niedrigen Molekulargewicht. Der Einfluß von η ist am größten im Bereich der schleichenden Strömung (SS), wo ja bekanntlich $Ne = c/Re$ gelten muß. In unserem Fall gilt diese Beziehung bis zu Re 's von etwa 5, wobei sich experimentell $c = 13.51$ herausstellte. Da diese Konstante doch beträchtlich von der Konstanten abweicht, die bei unserem kommerzie-

len KZV vom Hersteller vorgegeben ist (mit gleichen Abmessungen wie unsere FDK-Apparatur) ist klar, daß in beiden Geräten doch recht unterschiedliche Strömungsformen vorliegen müssen.

Für nicht-Newton'sche Flüssigkeiten (NNF's), rein viskose oder viskoelastische, ist η keine Konstante, sondern hängt von $\dot{\gamma}$ ab. Deswegen wurde eine Referenzviskosität η_{ref} verwendet, um Re_{ref} zu definieren. Hierzu wurde die Lösungsmittelviskosität (d.h. Wasser) herangezogen.

Ausgehend von der Vorstellung, daß sich der SS-Bereich durch $NeRe = c$ beschreiben lässt verlangt eine Änderung von $NeRe_{\text{ref}}$ über Re_{ref} zu $NeRe = c$ in doppelt-logarithmischer Darstellung eine Verschiebung unter 45° . Die Größe dieser Verschiebung liefert direkt η . Damit erhält man für jedes Ω die Funktion $\eta(\Omega)$. Durch Gleichsetzen von $\eta(\Omega)$ mit der Fließkurve $\eta(\dot{\gamma})$ erhält man eine Beziehung zwischen Ω und $\dot{\gamma}$. Solange Ω klein genug ist (Re klein) stellt sich diese Beziehung als linear heraus, d.h. $\dot{\gamma} = c_\gamma \Omega$. Obwohl c_γ von Flüssigkeit zu Flüssigkeit etwas variiert liefert, was η betrifft, die Näherung $c_\gamma \approx 4$ in unserem Fall zufriedenstellende Ergebnisse für alle untersuchten Flüssigkeiten. Damit ist die Tauglichkeit des FDK als Viskosimeter nachgewiesen.

Allerdings sind dem ganzen auch Grenzen gesetzt. Es zeigt sich nämlich daß bei höheren Re 's für viskoelastische Flüssigkeiten Abweichungen von $NeRe = c$ auftreten, für die bei Newton'schen Flüssigkeiten immer noch $NeRe = c$ gilt. Dies ist am deutlichsten zu sehen wenn $\eta(\dot{\gamma})$ direkt mit $\eta(\Omega)$ verglichen wird. Für höhere Re 's ist die Funktion $\dot{\gamma} = \dot{\gamma}(\Omega)$ nicht mehr linear. Die Elastizität der Flüssigkeit macht sich bemerkbar. Als nicht-lineare Größe macht sich diese in der M - Ω Beziehung bei höheren $\dot{\gamma}$ bemerkbar und dies umso stärker, je elastischer die Flüssigkeit ist. Bei schwach elastischen Flüssigkeiten ist die Trägheit der limitierende Faktor (wie im Kegel-Platte und Platte-Platte Viskosimeter), bei stark elastischen die Elastizität der Flüssigkeit.

PIV-Messungen unterstreichen das. Selbst Newton'sche Flüssigkeiten zeigen Stromlinien die alles andere als kreisförmig sind. Das bedeutet, daß weder innerhalb des FDK-Bereiches eine Festkörperrotation vorliegt noch außerhalb eine viskosimetrische Strömung herrscht. Dies wäre die Voraussetzung, daß die Trägheit der Flüssigkeit das Strömungsfeld nicht beeinflusst.

Die numerischen Berechnungen für Newton'sche und verallgemeinerte Newton'sche Flüssigkeiten sind auf den wahren SS-Bereich, $Re = 0$, beschränkt. Dabei spielt selbst lokal die Trägheit keine Rolle und die Strömung erscheint stationär. Dies wird am besten verständlich, wenn man sich ein mitrotierendes Koordinatensys-

tem vorstellt. In diesem ist, per definitionem, die Strömung stationär, doch müssen Coriolis- und Zentrifugalkräfte berücksichtigt werden. Allerdings skalieren beide mit Re , d.h. für $Re = 0$ fallen beide heraus, was allerdings auch ihr Name 'Trägheitskräfte' zum Ausdruck bringt. In Übereinstimmung mit den PIV Messungen zeigen die Rechnungen, daß die Stromlinien nicht kreisförmig sind. Trotzdem zeigen die berechneten M - Ω Beziehungen gute Übereinstimmung mit den gemessenen für hinreichend kleine Ω . Daß für große Ω -Werte Abweichungen auftauchen ist nicht verwunderlich. Verallgemeinerte Newtonsche Flüssigkeiten sind rein viskos. Die verwendeten Polymerlösungen sind alle viskoelastisch und die Elastizität läßt sich nur für kleine Ω 's vernachlässigen.

Zusammenfassend läßt sich feststellen, daß der FDK sich durchaus als Viskosimeter verwenden läßt, daß allerdings die Elastizität oder die Trägheit der Flüssigkeit dem Grenzen setzen.

Einleitung

Seit Bingham in den Zwanziger Jahren des 20. Jahrhunderts zum ersten Mal eine nicht-Newton'sche Flüssigkeit modellierte, hat sich die Rheologie, ein Zweig der Kontinuumsmechanik, bei der Untersuchung des Deformationsverhaltens von Stoffen weiterentwickelt. Derartige Untersuchungen umfassen nicht nur die Messung der Deformation des unter bestimmten Spannungen oder Scherungen unterzogenen Stoffes sondern auch seine Anwendung und Modellierung.

Zur Charakterisierung eines Stoffes müssen Daten von Messungen entnommen werden, welche es ermöglichen, die Verformung des Materials darzustellen und zu verstehen, wie diese Deformation auftritt. Dieser Schritt schließt die Modellierung der betroffenen Werkstoffeigenschaft ein, bspw. die Viskosität. Man bringt die auf die Flüssigkeit wirkenden Kräfte (z.B. Drehmoment) in Zusammenhang mit der Deformation (Verformungsgeschwindigkeit) und das sich aus diesen zwei Variablen ergebene Verhältnis liefert Information über die Viskosität.

Um das rheologische Verhalten eines Werkstoffes zu beschreiben und die Daten experimentell zu erfassen, ist ein Rheometer nötig. In diesem Gerät wird versucht, ideale Strömungszustände der Flüssigkeit herzustellen. Ein Beispiel ist ein Rotationsviskosimeter.

Rotationsviskosimeter sind bewährte Geräte, die sowohl im Forschungsbereich als auch in der Industrie angewendet werden.

Wie oben erwähnt, im Fall der Viskosität η verwendet man eine Funktion der Form

$$\eta = f\left(\frac{M}{\Omega}\right), \quad (10.3)$$

wobei M für das eingesetzte Drehmoment und Ω für Winkelgeschwindigkeit stehen, die während des Versuches gemessen wird.

Bei den Rotationsrheometern ist es manchmal notwendig, Versuche mit Geschwindigkeiten oder Drehmomenten durchzuführen, die sehr hoch sind. Das bringt eine beträchtliche auf das System wirkende Trägheitskraft mit sich. Sobald diese eine bestimmte Grenze

überschreitet, entwickelt sich ein unerwünschtes Fließverhalten (Sekundärströmung). Obwohl das einen einschränkenden Faktor darstellt, ist es nicht das einzige Problem, wenn man Messungen durchführt. Auf den Oberflächen können Gleiteffekte (wall slip) auftreten.

Man kann sagen, dass der Gleiteffekt auftritt, wenn sich eine dünne Schicht oder ein Film auf einer festen Wand bildet. So werden Gleichungen, die zur Bestimmung der Viskosität benutzt werden und die auf der Annahme der Haftbedingung (Eng. non-slip) an den Wänden stützen, keine Viskosität vorhersagen. Es ist möglich diese Schwierigkeiten zu überwinden, wenn man den Messbereich einschränkt oder die Oberflächen verändert. Selbstverständlich ist dies weder der beste noch der einfachste Weg zur Lösung dieser Probleme. Aufmerksam muß man auch sein damit die Probe beim Eintauchen nicht verändert wird.

Eine Alternative bietet die Flügeldrehkörper-Geometrie. Mit diesem System werden wenige Beschädigungen der Strukturen beim Tauchen des rotierenden Körpers auftreten. Die Probe wird homogen gehalten. In der vorliegenden Arbeit wird ein 4-armiger Flügeldrehkörper untersucht, welcher in einen Becher (cup) eingetaucht wird. Obwohl seine Form einfach ist, ist seine Anwendung bis jetzt auf die Bestimmung der Fließgrenze beschränkt.

Die Scherrate kann mittels numerischer Simulationen berechnet werden, welche der Validierung der experimentellen Daten und / oder der rheologischen Modelle dienen. Das so genannte Computational Fluid Dynamics (CFD) ist im Lauf der letzten zwanzig Jahre, mit zunehmender Tendenz zu der nicht-Newtonschen Flüssigkeiten, kontinuierlich weiterentwickelt worden. Heutzutage sind robuste numerische Verfahren und Hardware vorhanden, um relativ komplexe Strömungen zu untersuchen. Das ermöglicht, die experimentellen Grenzen zu überwinden, welchen man in der Rheologie begegnet und die von den Einschränkungen der Ausrüstungen oder den Messtechniken abhängig sind.

In der vorliegenden Arbeit sind experimentelle und numerische Untersuchungen für eine Flügeldrehkörperströmung durchgeführt worden. Die gesamte Arbeit ist strukturiert wie folgt.

Das 2. Kapitel gibt eine Übersicht der durchgeführten Arbeiten mit dem Flügeldrehkörper der letzten zwanzig Jahre. Eine Zusammenfassung der durchgeführten Untersuchungen zur Messung der Fließgrenze und der Versuche zur Ermittlung der Viskosität der Flüssigkeit wird vorgestellt.

Das 3. Kapitel widmet sich den numerischen Aspekten zur Durchführung der Sim-

ulationen für die Flügeldrehkörperströmung. Hier werden die Finite-Volumen-Methode (FVM) und das Verfahren für die Diskretisierung der herrschenden Gleichungen präsentiert. Es wird auch die dimensionlose Skalierung der allgemeinen Transportgleichung abgeleitet, welche das Fundament unserer Simulationen ist. Am Ende dieses Kapitels werden die für die Simulation angewendete Software und ihre Pre- und Postprocessing kurz beschrieben.

Das 4. Kapitel beschreibt den Flügeldrehkörper. Hier werden die Randbedingungen des Problems, das Gitter der Geometrie und einige theoretische Aspekte für seine allgemeine Anwendung zur rheologischen Charakterisierung des Materials festgelegt.

In dem 5. Kapitel wird die Methode der optischen Messtechnik PIV präsentiert, die für die Visualisierung der Strömung angewendet wird. Diese Technik ist umfangreich. Hier werden die Verfahren zur Bildaufnahme, statistische Bewertung und Datenanalysen vorgestellt, die der Schätzung der Verschiebung für die in der Flüssigkeit vorhandenen Tracer-Partikeln dienen.

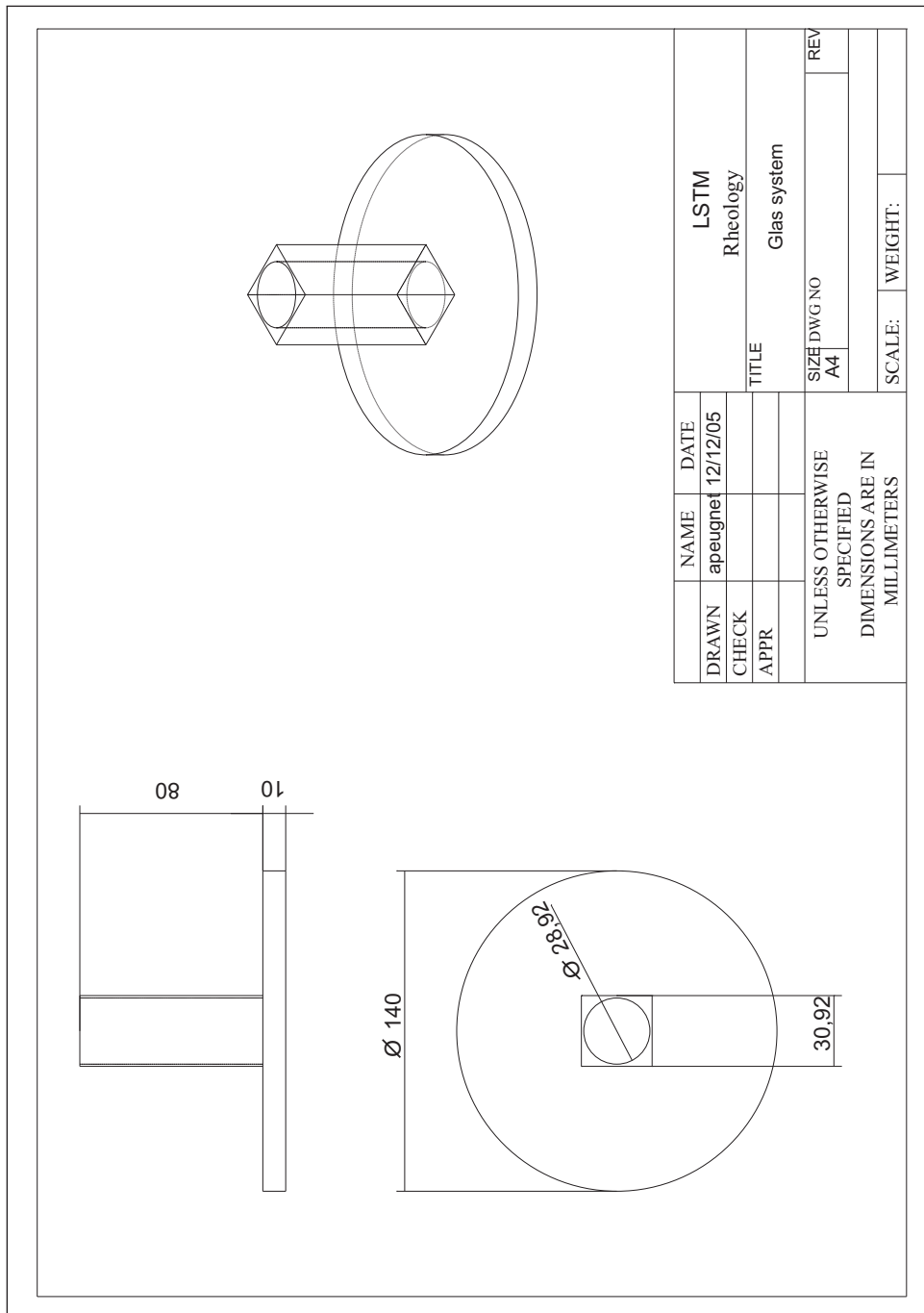
Das 6. Kapitel beschäftigt sich mit Newtonschen und nicht-Newtonschen Flüssigkeiten, nebst ihrer chemischen und physikalischen Eigenschaften. Das Bezugsviskosimeter, ein konzentrisches Zylinderviskosimeter, das zur Charakterisierung der verschiedenen Flüssigkeiten angewendet wird, wird unter idealen Annahmen vorgestellt, um die Schubspannung und die Viskosität einer Flüssigkeit zu bestimmen. Außerdem wird es mit der Geometrie des Flügeldrehkörpers verglichen.

Im 7. Kapitel wird eine rheologische Charakterisierung durchgeführt, wobei sowohl die Newtonschen und nicht-Newtonschen Fließkurven vorgestellt werden.

Im 8. Kapitel wird eine Methode beschrieben, die es erlaubt, den Flügeldrehkörper als Viskometer einzusetzen. Die im 7. Kapitel bestimmten Fließkurven der nicht-Newtonschen Flüssigkeiten werden mit den durch unsere Methode berechneten Kurven verglichen.

Zum Abschluss werden in den 9. und 10. Kapiteln Ergebnisse der experimentellen Visualisierung und der numerischen Simulationen für die Flügeldrehkörperströmung vorgestellt. Die Zusammenfassung gibt einen Überblick über die erhaltenen Ergebnisse.

A Cup of glass used for the PIV measurements (sketch)



A.1 Bob and vane geometries used for the experiments



Figure A.1: Bob and vane geometries (vane painted to black for the PIV-measurements).

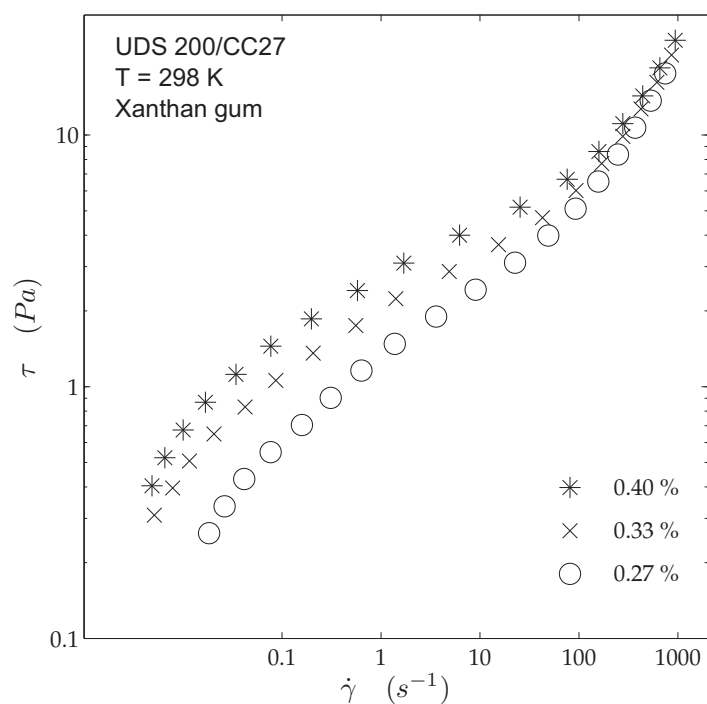
B Flow curves

Fluid	[c] (w/w) %	η_0 (Pa s)	η_∞ (Pa s)	α (-)	λ (s)
Hydroxypropyl guar	0.40	0.15	0.01	0.574	0.029
	0.50	0.33	0.01	0.624	0.059
	0.60	0.69	0.01	0.663	0.111
Xanthan gum	0.27	27.254	0.016	0.777	47.2825
	0.33	102.38	0.016	0.810	129.6086
	0.40	136.94	0.016	0.832	111.2683

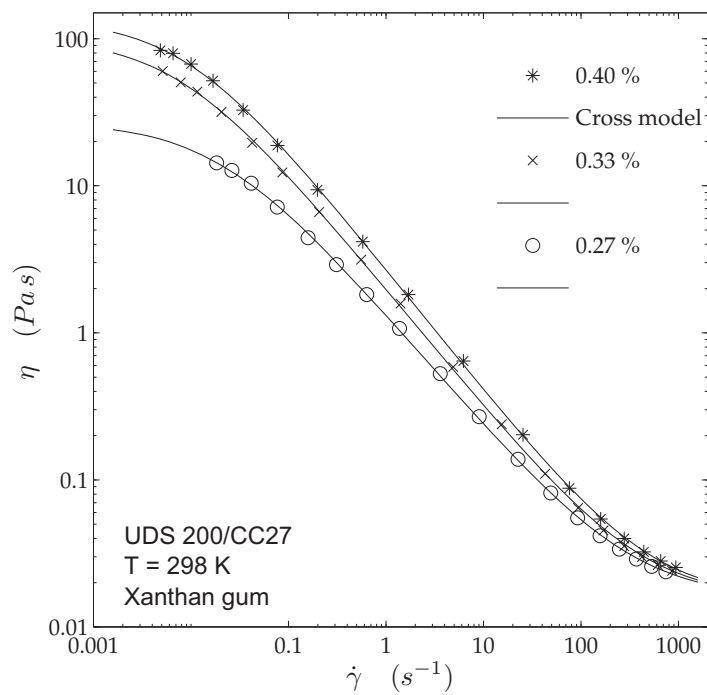
Table B.1: Parameters for the Cross model.

Fluid	[c] (w/w) %	η_0 (Pa s)	η_∞ (Pa s)	λ (s)	β (-)	n (-)
Polyacrylamide	0.05	4.7122	0.0180	31.32	1.5	0.28
	0.10	8.7438	0.0180	31.23	1.5	0.28
	0.20	27.63	0.0180	48.64	1.5	0.28

Table B.2: Parameters for the Carreau–Yasuda model.

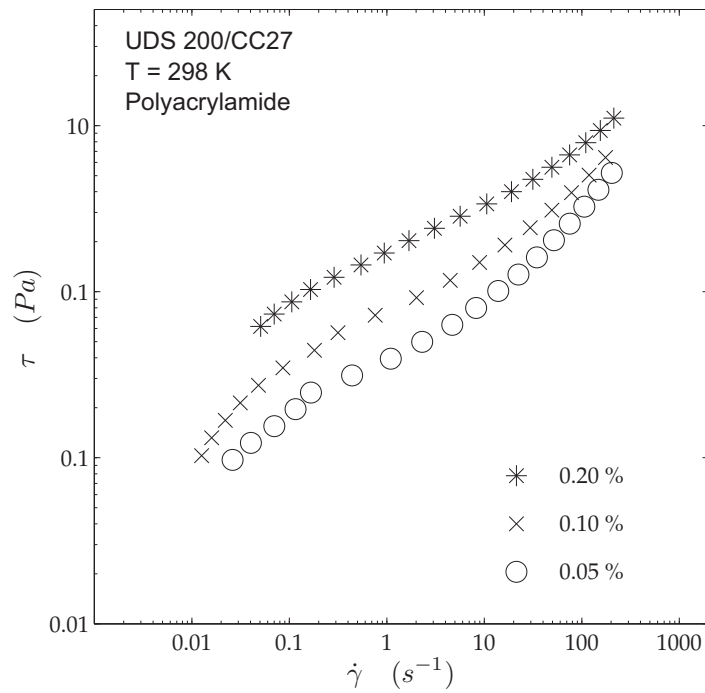


(a) Shear stress versus shear rate.

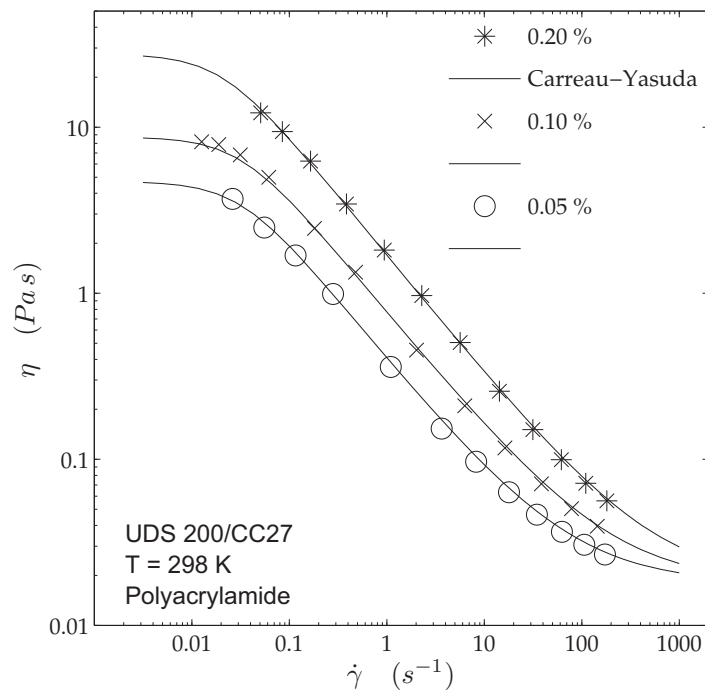


(b) Viscosity versus shear rate.

Figure B.1: Flow curves for the xanthan gum solutions. Points correspond to experimental data, solid lines to Cross model.



(a) Shear stress versus shear rate.



(b) Viscosity versus shear rate.

Figure B.2: Flow curves for the polyacrylamide solutions. Points correspond to experimental data, solid lines to Carreau-Yasuda model.

C Measurement of the yield stress

The existence of a yield point might be an arguable topic in rheology. In practice it is often accepted that the yield point is the limiting force, when a stress is applied to the sample, necessary to produce a *liquid-like* behavior, that is, a continuous deformation¹.

Regardless of the existence of this yielding point the use of this definition has been useful in engineering and the vane-in-cup system has been used to measure this particular material characteristic. In the following paragraphs the measurement of the yield stress with the vane geometry will be addressed.

The most simple relationship employed to estimate the yield stress comes from the assumption that the yield stress is distributed uniformly along the side and ends of an equivalent cylinder formed when the vane is rotated.

It can be written that

$$M_1 = M_S = \underbrace{2\pi r_v l_v \tau_w r_v}_{\text{Torque of a straight cylinder}} \quad (\text{C.1})$$

and

$$M_2 = M_E = 2 \left[2\pi \int_0^{r_v} \tau_e(r) r \, dr \right]. \quad (\text{C.2})$$

Here M_S and M_E stand for the torque at the side and at the end of the (imaginary) cylinder, respectively. r_v is the radius of the vane, τ_e and τ_w is the shear stress at the end and at the wall, respectively and l_v is the length of the rotating body.

Eq. C.2 is integrated assuming viscometric flow conditions. This is done in an interval for a small radius r and τ_e being equal distributed at both ends. A further assumption is that $\tau_e = \tau_w = \tau_y$. Then at the maximum shear stress τ_{\max} (corresponding to the maximum torque M_{\max}) it is assumed that the material yields instantaneously.

Thus,

¹Similarly one talks of a yield point when the applied stress is reduced to a certain limiting force where the sample shows a *solid-like behavior*. These definitions of course do not provide a satisfactory explanation of the yield stress. For further reading see [12].

$$M_{\max} = M_S + M_E, \quad (\text{C.3})$$

and consequently the sought yield stress is:

$$\tau_y = \frac{M_{\max}}{K}, \quad (\text{C.4})$$

with the constant K given by:

$$K = 2\pi r_v^3 \left(\frac{l_v}{r_v} + \frac{2}{3} \right). \quad (\text{C.5})$$

Notice that for $l_v/r_v \gg 2/3$ the constant K becomes the volume of a cylinder. The assumption that the shear stress is uniformly distributed everywhere on the imaginary cylindrical surface leads to some error ([58]). This error can be estimated experimentally if one measures with different radii r_v of the vane (height of the vane should of course kept constant). Experimental works from Nguyen et al. ([58]) suggest that for $l_v/r_v > 2$ the error associated with previous equations is reduced. Sherwood et al. ([72]) affirms that this value should be greater than 3 (despite this aspect ratio, numerical simulations show that the stress takes higher values near the edge of the vane [48], [63]).

D Velocity profiles for the NF and GNF

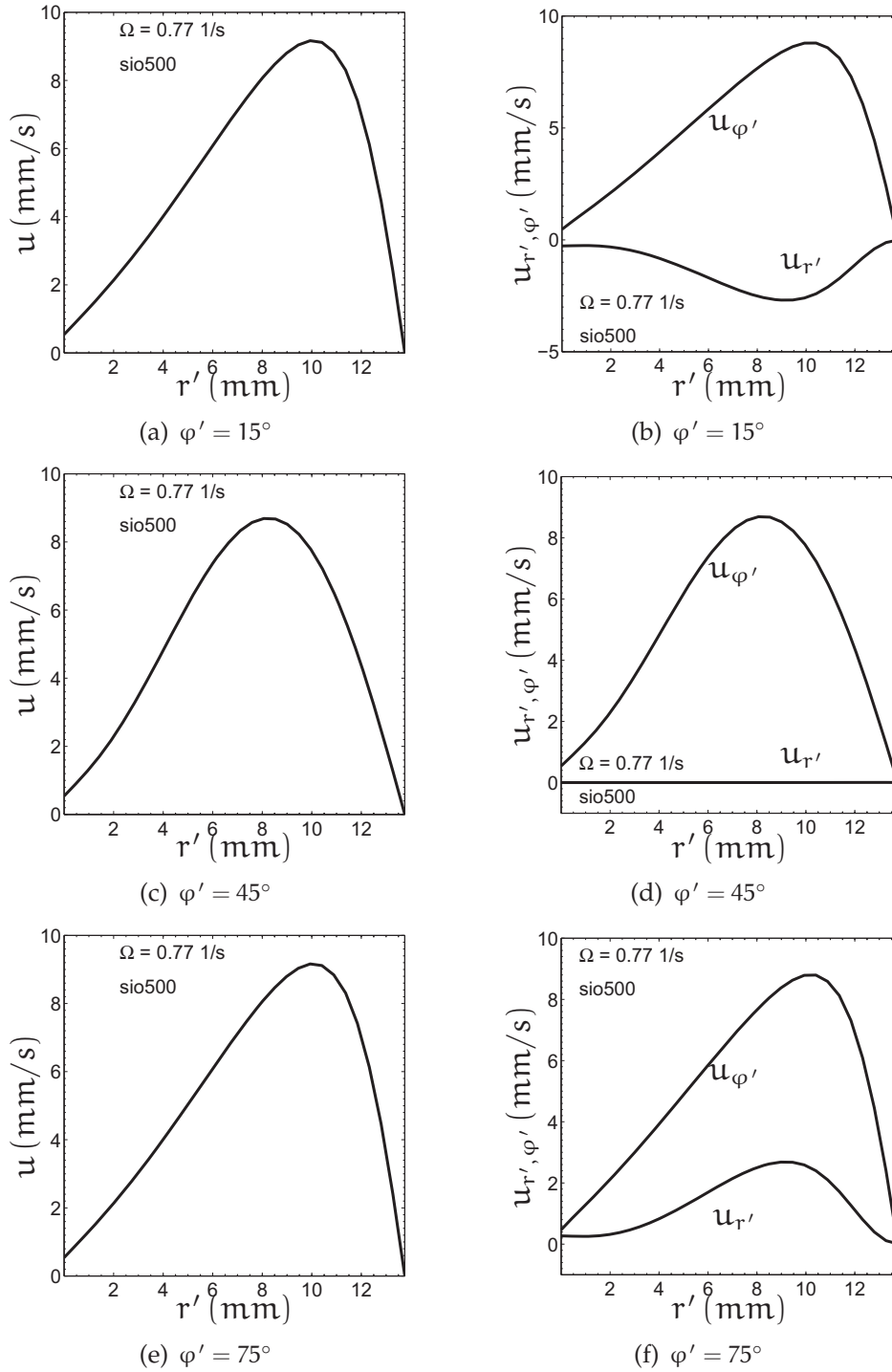


Figure D.1: Profiles of the total velocity at different angles and radial locations for the NF. Angular velocity $\Omega = 0.77 \text{ s}^{-1}$, \odot .

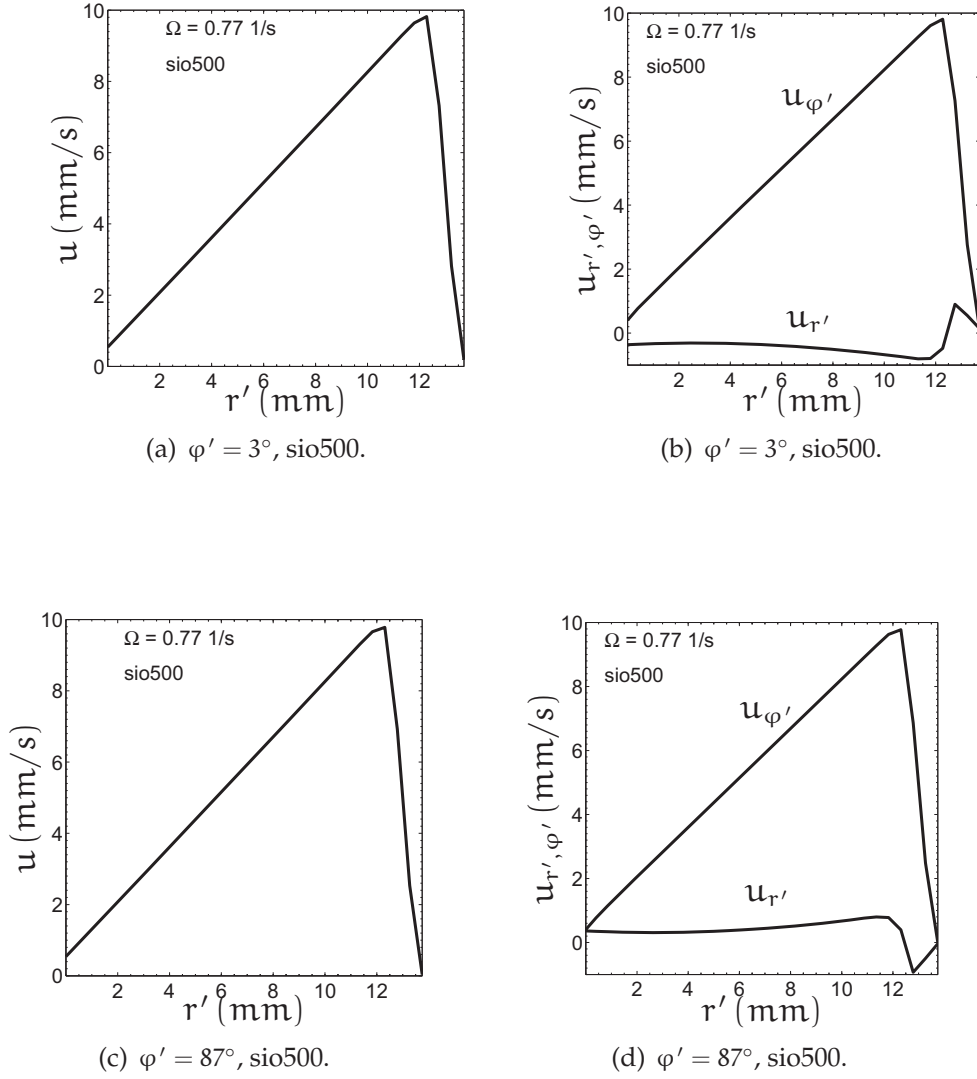


Figure D.2: Profiles of the total velocity at different angles and radial locations for the NF. Angular velocity $\Omega = 0.77\text{s}^{-1}$, \odot .

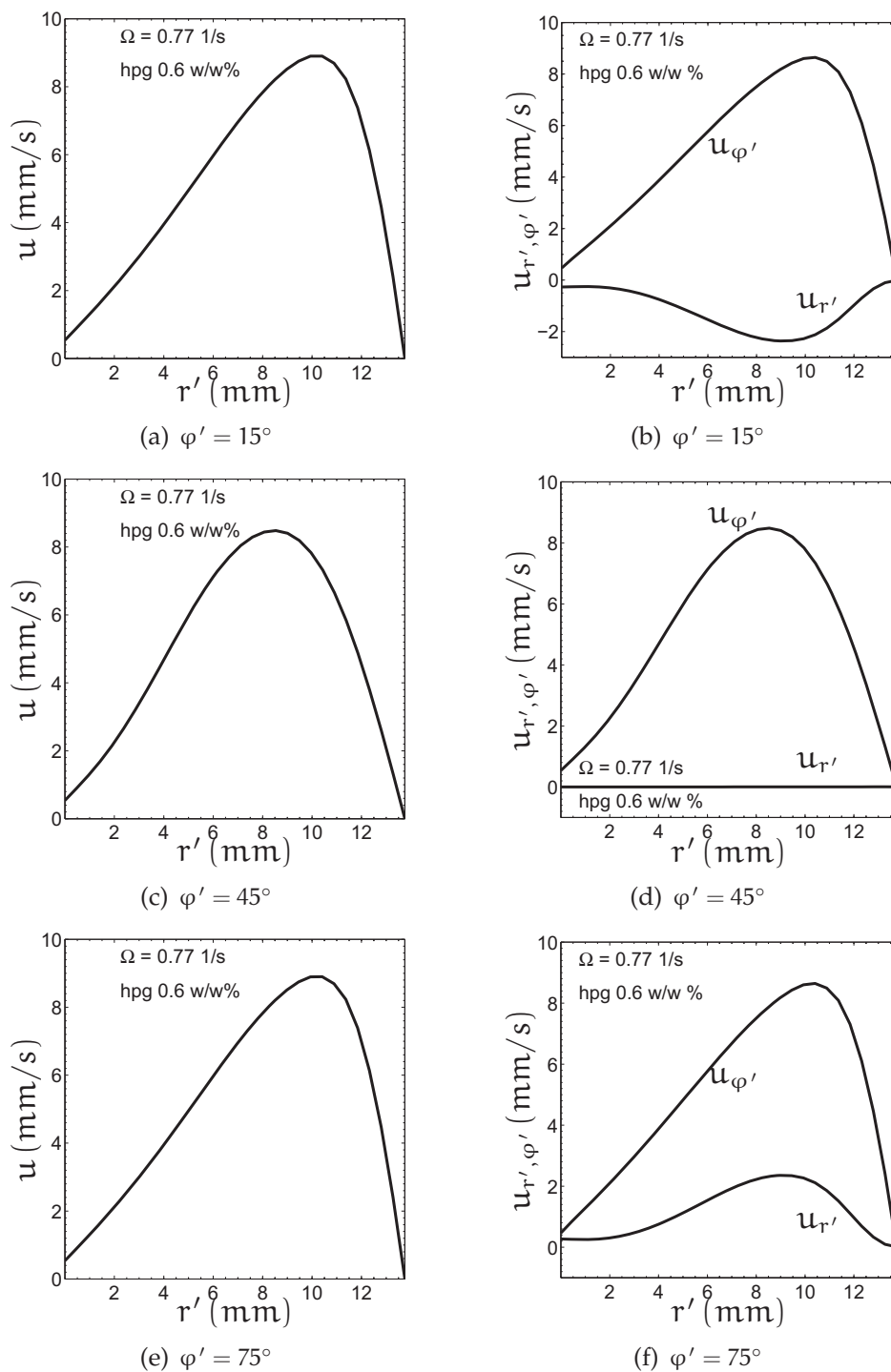


Figure D.3: Profiles of the total velocity at different angles and radial locations for the GNF. Angular velocity $\Omega = 0.77\text{s}^{-1}$, \odot .

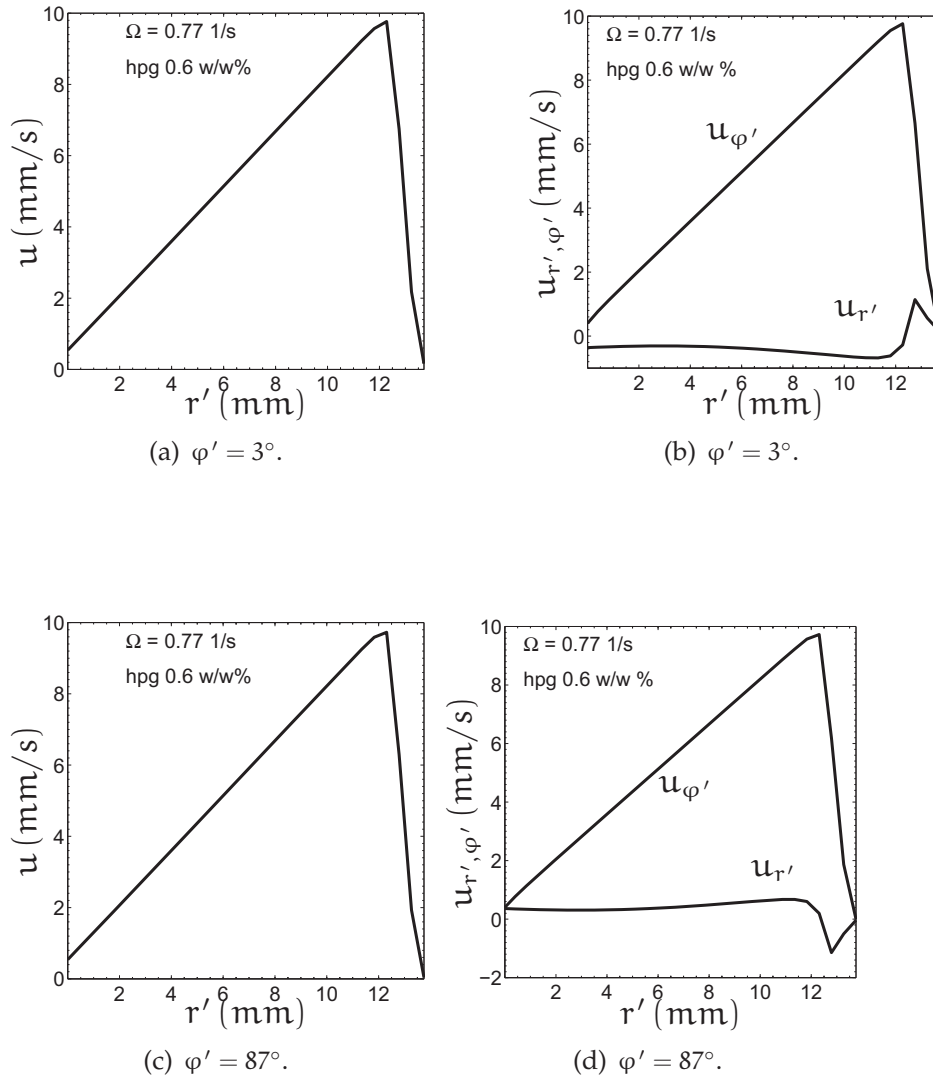


Figure D.4: Profiles of the total velocity at different angles and radial locations for the GNF. Angular velocity $\Omega = 0.77\text{s}^{-1}$, \odot .

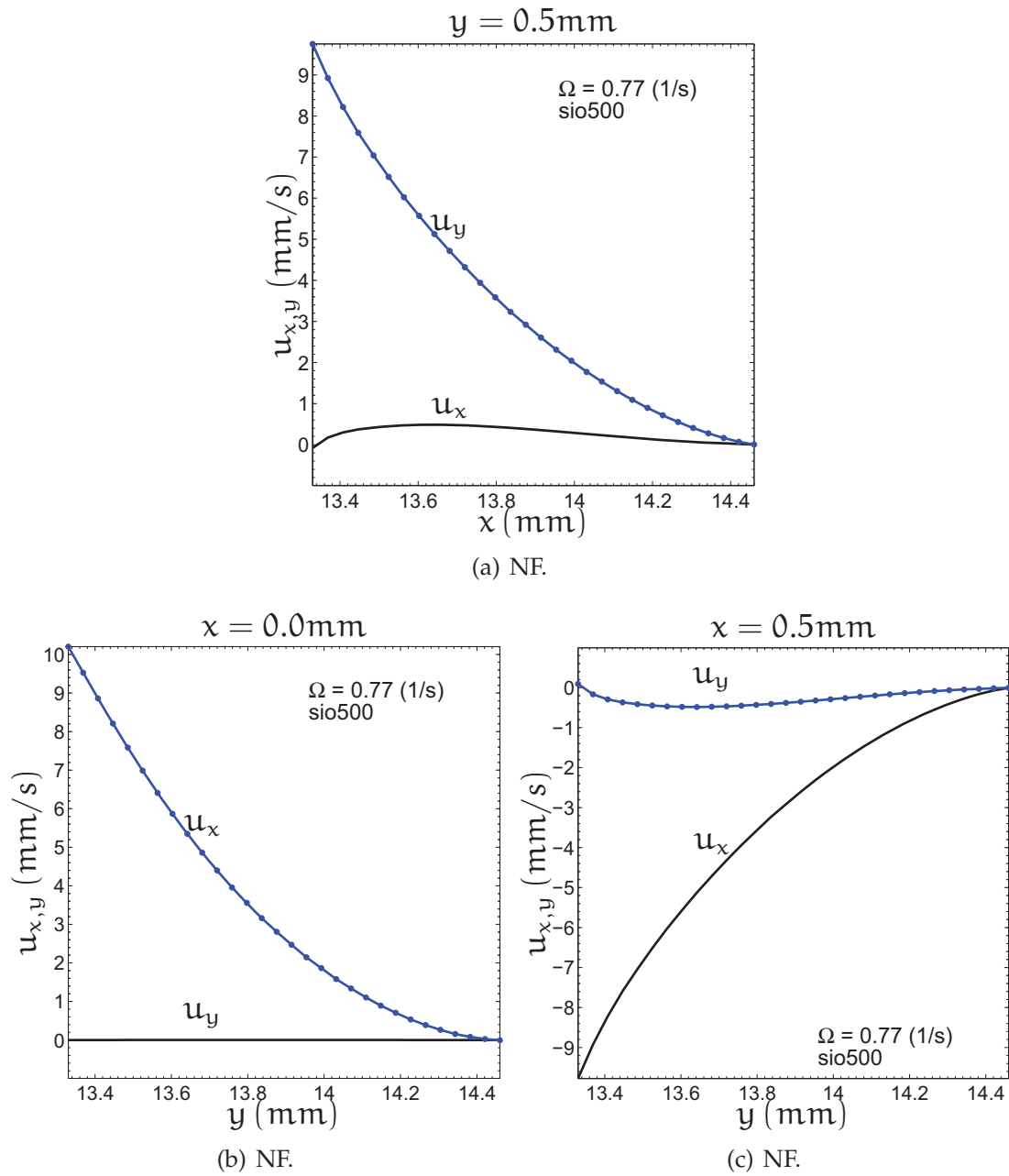


Figure D.5: Components of the velocity along the gap for the NF. Angular velocity $\Omega = 0.77\text{s}^{-1}$, \odot .

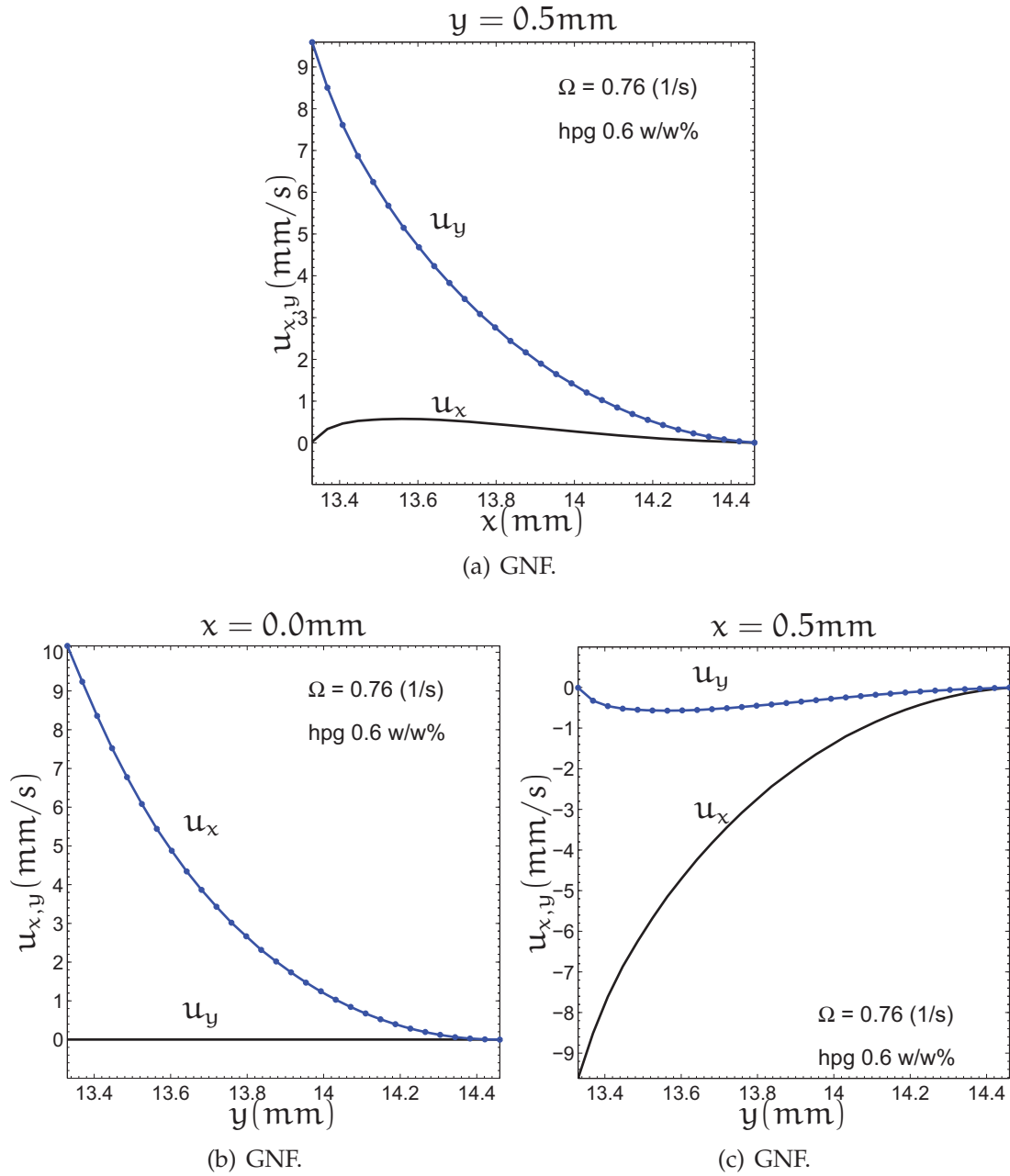
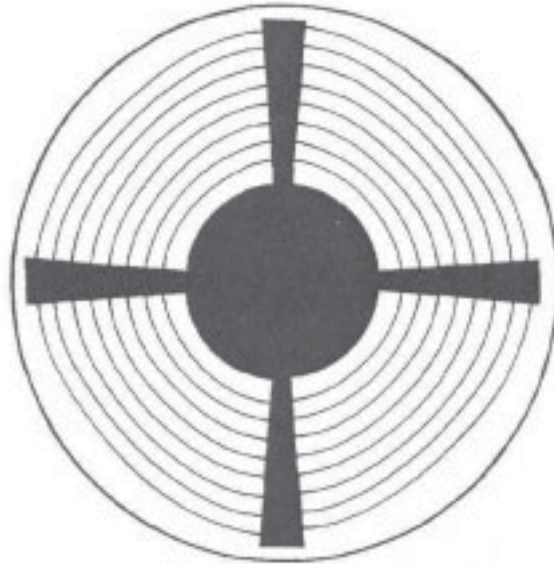
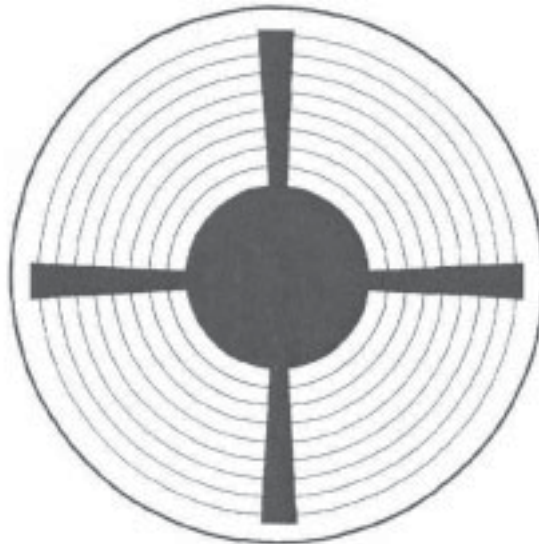


Figure D.6: Components of the velocity along the gap for the GNF. Angular velocity $\Omega = 0.76\text{s}^{-1}$, \odot .

E Streamlines for a NF and a power-law fluid (Ostwald de Waele)



(a) Newtonian fluid: $m = 1 \text{ Pa s}$, $n = 1$.



(b) Power-law fluid: $m = 1 \text{ Pa s}^{0.2}$, $n = 0.2$.

Figure E.1: Streamlines for a Newtonian and a power-law fluid (after Barnes et al. [11]). Angular velocity $\Omega = 0.5 \text{ s}^{-1}$ and viscosity η of the fluid $\eta = m \dot{\gamma}^{n-1}$.

List of Figures

2.1	Bob-in-cup geometry.	15
3.1	Two-dimensional orthogonal control volume and notation used.	21
3.2	Two-dimensional non-orthogonal control volume and notation used.	21
3.3	Stencil used for the linear interpolation.	26
3.4	Flow chart of the numerical procedure.	30
4.1	Four-bladed vane used in the present work.	32
4.2	Schematic representation of a four-bladed vane-in-cup geometry.	33
4.3	N-bladed vane geometry.	33
4.4	Cylindrical coordinate system.	36
4.5	Coordinate system and location of boundary conditions.	39
5.1	Schematic representation of a PIV set-up.	43
5.2	Flow chart for the particle image velocimetry procedure.	47
6.1	Molecule of silicon-oil.	49
6.2	General molecule of the Galactomannans.	50
6.3	Representation of the reaction to obtain hydroxypropyl guar.	51
6.4	Molecule of xanthan gum.	51
6.5	Molecule of polyacrylamide.	52
6.6	UDS 200	53
6.7	Schematic representation of the bob-in-cup geometry (CC 27).	54
6.8	Set-up used for the PIV measurements.	56
6.9	Location of the plane for the PIV-measurements.	57
7.1	Flow curves for the hydroxypropyl guar solutions	63
7.2	Flow curve for the hydroxypropyl guar	65
8.1	Characteristic curve for the vane flow (Ne vs Re).	68
8.2	Data of fig. 8.1 plotted as NeRe vs Re.	69
8.3	NeRe vs Re and NeRe _{ref} vs Re _{ref}	72
8.4	Viscosity curves NNF	74
8.5	Viscosity curves NNF	75
8.6	Shear rate vs angular velocity (bob and vane geometries).	76
8.7	Viscosity curves (using c_γ)	78
8.8	Viscosity curves (using c_γ)	79
8.9	Viscosity curves (averaged C_γ)	81
8.10	Viscosity curves (averaged C_γ)	82
9.1	Cup of glass used for the PIV measurements.	86
9.2	PIV measurement at $\Omega = 0.064 \text{ s}^{-1}$, Newtonian fluid sio80.	87
9.3	Sketch of the global and the local coordinate-systems.	88
9.4	Total-velocity profiles (PIV)	91
9.5	Components of the velocity (PIV)	92
9.6	Components of the velocity (PIV)	93

LIST OF FIGURES

10.1	Stream and contour lines for the NF sio500	98
10.2	Stream and contour lines for the GNF	99
10.3	Profiles of the total velocity and its components for the NF.	102
10.4	Profiles of the total velocity and its components for the GNF.	103
10.5	Profiles of the total velocity and its components for the NF.	105
10.6	Profiles of the total velocity and its components for the GNF.	106
10.7	Profiles of the total velocity and its components for the NF.	108
10.8	Profiles of the total velocity for the GNF.	109
10.9	Ideal velocity profile	110
10.10	Shear rate along the edge of the vane for the NF.	112
10.11	Shear rate along the edge of the vane for the GNF.	112
10.12	Shear rate along the gap for the NF.	113
10.13	Shear rate along the gap for the GNF.	114
10.14	Torque vs angular velocity for GNFs.	116
A.1	Bob and vane geometries.	138
B.1	Flow curves for the xanthan gum solutions	140
B.2	Flow curves for the polyacrylamide solutions	141
D.1	Profiles of the total velocity for the NF.	144
D.2	Profiles of the total velocity for the NF.	145
D.3	Profiles of the total velocity for the GNF.	146
D.4	Profiles of the total velocity for the GNF.	147
D.5	Components of the velocity along the gap for the NF.	148
D.6	Components of the velocity along the gap for the GNF.	149
E.1	Streamlines for a NF and NNF after Barnes et al.	150

List of Tables

2.1	Overview of the research–work carried out with the vane geometry. . .	5
3.1	Values of the transported variables.	22
4.1	Non–slip boundary conditions	37
6.1	Viscosities of Newtonian silicon oils	49
6.2	Dimensions of the vane geometry	55
7.1	Concentrations of polymer solutions	61
7.2	Parameters for the Cross model.	62
7.3	Parameters for the Carreau–Yasuda model.	64
7.4	Parameters for the Cross model when the solvent viscosity is used. . .	65
8.1	Device constants for the vane geometry.	77
10.1	Radial locations for the occurrence of the maximum velocity.	100
10.2	Locations for the velocity profiles along the gap.	107
B.1	Parameters for the Cross model.	139
B.2	Parameters for the Carreau–Yasuda model.	139

Index

- Assumptions
 - idealized, 31
- Boundary conditions, 35
 - periodicity conditions, 36
 - wall conditions, 35
- Carreau–Yasuda
 - model, 60
 - parameters, 64, 139
- CFX solver, 27
- Couette approximations, 13
- Cross
 - model, 60
 - model parameters, 62
 - model parameters (when the solvent viscosity is used), 65
- Flow curves, 59
 - hydroxypropyl guar, 62
 - polyacrylamide, 62
 - xanthan gum, 62
- Finite volume method
 - FVM, 19
- Governing equations, 34
- Newtonian fluids, 49
 - silicon oil, 49
- Non–Newtonian fluids, 50
 - hydroxypropyl guar, 50
 - polyacrylamide, 51
 - xanthan gum, 50
- Numerical simulations, 95
 - flow field, 96
 - torque, 115
- Particle image technique
 - measurements, 85
- PIV, 41
- Rheology, 1
- Rheometer
 - UDS 200, 52
- Torque on a rotating vane, 32
- Vane, 5, 8–14, 16, 17
 - effect of dimensions, 14
 - end effects, 15
 - fracture zone (surface of shearing), 8
 - geometry, 5, 31
 - material characterization, 5
 - measurement of the yield stress, 7
 - mesh for the vane geometry, 38
 - vane–in–cup, 5
- Viscometer
 - bob–in cup geometry, 53
 - vane–in–cup geometry, 54
- Yield stress
 - stress distribution, 8, 10
- yield stress, 2
- Yield stress
 - measuring of the, 142

Curriculum vitae



Name		Alejandro Peugnet
Date of birth		23.07.1974
Nationality		Nicaraguan
School	1982–1991	Colegio madre del divino pastor Carazo, Nicaragua
University	1992–1997	Chemical engineering National university of engineering Managua, Nicaragua (Ing)
	1998–2001	Master studies in process engineering Friedrich–Alexander University Erlangen, Germany (MSc)
	2002–2005	PhD studies in experimental and numerical rheology at the institute of fluid mechanics, Friedrich–Alexander University Erlangen, Germany
Professional experience	2002–2005	Scientific researcher at the institute of fluid mechanics (rheology group) at the Friedrich–Alexander University Erlangen, Germany
	Since 2006	System & process engineering Thermohydraulics, R & D. AREVA NP GmbH Erlangen, Germany
